

Design, Synthesis and Microstructural Characterization of Ni(Zn)-
Alumina composite particles for Cold Spray Additive
Manufacturing

by

Vineeth Menon

B.Tech, Metallurgical Engineering, N.I.T. Raipur, 2015

M.Tech, Metallurgical & Materials Engineering, I.I.T. Kharagpur, 2018

A Thesis Submitted in Partial Fulfillment
of the Requirements for the Degree of

Master of Science in Engineering

in the Graduate Academic Unit of Mechanical Engineering

Supervisor: Gobinda C. Saha, PhD, Mechanical Engineering

Examining Board: Rickey Dubay, PhD, Mechanical Engineering, Chair

Clodualdo Aranas, PhD, Mechanical Engineering

Zhibin (Ben) He, Ph.D., Chemical Engineering

This thesis is accepted by the

Dean of Graduate Studies

THE UNIVERSITY OF NEW BRUNSWICK

June, 2024

©Vineeth Menon, 2024

Abstract

In this work, the high-energy mechanical alloying (HE-MA) method was used to manufacture nanostructured Ni(Zn)–Al₂O₃ composite particles, to be utilized as particle feedstock in cold spray additive manufacturing process. Pre-milled Ni(Zn) alloy precursors were milled in SPEXTM 8000 M high energy ball mill. Microstructural characterization with Electron backscatter diffraction (EBSD) studies and particle size distribution of Ni(Zn) alloy particles showed that, in comparison to Ni(10wt.%Zn) alloy particles, Ni(5wt.%Zn) experienced higher plastic deformation, work hardening, and fracture. Two design compositions (30-wt.% and 50-wt% α -alumina) were paired with two substitutional alloy compositions, Ni(5wt.%Zn) and Ni(10wt.%Zn), for the material design-of-experiment (DoE). The embedment of nanometer-sized α -alumina grains in micron-sized Ni(Zn) alloy matrix was confirmed via microstructural analysis. The composite particles that were milled for four hours had the desired particle size distribution to serve the purpose for cold spraying, according to the particle size measurement obtained via laser diffraction spectroscopy (LDS).

Acknowledgement

This research has been made possible by the incredible help and guidance from the project supervisor Dr. Gobinda Saha and all my colleagues from the Nanocomposites and Mechanics Laboratory (NCM Lab), Department of Mechanical Engineering, University of New Brunswick, Fredericton. I am also courteous to Dr. Clodualdo Aranas for the help he has provided so far during the execution of this research work. Advice and assistance while performing the experimental works related to Scanning electron microscopy, X ray diffraction and Particle size distribution from Mr. Steven Cogswell, Dr. Venkatarami Reddy, Dr. Dennis Connor is deeply appreciated and thanked. I am also grateful to the support provided by New Brunswick Innovation Foundation (NBIF STEM & Social Innovation Award) and Natural Sciences and Engineering Research Council Canada (NSERC) for conducting this research and making it possible.

Table of Contents

Abstract	ii
Acknowledgement.....	iii
Table of Contents	iv
List of Tables	vii
List of Figures	viii
Chapter 1 Introduction	1
1.1 Motivation.....	2
1.2 Scope of the research	3
1.3 Research Questions and Hypothesis	4
1.4 Goal of Research and Objectives.....	6
Chapter 2 Literature Review	7
2.1 Metal Matrix Composites (MMCs).....	7
2.2 Powder production techniques	8
2.3 Powder Modification Techniques.....	9
2.4 High-Energy Mechanical Alloying (HE-MA)	10
2.5 Process Variables in Mechanical Alloying (MA).....	15
2.5.1 Type of mill.....	16
2.5.2 Milling receptacles	16
2.5.3 Milling speed	16
2.5.4 Milling duration	17
2.5.5 Grinding media	18
2.5.6 Weight of balls to powder ratio.....	19
2.5.7 Filling level of the vial	19
2.5.8 Milling environment	20
2.5.9 Role of surfactants in mechanical milling/ alloying.....	21
2.5.10 Milling temperature	23
2.6 Types of mills	25

2.6.1 SPEX [®] shaker mill	25
2.6.2 Planetary ball mill	26
2.6.3 Attritor mill	28
2.6.4 Commercial mills	29
2.7 Material selection for current research	29
2.8 Applications	31
2.8.1 Nickel based alloys	31
2.8.2 Copper based alloys	32
2.8.3 Cobalt based alloys	33
2.8.4 Aluminum based alloys	33
2.9 Cold gas dynamic spray (CGDS) technology	34
2.10 Summary	37
Chapter 3 Research Methodology	39
3.1 Milling methodology for Ni(Zn)- α -alumina particle synthesis	39
3.2 Specimen characterization	41
3.3 Instrument details	41
3.3.1 SPEX [®] 8000M mixer/mill	41
3.3.2 Malvern particle analyzer	42
3.3.3 Scanning electron microscopy (with EDS and EBSD)	43
3.3.4 X-ray diffraction	47
3.4 Summary.....	48
Chapter 4 Results and discussions.....	49
4.1 Microstructural characterization of as-received and pre-milled Ni(Zn) alloy precursors.....	49
4.2 EBSD characterization of Ni(Zn) alloy particles.....	54
4.3 Particle size distribution analysis	61
4.4 Microstructural characterization of Ni(Zn)-alumina composite particles.....	66
4.5 X-ray diffraction analysis	75
4.6 Summary.....	84
Chapter 5 Conclusion and Future Recommendations	85
Bibliography	88

Appendix A: Material data sheets 107
Curriculum Vitae

List of Tables

Table 3.1: The identification of the powder particle specimens and their milling settings	40
Table 4.1: The associated mean and median values as well as a PSD analysis for specimens (S1-S12) [103].....	63
Table 4.2: List of elements shown in the EDS analysis of S3 specimen [103].	74
Table 4.3: Crystallite size was determined for (a) matrix and (b) ceramic reinforcement using the W-H method [103].....	77
Table 4.4: Calculation of (a) lattice parameter; and (b) c/a ratio of various compositions [103].	80

List of Figures

Figure 2.1: Aluminum metal matrix composite utilized in the making of (a) piston, (b) cylinder barrel-equipped engine, (c) piston linking rod, (d) Braking mechanism [33]	8
Figure 2.2: SEM image demonstrating the incorporation of the hard Si particles into the softer Ge matrix during a 12-hour mechanical alloying process of the Si-Ge powder mixture [45,47]	12
Figure 2.3: TEM image of a mechanically milled α 2-titanium aluminide matrix with the dispersion of Er_2O_3 in it [45,48]	13
Figure 2.4: SEM image illustrating the complex lamellar structure produced by milling a ductile- ductile component system (Ag-Cu) [45]	15
Figure 2.5: An illustration of the functioning of surfactant in the mechanical alloying/milling process [62]	22
Figure 2.6: SPEX [®] 8000 mixer/mill [50]	26
Figure 2.7: (a) A P-5 four station ball milling machine Fritsch Pulverisette; and (b) diagram showing motion of the balls move within the ball mill. [50]	27
Figure 2.8: An illustration of a vertical attritor including a rotating impeller [45]	28
Figure 2.9: An image showing the cold spray process [91]	35
Figure 2.10: Typical particle diameter range for several materials in CGDS research studies [92].....	36
Figure 3.1: Malvern mastersizer MAZ2000S consisting of (1) Optical unit, (2) Sample dispersion accessory, and (3) computer system [97]	43
Figure 3.2: A D8 X-ray diffractometer [102]	48

Figure 4.1: Scanning electron micrographs of alloy compositions (a) Ni (5wt.% Zn), (b) Ni (10wt.% Zn) along with (c) α -Al ₂ O ₃ particles [103]	52
Figure 4.2: Particle morphology microstructure of both the (a) Ni(5wt.% Zn) and (b) Ni(10wt.% Zn) pre-milled for 2 hours.	53
Figure 4.3: Scanning electron micrograph of Ni(5wt.%Zn) particles pre-milled for 2 hours [103].....	53
Figure 4.4: IPF maps for as-received alloy precursors (a) Ni(5wt% Zn), (b) Ni(10wt.% Zn) and pre-milled (c) Ni(5wt.% Zn), and (d) Ni(10wt.% Zn) particles for 2 hours [103]	56
Figure 4.5: Grain size distribution for as-received alloy precursors (a) Ni(5wt.% Zn), (b) Ni(10 wt.% Zn) and pre-milled (c) Ni(5wt.% Zn), and (d) Ni(10 wt.% Zn) particles for 2 hours [103].....	58
Figure 4.6: EBSD band contrast image for as-received alloy precursors (a) Ni(5wt.% Zn), (b) Ni(10wt.%Zn) and pre-milled (c) Ni(5wt.% Zn), and (d) Ni(10wt.% Zn) particles for 2 hours [103].....	61
Figure 4.7: PSD in relation to cumulative volume fraction for (a) Ni(5wt.%Zn) and Ni(10wt.% Zn) alloy particles pre-milled for 2 hours, (b) as received α -Al ₂ O ₃ particles [103].....	62
Figure 4.8: Illustration the transformation of PSD in the milled specimens (S1-S12) [103]	65
Figure 4.9: SEM images of post-milled samples following a 4-hour milling period. Batches #1, #2, #3, and #4 are represented by Figures 4.9(a)- 4.9(d), respectively [103]	69
Figure 4.10: HE-MA mechanisms of Ni particles incorporating alumina reinforcements: (a) particle flattening, (b) alumina embedment, and (c) alumina agglomeration [114]...	70
Figure 4.11: Characteristics seen in the SEM image include: a) embedding in S3, b) matrix fusion in S6 (with an insert depicting the enlarged view of fusion), and c) particle size assessment in S3 [103]	72

Figure 4.12: Specifications of the S3 composite specimen: (a) SE microstructure; (b) elemental distribution maps, arranged as follows: (i) mounting carbon, (ii) oxygen, (iii) aluminum; (iv) nickel, (v) zinc, (vi) iron; (vii) chromium, and (viii) phase-map [103].... 74

Figure 4.13: XRD pattern for particle specimens S3, S6, S9, S12, S13, and S14 [103] 76

Figure 4.14: The graph depicts crystallite size of the following samples: (a) Ni(Zn) as-received particles and S13, and S14 specimens; (b) as-received alumina and alumina reinforcement in S3, S6, S9, and S12 specimens [103] 79

Figure 4.15: (a) lattice parameters of Ni(Zn) alloy particles specimens S13, S14 and the lattice parameters of Ni(Zn) alloy matrix in composite specimens S3, S6, S9, S12; and (b) c/a ratio of lattice parameters of as-received alumina as well as alumina reinforcement in composite specimens S3, S6, S9, S12 [103]..... 82

Chapter 1 Introduction

Many metallic components used in the power, automotive, aerospace, and materials industry sectors may benefit from coatings made of Nickel element as a principal component. Nickel has remarkable high-temperature properties, hardness, and strength. Ni-based metal matrix composites (MMCs) have been sprayed onto a variety of substrates by researchers using cold gas dynamic spray process (CGDS) [1], plasma spraying [2], High velocity oxy-fuel (HVOF) [3] etc. MMC belongs to the composite material family class with varying combinations of metal/alloy and ceramic constituents. The resulting material can deliver new material properties and physical characteristics when applied as feedstock in spray coating technologies. The challenge however is that the combinations are neither experimental validated, nor are they functionally innovative for shielding industrial components from high temperature wear and oxidation resistance. As far as engineering applications are concerned, there is industrial demand for innovative material design and their successful deposition on substrates so to enhance the service lives operational components.

One method to achieve this is to suppress wear and oxidation losses by applying coatings made of novel material compositions achieved through experimental design and synthesis of the MMC feedstock. This directly affects the plant's dependability and efficiency when it comes to operation in high temperature conditions. For instance, very thin coatings made of such MMC feedstock are well resistant to oxidation and wear that may safeguard the

turbine components at elevated temperatures [4]. From automotive to aircraft industrial uses, there is a growing recognition of the necessity for lightweight, high strength materials. The hardness and stiffness of a material required is high and mass required is low. This has several benefits, such as the ability to carry a larger shipment and/or increased fuel efficiency. Finding materials with the necessary mechanical strength that are also affordable and lightweight is a difficulty for many applications. Although there are a few materials that can fulfill these needs in their basic form, the creation of MMCs reinforced with ceramic particles have emerged as a new concept for the design of novel materials with distinctive characteristics like low weight and high strength [5].

The major factors influencing MMC performance are: (1) distributing reinforcement particles throughout the metal matrix sufficiently; (2) preserving the structural integrity throughout the synthesis of composite particle feedstock; and (3) creating an appropriate matrix-reinforcement particle interface [6-11]. Lowering the crystallite size of metal matrix to the nanoscale level can further increase an MMC's strength [12].

1.1 Motivation

Due to the ability to improve the coated substrate materials' resistance to high temperatures, high wear rates, coatings are incredibly helpful in protecting substrate materials during harsh working circumstances. These coatings may be useful in several industries like aerospace, automotive, shipbuilding, mining and marine [13-16]. Several researchers have been investigating the merit of Ni based coatings with different kinds of reinforcements

that could prove meritorious in providing protection to the metal components or structures in the industries making them resistant to deterioration and thereby contributing to the overall economic, social, and environmental benefits [17-26].

The MMC particle feedstock created by high-energy mechanical milling can be a solution to many problems faced by the coatings in terms of mechanical, tribological or corrosion properties. The microstructure of a MMC particle feedstock contains ceramic grains uniformly dispersed in the metal matrix, thereby enabling it to impart uniform properties when sprayed onto substrates. Ni based MMC particle feedstock synthesized in this research shall provide uniform mechanical and tribological properties to industrial standard substrates subjected to high temperature environments.

1.2 Scope of the research

The better strength merit of nickel(zinc) substitutional alloy over its parent element, nickel, has been suggested in the current research work. Zinc atoms contribute to the lattice strains in the FCC (face-centered cubic) crystal structure by taking up some of the nickel's lattice locations. In order to block dislocations and provide alloy strength, these lattice strains may be significant. To the best of author's knowledge, no study has been performed on the design, synthesis, and spraying of reinforced Ni(Zn)-Al₂O₃ particles, therefore composite CS coatings composed of nickel zinc substitutional alloy would be a novel composition to work with. The tribological characteristics of Ni(Zn) based MMC coatings should be better than those of nickel-based MMC coatings due to the anticipated increased hardness of

Ni(Zn) alloy-based composites. Furthermore, the Ni(5wt.%Zn) and Ni(10wt.%Zn) alloys utilized in this study have melting points that are both very close to 1,400° C, which makes them suitable for high temperature applications. This also enables the use of higher carrier gas temperatures during HPCS (high-pressure cold spray), which raises the deposition efficiency (DE) of Ni(Zn)-Al₂O₃ particles. Alumina is a low-cost, low-density ceramic material with good wear, corrosion, high temperature stability, and fracture toughness properties among the several reinforcements that are accessible [27].

1.3 Research Questions and Hypothesis

The research has therefore developed the following research questions with corresponding hypotheses to direct through the research methodology chosen, as inferred from the discussion above:

1. How does the composition of composite particles affect the way that ceramic grains are incorporated into the alloy matrix?

To ensure appropriate embedding of ceramic grains to obtain homogeneous composite particle composition, the alloy matrix should have an optimal amount of ceramic reinforcement to avoid excess agglomeration. Also, the size range of alloy particles should be at least a magnitude higher than the size range of ceramic grains.

2. How does the milling time of composite particles affect the way that ceramic grains are incorporated into the alloy matrix?

The longer milling period ought to improve the homogeneity of the ceramic grain embedment in the matrix of the substitutional alloy. In the initial stage of milling process, severe plastic deformation, particle flattening, and subsequent cold welding is prominent. The larger surface area of a flattened particle facilitates the embedment of ceramic grains into alloy matrix. Along with the progress in milling time, work hardening increases and fracture toughness decreases which eventually gives equiaxed composite particles.

3. What impact does a higher Zn content in Ni have on the characteristics of Ni(Zn)-alumina composite particles?

A higher Zn content in the Ni(Zn) substitutional alloy will result in higher hardness and the milled composite particles made of it is expected to have higher hardness and possibly higher mechanical strength and wear resistance properties when such particles are cold sprayed on to a metallic substrate.

4. What impact does HE-MA have on the grain size and particle size distribution (PSD) of the HE-MA composite particles?

When milling time increases, mechanical milling might lower PSD. Nevertheless, the amount of PCA supplied, the ductility of the powder particles, and the fracture of the particles during milling all affect how much the particle size decreases. The ductility and composition of the cermet powder particles determine the distribution of grain sizes inside. The grain size distribution should be finer the longer the milling period.

1.4 Goal of Research and Objectives

This research aims to develop Ni(Zn) alloy particles with α -alumina grains embedded in it to form Ni(Zn)-alumina composite HE-MA particles for their microstructural characterization and evaluation of their merit for eventual cold spray-ability on industry standard substrates. These Ni(Zn)-Al₂O₃ particles are intended to have homogenized embedment of ceramic grains throughout the metal matrix so that upon cold spraying the coatings made can have uniform mechanical properties. Also, the substitutional alloy Ni(Zn)-alumina coatings made out this feedstock is expected to have enhanced high temperature properties as compared to coatings made of discrete Ni-Zn-alumina based coatings. The outcome of this research is significant for industries that use metallic components subject to wear. This shall reduce the overall component and equipment maintenance costs.

The objectives for the research project are as follows:

- To synthesize and characterize a novel Ni(Zn) substitutional alloy-based Ni(Zn)- α -Al₂O₃ composite particle feedstock by HE-MA method.
- Designing experiments for composite particle feedstock synthesis with respect to varying compositions and milling time.
- Investigate the crystallite size, microstructural analysis, extent of plastic deformation in Ni(Zn)- α -Al₂O₃ composite alloy particles.

Chapter 2 Literature Review

2.1 Metal Matrix Composites (MMCs)

MMCs have advanced significantly in the last 50 years, particularly, many novel applications have been created for commercial and research objectives. Aerospace, thermal management, ground transportation, infrastructure, sports products, and industrial sectors are pertinent uses. Usually made of ceramic, reinforcement in MMCs takes the shape of whiskers, particles, continuous fibers, or short fibers [28-30]. Due to their inherent isotropic features and inexpensive cost, MMCs have garnered much attention. Carbides, nitrides, and oxides are examples of reinforcement materials. The selection of reinforcement particles for the metal matrix may depend on thermal stability, melting temperature, strength, particle morphology, cost, elastic modulus and compatibility with matrix material [31]. MMCs' properties can be adjusted to meet the needs of various industrial applications by selecting the right matrix, reinforcement, and processing route combinations. Many studies have yielded many fresh scientific information about the inherent and extrinsic impacts of ceramic reinforcement on MMCs' mechanical, thermomechanical, physicochemical, and tribological properties. For instance, the braking systems of vehicles and trains use aluminum matrix composites in the most significant way due to their massive size and great volume. Now, aluminum matrix composite brake discs are widely utilized in European railroads and in some passenger automobile models in the United States [32]. Figure 2.1 illustrates a few of the applications utilizing Al MMCs [33].



Figure 2.1: Aluminum metal matrix composite utilized in the making of (a) piston, (b) (b) cylinder barrel-equipped engine, (c) piston linking rod, (d) Braking mechanism [33].

2.2 Powder production techniques

Particulate matters (or powders) are the building blocks of modern-day additive manufacturing era. The size, shape, and composition of powder particles are influenced by the desired additive manufacturing technologies such as thermal or cold spray. In the manufacturing regime, molten metallic bulk is broken up into tiny droplets during the atomization process, which is followed by solidification [34-38]. Water atomization, gas atomization, and plasma atomization are the different atomization methods. In contrast to

the spherical particles obtained from inert gas atomization, water atomization yields irregular particles. Water atomization is not a good way to make powders for CS since the resulting powders have more contamination [34,38]. For CS application, near-spherical particles are produced via the plasma atomization method [34]. Both gas and plasma-atomized powders have lower levels of oxygen contamination. The production of fine or dendritic grains may result from the quick cooling of the fine molten droplets, which could also raise the dislocation density. Particle size, cooling rate, and processing variables all have a major impact on the microstructure.

Another method for making powders that works well with fragile particles is mechanical crushing. For usage in the thermal spray method, titanium derived from raw rutile - which is porous and spongy - is ground into a fine powder. Also, copper, having a dendritic structure is formed by the electrolysis process, which is a very commonly utilized element in thermal spraying [39].

2.3 Powder Modification Techniques

These methods are useful in achieving the powder properties needed for applications involving CS. Through a process called plasma spheroidization, spherical particles can be created from particles of any size or shape. Before quickly solidifying, the particles travel through a plasma jet melt and take on a spherical shape [34,41]. Ball milling is another widely used method. Particles are deformed, fractured, and rewelded during the ball milling process by the motion of hard milling balls. The resulting powders are shaped irregularly

[34,41]. Ball milling facilitates the homogeneous dispersion of second-phase particles inside the metal matrix, resulting in composite powders that are appropriate for use in cold spraying [42]. Also, powders with a nanograin structure are produced by cryogenic ball milling in a liquid nitrogen atmosphere [40,43,44].

2.4 High-Energy Mechanical Alloying (HE-MA)

A high-energy ball mill is used to repeatedly weld, fracture, and then reweld a combination of powdered particles. During the milling process, the powder particles become caught between the colliding balls and based on the mechanical properties of the powder components, experience deformation, fracture, or welding. Metal-matrix composites, intermetallic compounds, amorphous materials, and supersaturated solid solutions are among the materials and alloys that can be created with this procedure [45]. John S. Benjamin's research showed that in a nickel-base superalloy, age hardening and fine particle dispersion strengthening can be combined via mechanical alloying in the year 1970. Yttria proved to be an efficient dispersion strengthening agent in Nickel based superalloy. The dispersion strengthening along with precipitation hardening mechanism in the nickel-based superalloy complement one another for temperature up to 1500° F [46]. Mechanical alloying of metals has been primarily used in the development of oxide dispersion strengthened (ODS) commercial alloys based on copper, aluminum, and nickel. Elevated temperature strength is a characteristic of these materials that arises from multiple causes. The first characteristic of their structure is the uniform dispersion of very fine (between 5 and 50 nm) oxide particles of stable oxides, such as beryllia (BeO), lanthana (La₂O₃), yttria (Y₂O₃), thoria (ThO₂), titania (TiO₂), and alumina (Al₂O₃). These particles have an

approximate spacing of 100 nm throughout their structure. This dispersion reduces the deformation in alloy due to creep by preventing the motion of dislocations in the metal matrix. The dispersoid particles also prevent the processes of recovery and recrystallization. Second, the even dispersion of alloying elements brought about by mechanical alloying improves the stability and characteristics of both precipitation-hardened and solid-solution strengthened alloys at high temperatures. Materials that have been mechanically alloyed are also highly resistant to hot corrosion and oxidation [45].

In mechanical alloying (MA) technology, three possible metal and alloy combinations are considered: (1) brittle-brittle, (2) ductile-brittle, and (3) ductile-ductile.

In the brittle-brittle category, the lesser brittle component becomes embedded in the more brittle component as it is milled. As such, the hard particles of Si are embedded in the soft Ge matrix in Si-Ge (Figure 2.2) and Mn-Bi brittle-brittle component systems [47]. While milling brittle components, the potential mechanisms that could aid in the transfer of material is plastic deformation, mainly enabled by surface deformation, micro-deformation in volumes free of defects, and increase in local temperature [45,47].

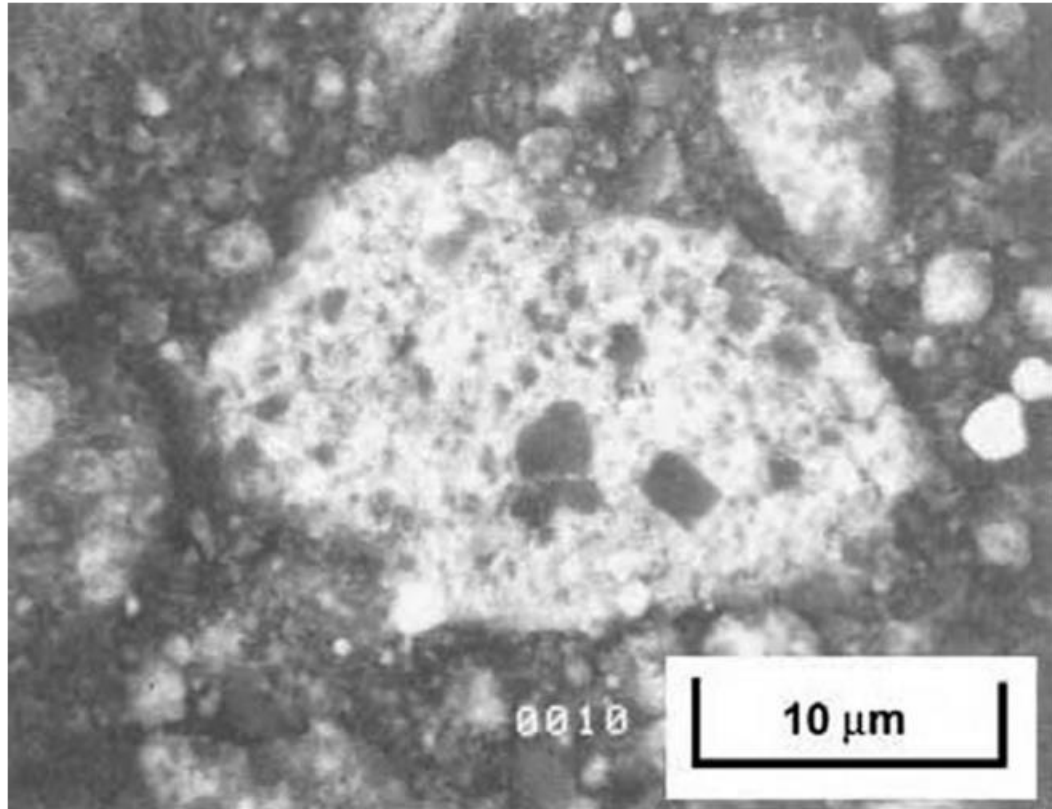


Figure 2.2: SEM image demonstrating the incorporation of the hard Si particles into the softer Ge matrix during a 12-hour mechanical alloying process of the Si-Ge powder mixture [45,47].

Traditional ODS alloys fall into the ductile-brittle group because brittle oxide particles are scattered throughout the ductile matrix. Ball-powder impacts during the early phases of milling flatten the ductile metal powder particles while breaking apart the intermetallic particles or brittle oxide. The ductile components tend to occlude and confine these broken, brittle particles inside. The ductile powder particles become work-hardened resulting in the refined and complicated lamellae formation with additional milling. Each particle's composition gradually approaches that of the initial powder blend. As an ODS alloy is milled further, the lamellae become more refined, the interlamellar spacing reduces, along

with the brittle particles becoming evenly distributed throughout the ductile matrix. TEM image of an α_2 -titanium aluminide matrix with the dispersion of Er_2O_3 in it that has been mechanically milled is depicted in Figure 2.3 [45,48].

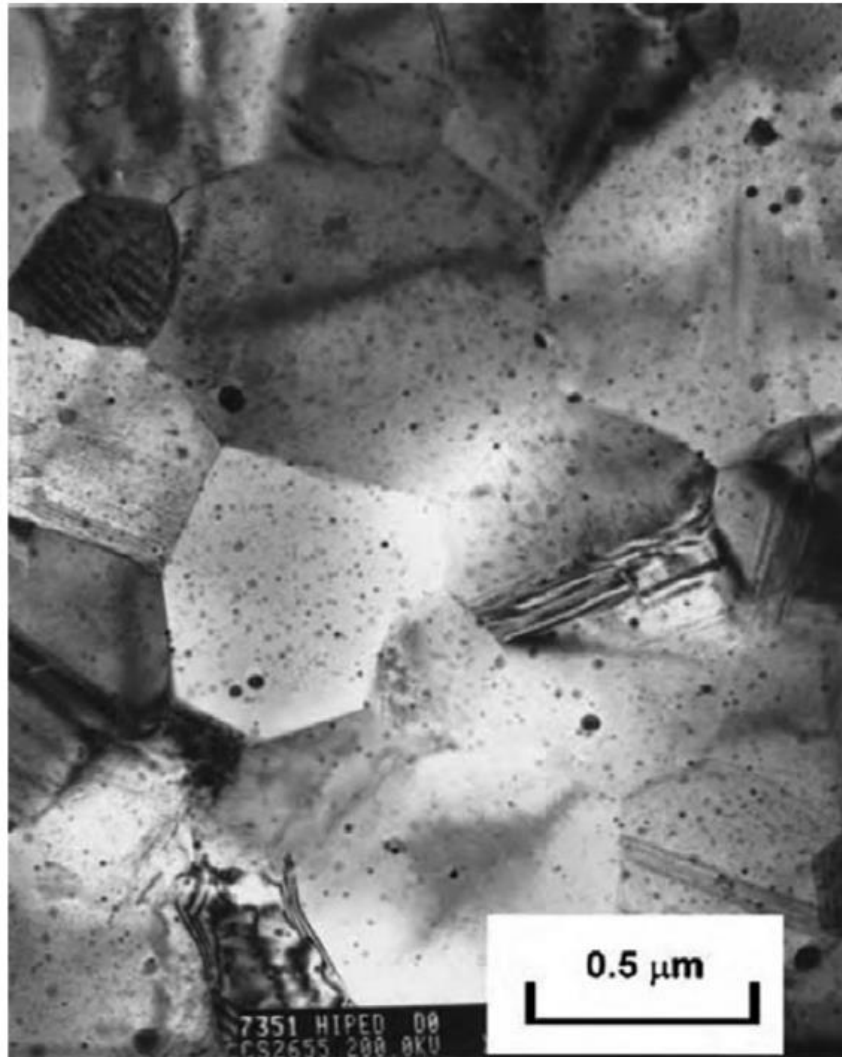


Figure 2.3: TEM image of a mechanically milled α_2 -titanium aluminide matrix with the dispersion of Er_2O_3 in it [45,48].

The best kind of material combination for mechanical alloying is ductile-ductile. Initially, the particles get flattened and may also fuse onto the ball surfaces. The benefit of this

powder coating on the grinding medium is that it keeps the medium from wearing down too much. Subsequently, the flattened particles undergo cold welding to create a composite lamellar structure consisting of the individual metals. The work hardening, hardness, and fragmentation of the composite powder particles increase with increasing mechanical alloying time, leading to particles with increasingly equiaxed dimensions. As the material is milled further, the welded layer's elemental lamellae and the coarse and fine powders stop being linear and instead become convoluted (Figure 2.4). The reason for this is because equiaxed powder particles randomly fuse together, showing no bias in the orientation in which they fuse. At this point, alloying starts to happen because of a combination of higher lattice defect density, reduced interlamellar spacing, and any possible heating during the process of milling. At this point, the particle size and hardness typically achieve a saturation value. Real alloying happens at atomic levels with additional milling, forming intermetallics, solid solutions, or maybe amorphous phases. The rate of mechanical energy is applied in the process and the rate at which the material being processed work hardens are two factors that affect the rate of refinement of microstructure, as was discussed in [45,49].

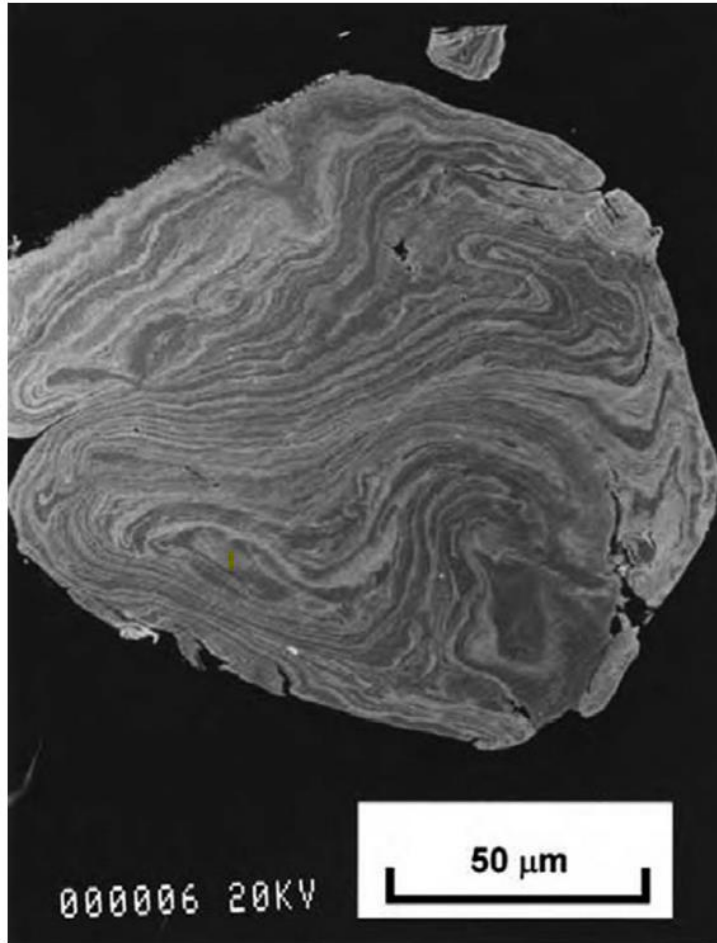


Figure 2.4: SEM image illustrating the complex lamellar structure produced by milling a ductile-ductile component system (Ag-Cu) [45].

2.5 Process Variables in Mechanical Alloying (MA)

Since mechanical alloying is a complicated process, achieving the intended product phase and/or microstructure requires optimizing several variables. The milling time, material type, material size, milling speed, process control agent, type of mill, milling container, milling atmosphere, grinding medium size, vial fill level, ball-to-powder weight ratio, and milling temperature are some of the significant factors that affect the final composition of the powder [50].

2.5.1 Type of mill

For performing MA, there are several types of mills available. These mills vary in terms of capacity, operating speed, and controllability—that is, the degree to which contamination of the powders may be minimized. A suitable mill can be selected according to the type of powder, the amount of powder, and the final constitution desired [50].

2.5.2 Milling receptacles

The material chosen for the milling container is crucial since some of its material might dislodge and get added into the powder because of the grinding medium's impact on the interior surface of the container. This may contaminate the powder and change its chemical composition. There is a chance that the powder will become contaminated if the material with which grinding vessel is made and the powder are different. Conversely, if the two materials are identical, the chemistry can change unless appropriate measures are implemented to offset the increased quantity of the element added to the powder. Bearing steel, tempered steel, hardened chromium steel, tool steel, WC-Co, hardened steel, stainless steel, and WC-lined steel [51], are the most frequent materials used for the grinding vessels [50].

2.5.3 Milling speed

It is simple to understand that the energy transferred to the powder would increase with the rotational speed of the mill. However, there are restrictions on the highest speed that can be used, depending on the milling machine design. For instance, raising the rotational speed

in a traditional ball mill will accelerate the ball movement. The balls will become stuck to the interior surface of the vial over a certain speed and cannot drop to produce any impact force. To ensure that the balls fall from the highest height and generate the most collision energy, the maximum speed should be set slightly below the critical velocity [50].

A further constraint on the maximum speed of milling is that the temperature within the vial may rise to a high level. When diffusion is needed to encourage homogeneity and/or alloying in the powders, this could be useful in such circumstances. However, there are some situations in which this temperature increase could be detrimental since it speeds up the transformation process and causes the breakdown of additional metastable phases or supersaturated solid solutions that were created during milling [52]. Furthermore, the powders could become contaminated due to the elevated temperatures produced. According to reports, the improved dynamic recrystallization during nanocrystal formation causes the average crystal size to grow along with the internal strain to decrease at higher milling speeds [53]. The highest temperature that can be reached varies greatly depending on the type of mill.

2.5.4 Milling duration

The milling time is the most crucial factor. The duration is often set to produce a constant condition between the powder particles' fracture and cold welding. Several factors affect the amount of time needed: ball-to-powder ratio, milling intensity, temperature, and kind of mill. For every combination of the aforementioned characteristics and for any specific

powder system, these timings must be determined. However, if the milling of powder is done for longer than necessary, It should be understood that the amount of contamination rises, and some undesired phases develop [54]. Therefore, it is preferable that the powder be milled for only the amount of time needed, and no more [50].

2.5.5 Grinding media

Stainless steel, WC-Co, tool steel, hardened steel, tempered steel, bearing steel, and hardened chromium steel are the most frequent materials used as grinding media. To ensure the balls exert sufficient force on powders, the grinding media's density must be high. To prevent cross contamination, it is ideal to use the same material for both the grinding medium and the grinding vessel for milling the powders [50].

The effectiveness of milling is also influenced by the size of the grinding medium. Since the heavier balls will impart greater impact energy to the powder particles, the high density and large size of the grinding media are often beneficial. Additionally, it has been stated that the size of the grinding media utilized affects the final composition of the powder. For instance, a solid solution of Al in Ti was created after milling a blended elemental Ti-Al particle mixture using balls with a diameter of 15 mm. However, even after a lengthy milling period, the usage of balls with a diameter of 20 and 25 mm produced a mixture of just the Ti and Al phases [55]. A different set of studies [56,57] revealed that utilizing steel balls with a 3/16'' diameter instead of 3/4'' diameter could result in the production of an amorphous phase in Ti-Al alloys more quickly. In fact, when milling was carried out with

large steel balls, in certain instances a stable crystalline compound was developed, and no amorphous phase was created [56].

2.5.6 Weight of balls to powder ratio

An essential factor in the milling process is the ball to powder particles ratio (BPR) which is the ratio of weight of balls to that of powders, also known as the charge ratio (CR). If the powder is to be milled in a small capacity mill, like a SPEX mill, a ratio of 10:1 is typically utilized. However, a larger BPR of 50:1 or maybe 100:1 is employed when milling is done in a higher capacity mill, such as an attritor mill. The amount of time needed to reach a certain phase in the milled powder particle is greatly influenced by the BPR. The necessary time decreases with increasing BPR. For instance, milling of Ti-33at.%Al powder mixture in a SPEX mill, an amorphous phase was formed in 7 hours with a 10:1 BPR, in 2 hours with a 50:1 BPR, and in 1 hour with a 100:1 BPR [58]. A high BPR causes more collisions per unit of time due to an increase in the weight of balls in proportion to that of powders. This increases the energy imparted to the powder particles, hastening the alloying process [50].

2.5.7 Filling level of the vial

The impact forces applied to the powder particles cause them to alloy, thus it's important that the powder particles and the balls have adequate room to freely move inside the milling container. A very small production rate results from a very little quantity of powder particles and balls. Conversely, if the amount is high, the balls will not have enough room

to move about, which will reduce the impact energy. As a result, caution must be used to avoid filling the vial too much; typically, about half of the vial is left empty [50].

2.5.8 Milling environment

The contamination of the powder particles happens mainly because of the milling environment. As a result, milling of powders is done in vessels that have either been sealed vacuum shut or filled up with inert gases like helium or argon. Nitrogen can form nitrides during milling which is undesirable. The most popular ambient to stop powder particle contamination and/or oxidation is high-purity argon. Typically, atmosphere-controlled glove boxes are used for the loading and unloading of the milling vial with powder particles. Usually, the argon gas in these glove boxes is periodically replaced after being evacuated. In certain cases, investigators have gone so far as to perform the milling process inside of glove boxes that have been evacuated [50].

Various milling atmospheres have been employed for distinct objectives. Nitrides have been produced in ammonia or nitrogen atmospheres [59,60]. Hydrides were created using a hydrogen atmosphere [61]. It has been demonstrated that milling in presence of air in vial causes the powder to generate nitrides and oxides, particularly if the powder is reactive. Consequently, when milling, care must be made to employ an inert atmosphere [50].

2.5.9 Role of surfactants in mechanical milling/ alloying

Surfactants, also known as process controlling agents (PCAs), are used in mechanical milling to reduce metal-to-metal contact by adhering to the particle surface and becoming adsorbed there. This reduces cold welding and eventually causes more particle fracturing. The surfactant molecules are shown in Figure 2.5 adhering to the particle surface. To prevent cold welding of particles, surfactants deposited onto the particle surface lower the surface energy of newly broken surfaces. The inclusion of surfactants during milling results in a large increase in powder yield, which lowers the cost of material processing. Surfactant addition during milling, however, may have unfavorable consequences such as contamination of powder particles and sluggish homogeneity in the particle microstructure during alloy formation. The ductility of the particles, their quantity, their milling time, their initial size, and the chemical and thermal stability of the surfactants all influence how much surfactant should be used in the milling process [62].

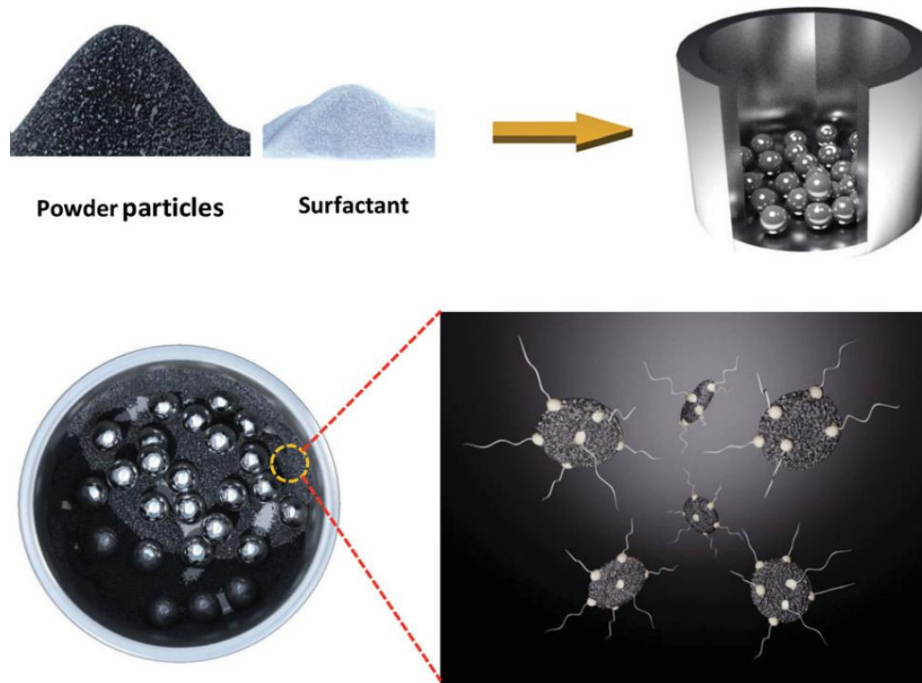


Figure 2.5: An illustration of the functioning of surfactant in the mechanical alloying/milling process [62].

Depending on the required level of purity and the type of powder to be ground (brittle or soft), a surfactant must be selected. Surfactants typically make up 1-5 wt.% of the overall powder charge when utilized in the mechanical alloying/milling process. Excessive cold-welding still happens when a modest amount of surfactant is used because only a small portion of the particle's surface gets covered. However, a significant amount of surfactant may coat the entire particle surface and cause the system to fracture more than cold welding would. A significant reduction in the friction coefficient between the powder particles and colliding balls occurs when a high amount of surfactant is added in a brief milling time. Also, the kinetic energy of milling balls gets consumed to overcome the frictional force and produce a flaky-shaped particle morphology [63,64]. It should be mentioned that using a lot of surfactant inhibits the creation of new materials and slows down the alloying

process, even though it produces fine, uniformly shaped particles after extended milling times. However, an appropriate amount of surfactant may coat the powder particle surface, resulting in a balance between fracture and cold welding [62]. For instance, according to Hiraga et. Al, the small particles (9.2 μm) produced by employing 3 wt.% methanol as surfactant did not meet the necessary plasma spraying application, while the larger particles (44.7 μm) created by using 2 wt.% methanol were well suited to plasma spraying [65].

Reducing the size of crystallites is largely dependent on the application of surfactants, especially in the initial phases of milling [66-69]. The bigger crystallite size estimated for a milled sample without surfactants may have resulted from the comparatively higher temperature attained during milling [67]. Heat is produced from the energy used to reduce the frictional force between powder particles. The elastic deformation of the vials and grinding media along with the plastic deformation of particles also produce heat. When the powder particle temperature rises over a particular point without the presence of a surfactant (lubricating agent) during milling, the powder particles may recover and recrystallize [70].

2.5.10 Milling temperature

Any alloy system is likely to be significantly impacted by the milling temperature since diffusion processes play a role in the creation of alloy phases, regardless of whether the final product phase is an amorphous phase, intermetallic phase, solid solution, or nanostructure phase. Only a small number of studies using purposeful temperature

variations during milling have been published. This was accomplished by either heating the milling vial electrically to raise the milling temperature or by dropping liquid nitrogen into the milling vial to decrease the milling temperature [50].

These studies were conducted to find out if a nanocrystalline structure or an amorphous phase occurs at different temperatures, or to investigate how the temperature of milling affects the variance in solid solubility levels. It was noted that for higher temperature milling of materials, the grain size was bigger and the root mean square (rms) strain for the material was less during the creation of nanocrystals [71]. Regarding the development of an amorphous phase in relation to milling temperature, there have been differing reports. Amorphization during MA is characterized by the development of micro-diffusion couplings of the component powders and a solid-state amorphization process. Therefore, the amorphization kinetics gets improved by increased milling temperatures. In the Ni-Zr [72] and Ni-Ti [73] systems, this has been noted. When a Ni-50 at.% Zr powder mixture was processed in a vibrating mill for 15 hours at liquid nitrogen temperature, no amorphous phase development was seen. However, at 200° C, milling for the same amount of time resulted in the production of a totally amorphous phase and at ambient temperature, milling produced a partially amorphous phase [50].

By a different process than during MA, as an amorphous phase is formed during MM. Amorphization during MM is caused by a rise in the crystalline phase's free energy brought about by defects such as larger grain boundary area or anti-site chemical disorder due to creation of a nanocrystalline structure. Amorphization is therefore predicted to be favored by lower milling temperatures. As the temperature was raised during the NiTi intermetallic

milling process, Koch et al. [74,75] observed decreased amorphization kinetics. It took 2 hours for the material to amorphize at liquid nitrogen temperature, but it took 18 hours to amorphize at 220° C [50].

2.6 Types of mills

Mechanically alloyed powders are created using several kinds of high-energy milling machinery. They vary in terms of capacity, milling efficiency, and supplementary arrangements for heating and cooling [50].

2.6.1 SPEX[®] shaker mill

Typically, SPEX[®] shaker mills (Figure 2.6) are utilized for alloy screening and laboratory research, milling roughly 10–20 g of powder particles at a time. The manufacturer of these mills is SPEX[®] CertPrep, located in Metuchen, NJ. This mill contains a single vial, clamped in place that swings vigorously back and forth several thousand times per minute, carrying the grinding balls and sample. The vial appears to be moving in the shape of an infinity sign or figure 8 when it combines the back-and-forth shaking action with lateral motions of the vial's ends. The balls mill and mix the sample as they strike the end of vial and the sample with each swing of the vial [50].

This machine has forced cooling built in to allow for longer milling durations. The SPEX[®] mills can be used with a wide range of vial materials, such as plastic, methacrylate, tungsten carbide, silicon nitride, agate, alumina, hardened steel, and zirconia [50].



Figure 2.6: SPEX[®] 8000 mixer/mill [50].

2.6.2 Planetary ball mill

A planetary ball mill, which can mill a few hundred grams of powder at a time, is another common mill used for MA research (Figure 2.7a). These are sold in the US and Canada by Gilson Co. and are produced in Germany by Fritsch GmbH. The movement of the milling vials in the planetary ball mill is what gives it its name. They rotate about their own axes owing to a unique driving system, which is mounted on a rotating support disk. Because the supporting disk and the vials revolve in opposing orientations, the centrifugal forces operate in opposite and similar directions on alternate occasions. As a result, there is a friction effect as the grinding balls go down the vial's inner wall, an impact effect when the

material is milled followed by the lift off of the grinding balls to travel through the vial's inner chamber freely and collide with the opposing inner wall as seen in Figure 2.7b. In the SPEX[®] mills, impacts occur even more frequently. Therefore, planetary ball mills have lower energy when compared to SPEX mills [50].

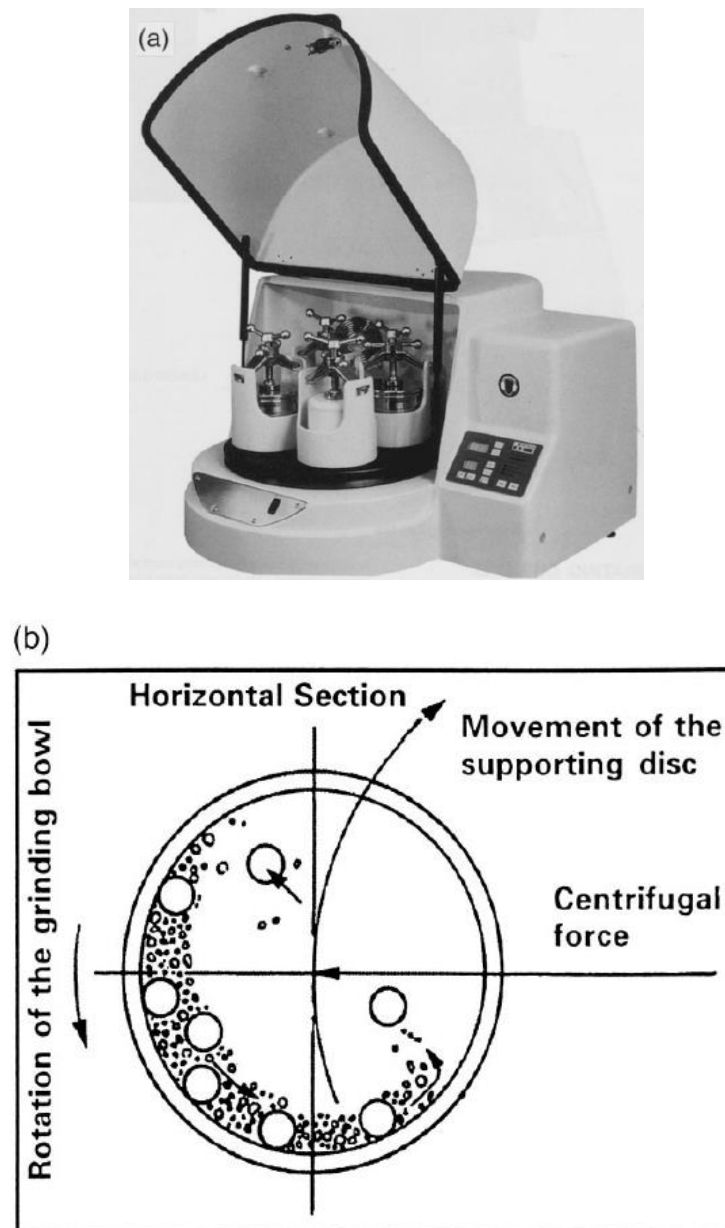


Figure 2.7(a) A P-5 four station ball milling machine Fritsch Pulverisette; and (b) diagram showing motion of the balls move within the ball mill. [50].

2.6.3 Attritor mill

An attritor, a type of ball mill that may produce higher energies, is made out of a vertical drum that has several impellers inside of it. The impellers, which are progressively arranged at right angles to one another, energize the ball charge and reduce the particle size as a result of impacts. It appears that ball sliding and interparticle collisions contribute to some size decrease. The steel balls inside the drum are stirred by the impellers, which are rotated by a strong motor. Large amounts of powder, ranging from roughly 0.5 to 40 kg, can be ground at a time in attritor mills (Figure 2.8). Union Process, located in Akron, Ohio, offers commercial attritors for purchase. These are low energy mills as compared to both planetary and SPEX[®] mills [50].

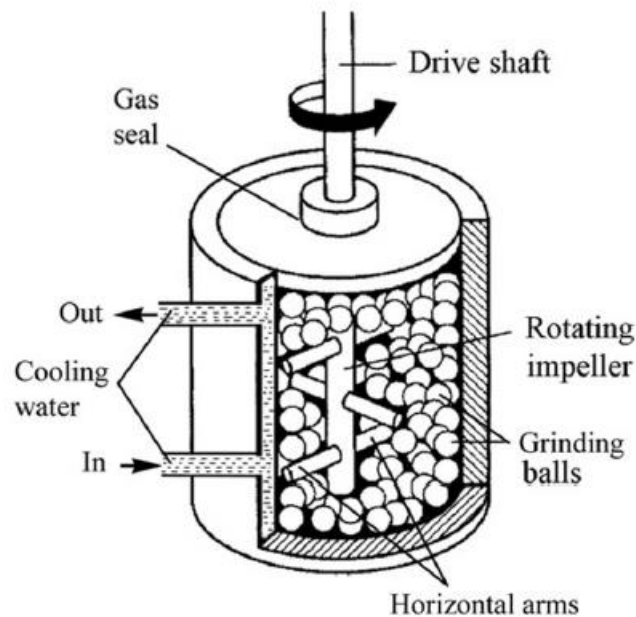


Figure 2.8: An illustration of a vertical attritor including a rotating impeller [45].

2.6.4 Commercial mills

Compared to the above-discussed mills, commercial tumble ball mills for mechanical alloying are substantially larger and have a processing capacity of several hundred kg to one ton at a time. The specific energy of the milling machine decreases as the milling time increases. As a result, a process that just takes a few minutes in a planetary mill and a few hours in attritor mill may take a few days in commercial tumbling ball mills. The sizes of commercial batch NETZSCH® attritors utilized in industry today range from 115 to 720 L [50].

2.7 Material selection for current research

The aim of the current work is to produce Ni(Zn)-alumina composite particles with desired characteristics for their potential use as feedstock in LPCS/HPCS by using HE-MA as a feedstock synthesis technology. The production of nanostructured metal-ceramic composites is studied using mechanical milling to create deposits in a cutting-edge cold spray additive manufacturing (CSAM) method. The service life of components is extended by the nanostructured metal-ceramic composites, which combine the advantages of ceramics (exceptional wear resistance and chemical stability) and metals (excellent strength and toughness). Nickel(zinc) substitutional alloy over its parent element, nickel, has been suggested in the current research work. Zinc atoms contribute to the lattice strains in the FCC crystal structure by taking up some of the nickel's lattice locations. In order to block dislocations and provide alloy strength, these lattice strains may be significant. Moreover, Ni(Zn) alloys used in this research have a high melting point close to 1400° C which makes them suitable for high temperature applications. The properties of aluminum

oxide (Al_2O_3) include strength, hardness, and chemical inertness. Because of exceptional thermal, chemical resistance, and high hardness of alumina it is discovered to be a good reinforcement for enhancing wear resistance of metallic matrix at high temperatures [76]. It can be found in nature in both metastable forms such as κ , η , θ , δ , β , and X, as well as in hydrated phases such as diaspor ($\alpha\text{-Al}_2\text{O}_3\cdot 3\text{H}_2\text{O}$) and boehmite ($\gamma\text{-Al}_2\text{O}_3\cdot \text{H}_2\text{O}$). The $\alpha\text{-Al}_2\text{O}_3$, least porous phase, is found in nature as corundum and is known to be stable at temperatures of approximately 1200°C [5,50,76-78]. When paired with Ni(Zn) substitutional alloy, the appealing qualities of Al_2O_3 may find use in the mining, aerospace, petrochemical, renewable energy, as well as gas turbine industries.

Ni-Zn-alumina particles were cold-sprayed onto an Al7075 substrate by Koray Kilicay et al. (2021) in order to repair damaged metallic components and lower the cost of replacement [79]. A primary distinction between the current work and [79] is the material design. In [79], discrete nickel, zinc, and alumina particles were mixed and sprayed onto an Al7075 substrate. Ni-Zn-alumina coatings were shown to have better mechanical and tribological performances than Al7075 substrate [79]. However, since the particles were discrete the homogeneous dispersion of alumina was not achieved in the Ni-Zn-alumina cold spray coating fabricated by Koray Kilicay et al. Also examined by Koray Kilicay et al. (2020) was the high-temperature oxidation resistance of Ni-Zn-alumina MMC coatings sprayed over TZM molybdenum alloy. According to reports, Zn and Ni formed matching zinc oxide (ZnO) and nickel oxide (NiO), which enhanced the TZM alloy's resistance to high-temperature oxidation and expanded its range of commercial applications by keeping oxygen from penetrating the alloy at higher temperatures [80]. Therefore, in this current

research, the focus is on designing and synthesis of Ni(Zn)-alumina particle feedstock with uniform embedment of alumina grains in the metal matrix. These composite particles upon cold spraying shall improve the desired mechanical and tribological properties of the cold spray coatings due to the uniformly distributed alumina ceramic grains in the coatings.

2.8 Applications

Mechanically alloyed materials enjoy extensive industrial use in aerospace, glass processing, power engineering, thermal processing, and related fields. The foundation of these applications is the capacity of MA to create materials having metastable phases, including amorphous alloys, nonequilibrium quasi-crystalline or crystalline intermediate phases, and supersaturated solid solutions [45].

The following discusses the key MA advancements in dispersion reinforced nickel, copper, cobalt and aluminum base alloys:

2.8.1 Nickel based alloys

The primary applications for the nickel-base superalloys from MA are in gas turbine engine parts and sheets used in corrosive and oxidizing environments. As a result, MA 754 is mostly used in aviation gas turbine engines as vanes and bands. Aero engine band assemblies and the brazed nozzle guide vane are other applications for it. For these uses, the main benefits of these alloys are its high melting point, resistance to creep, and resistance to thermal fatigue. Due to its high chromium content and ability to withstand high temperatures, the alloy MA 758 is designed for use in many industrial applications.

For radiant tube applications, alloy MA 754 tubing with a large diameter and thin wall has been created and tested. Heat exchangers and other industrial equipment working at extremely high temperatures have utilized Alloy MA 758 tubing [45].

2.8.2 Copper based alloys

MA copper alloys are mostly used in electrical applications. The electrodes used in electro-erosion and welding operations are particularly noteworthy since their extended lifespans allow for lower costs and higher output [81]. As hard magnets, Cu-Fe-Co alloys are thought to have valuable magnetic characteristics and can be applied in a variety of fields [82-85].

Hard magnets in a variety of applications can be made using Cu-Fe-Co alloys, which possess advantageous magnetic characteristics [82-85]. A copper, iron, and cobalt powder mixture with a mass proportion of 50:25:25 served as the beginning material for the endeavor [82]. Alumina with a particle size of around 1 mm was the alloyed component chosen to be added at 1, 3, and 10 weight percentages. Different milling periods of 3, 8, 10, and 16 hours satisfied the MA process. The coercive field value, H_c , and the electro-erosion maximum energy product, BH_{max} , grew quickly up until three hours into the milling process, then abruptly decreased, and then decreased more slowly and continuously as a result of decrease in crystallite size, as the authors stated [82]. Cu-Fe-Co powder that had alumina added to it had higher H_c and BH_{max} values. However, the values only slightly increased when the alumina concentration was above 3%, going from 8,326,666 to 8,637,051 A/m for the former and from 186,086 to 194,391 J/m² for the latter.

2.8.3 Cobalt based alloys

Oral and orthopedic surgery currently uses cobalt-base alloys as their primary materials. To be effective in replacing a bodily component, biomaterial alloys need to exhibit the best possible combination of corrosion resistance, wear resistance, fatigue, and strength. For joint replacement, a surgical implant, like a dental implant, needs to fulfill biological prerequisites. The alloys in the CoCrMoC system respond to these requirements. Co-27Cr-6Mo-0.25C biomedical alloy was created by mechanical alloying, as reported by Sainchez-De Jesu's et al. Drawing from over 40 years of clinical experience in oral and orthopedic surgery, this alloy is currently one of the preferred materials for wrought and cast metallic implants; it additionally achieved standardization. Because of its great strength, it is a preferred metallic material [45].

2.8.4 Aluminum based alloys

Compared to a traditional age-hardening aluminum alloy of similar strength, like Alloy 2024, the IncoMAP[®] AL-9052 alloy offers a density which is 5% lower. Its excellent strength, low weight, and resistance to corrosion make it a valuable material for aeronautical applications. The ultra-lightweight IncoMAP[®] AL-905XL alloy is created by adding lithium with mechanically alloyed aluminum alloys. Compared to the age-hardening 7075-T73 alloy having equivalent strength, it has a 10% higher stiffness and a lower density. This alloy can be applied to airframes due to its exceptional combination of characteristics [45]. High-strength aluminum-titanium alloys have recently been created using MA through the dispersion of Al₃Ti intermetallic particles either nanometer- or submicron-sized in an aluminum matrix, along with Al₂O₃ and Al₄C₃ dispersoids through

the incorporation of PCAs. To create high-strength alloys in different systems, comparable methods could be applied. In the Al-10Ti alloy produced by MA, high mechanical properties were generated. 1.5 wt.% wax was added during attrition milling a mixture of 10 wt.% titanium powders and aluminum [45].

2.9 Cold gas dynamic spray (CGDS) technology

In the 1980s, the Institute for Theoretical and Applied Mechanics in the Siberian section with the Russian Academy of Science in Novosibirsk made the discovery of the CGDS technology [86,87]. The method has undergone multiple revisions over the years, mostly owing to its exceptional capacity to deform solid particulate materials based just on the kinetic energy of the particles. It is challenging for technology to perform at a level where the industries expect components to be built with outstanding mechanical, tribological, and environmental attributes. Polymers, ceramics, metals, and alloys are among the feedstock and substrate materials that the CS technology may be able to work with [80,88,89]. Additionally, in comparison to other thermal spray techniques, the CS process offers less chance of high temperature phase transformations and oxide formations, making it useful for handling materials that are sensitive to oxygen [90]. By offering remarkable mechanical, corrosion resistance and wear resistance properties the CS coatings applied to substrates can lower the cost of replacing many kinds of widely used metallic components. The CS procedure is depicted in Figure 2.9.

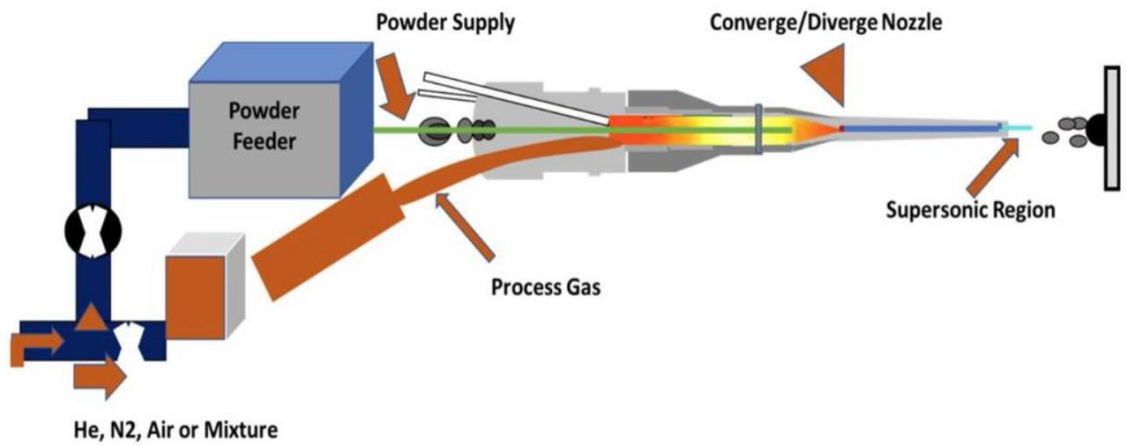


Figure 2.9: An image showing the cold spray process [91].

Particles less than 100 micrometers are ideal for cold spray applications. It is difficult to accelerate particles larger than 100 micrometers [92]. With respect to metallic and MMC compositions, Figure 2.10 displays a range of particle sizes and illustrates their efficacy in CS deposition.

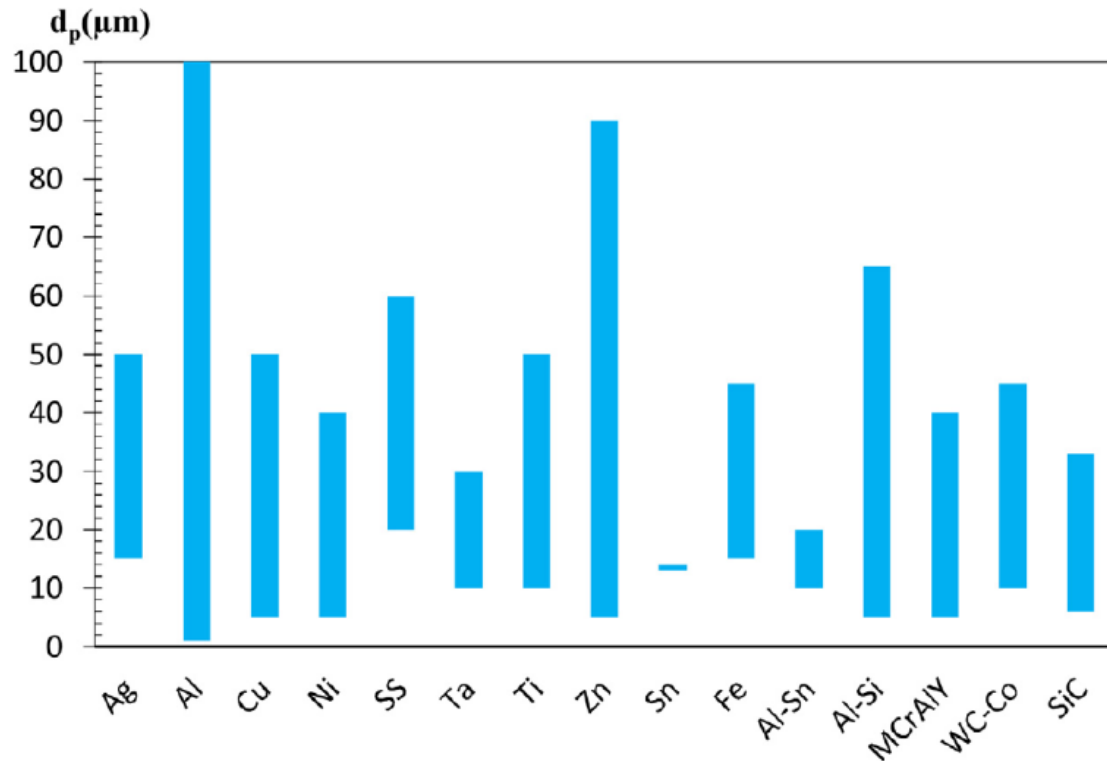


Figure 2.10: Typical particle diameter range for several materials in CGDS research studies [92].

Notwithstanding the fact that spherical particles have long been regarded as standard powders, the cold spray method is not limited to using them. Additionally, irregular morphologies such as angular and dendritic geometries can also be utilized as powder feedstock. Typically, atomization is used to create spherical powders, while cryomilling is used to produce angular particles. Using an electrolytic manufacturing process, dendritic powders are produced. Studies employing irregular particles demonstrated a significant increase in DE. When the deposition circumstances and granulometry are the same, they yield a higher in-flight velocity than spherical powders [93,94]. Uneven particles are able to achieve the maximum velocities when similar deposition parameters and powder

granulometry are used [95]. The increased drag coefficient of irregular powders is ascribed to the rapid separation of the boundary layers across the surface of the irregular particles, which causes the kinematic gain. Particles can achieve high velocities due to the substantial drag force caused by a negative pressure gradient created by a greater drag coefficient [95,96]. Consequently, the uneven shape reduces the porosity within the coating and enhances the efficiency of deposition. As a result, it might also make the coating harder [94,95].

2.10 Summary

MMCs are of great commercial importance due to mechanical, thermomechanical, physicochemical, tribological and corrosion resistance properties. Ball milling is an effective method to design and synthesize MMC particles to be used as a feedstock for CGDS process. A variety of compositions with varying milling parameters can help in producing a particle feedstock with required above mentioned properties. Ball milling is a wonderful technique to ensure homogeneous dispersion of second phase particles inside the metal or alloy matrix. Out of the different kinds of mills available, SPEX[®] mill shall be utilized for this research aiming at producing Ni(Zn)-alumina composite particles for cold spray process. The use of substitutional alloy Ni(Zn) alloy with the incorporation of alumina ceramic grains in the alloy matrix by HE-MA is a novel composition designed to overcome the limitations of the research performed by other researchers who used discrete nickel, zinc and alumina particles and blended them all together to fabricate a cold spray coating. This research gap opens new avenues for the application of HEMA to produce an

ideal particle feedstock for CGDS process that can provide uniform mechanical, tribological, and corrosion resistance properties.

Chapter 3 Research Methodology

This research focuses on the design, synthesis and microstructural characterization of Ni(Zn)-alumina particles produced by high energy mechanical alloying method for its potential use as particle feedstock for CSAM process.

3.1 Milling methodology for Ni(Zn)- α -alumina particle synthesis

Ni(Zn) alloy pieces (of initial size 1-10 mm) with two different compositions Ni(5wt.%Zn) and Ni(10wt.%Zn) were obtained from American Elements company. Also, α -alumina particles with 99.9% purity were obtained from Atlantic Equipment Engineers NJ [Appendix A]. The Ni(Zn) alloy as received had trace levels of Fe, Cd, and Pb (236.7, 10, and 10ppm respectively) in its chemical composition. Both the Ni(Zn) alloy pieces were pre-milled for 2 hours using 10 mm hardened steel balls at BPR of 7:1 and reduced to powder particles. 1wt.% stearic acid was used as surfactant in the milling mixture to avoid particle agglomeration and overheating. These Ni(Zn) alloy particles were then blended with α -alumina and milled again for three-time intervals of 1h, 2h, and 4h. A total of four alloy-ceramic compositions were made with 30 wt.% and 50 wt.% α -alumina contents. Hardened steel balls of 10 mm size and a BPR of 10:1 was used in the milling process to obtain Ni(Zn)-alumina composite particles. Again, 1 wt.% stearic acid was added to milling mixture to avoid agglomeration and overheating during milling. To avoid creating too much heat, the milling was done over a 4-hour period, with 10-minute pauses between each 30-minute cycle. To eliminate bias and machine variance-related errors, every experiment was conducted three times and then randomized. This led to the need to perform 48 sample

batches in all. An AirScience[®] Ductless Fume Hood was used to prepare and extract each sample. In order to sustain the effective BPR, ball weights were periodically modified to correspond with the weight of the removed specimen before milling more of the same composition. A material design-of-experiment (DoE) as shown in Table 3.1 shows the identification of the powder particle specimens and their milling settings.

Table 3.1: The identification of the powder particle specimens and their milling settings.

Alloy Composition (wt.%)	Specimen ID	Batch #	Alumina, wt.%	Time, hr.
Ni95Zn5	S1	1	30	1
Ni95Zn5	S2		30	2
Ni95Zn5	S3		30	4
Ni95Zn5	S4	2	50	1
Ni95Zn5	S5		50	2
Ni95Zn5	S6		50	4
Ni90Zn10	S7	3	30	1
Ni90Zn10	S8		30	2
Ni90Zn10	S9		30	4
Ni90Zn10	S10	4	50	1
Ni90Zn10	S11		50	2
Ni90Zn10	S12		50	4
Ni95Zn5	S13		0	4
Ni90Zn10	S14		0	4

3.2 Specimen characterization

The cross-sectional microstructure and morphology of milled powder particles were examined using secondary electron mode of Hitachi SU-70/Thermo Fisher Scios 2 Dual Beam Scanning Electron Microscope (SEM) and a JEOL 6400 SEM. The elemental makeup of the composite particles was investigated using energy dispersive spectroscopy (EDS) at 15 kV. Also, at a voltage of 20 kV, electron backscatter diffraction (EBSD) was conducted to examine the grain size distribution and plastic deformation of the alloy particles. The EBSD scan was conducted with a step size of 0.0202 μm for both Ni(5wt% Zn) and Ni(10 wt% Zn) alloy precursors and step size of 0.0404 μm for both Ni(5wt% Zn) and Ni(10 wt% Zn) pre-milled for 2 hours. A Malvern particle size analyzer (Model Mastersizer MAZ2000S, UK) was used to evaluate particle size distribution (PSD) of the milled powder particles using the laser diffraction method. With an accuracy of up to 0.6%, the analyzer has a size range was 10-nm to 3-mm. A Bruker D8 diffractometer X-ray diffraction (XRD) device was used to determine the crystalline phases in the milled powder particles. The specimens were scanned using Cu-K α radiation (1.5406 Å) at 25 mA and 40 kV over a 2θ range of 20°-80°, with 0.02° step size and 1 second step duration. An MDI Jade[®] 5.00 software was used to identify the XRD peaks.

3.3 Instrument details

3.3.1 SPEX[®] 8000M mixer/mill

In this research, for the synthesis of Ni(Zn)-alumina composite particles milling has been performed in SPEX[®] 8000M mill. These are laboratory mills used for milling a sample

batch of 10-15 grams at a time. A detailed description about this mill along with its image has already been provided in chapter 2, section 2.6.1.

3.3.2 Malvern particle analyzer

The Malvern particle analyzer (Model Mastersizer MAZ2000S, UK) is a tool used to quantify particle size and its distribution. By precisely forecasting the scattering pattern that is produced when a particle is passed via a laser beam, the apparatus measures the particle size. The Mie theory is the widely accepted hypothesis that describes how light scatters from every substance in any condition. Given particle-specific data, such as absorption and refractive index, Mie theory may predict the light scattering by spherical particles. The mastersizer uses an optical unit that can capture the scattering pattern of a field of particles and thereby calculating the particle size that creates such a pattern. As seen in figure 3.1, the Master sizer is composed of an optical bench with a wet cell, a computer system, and a sample dispersion unit (Hydro 2000S).

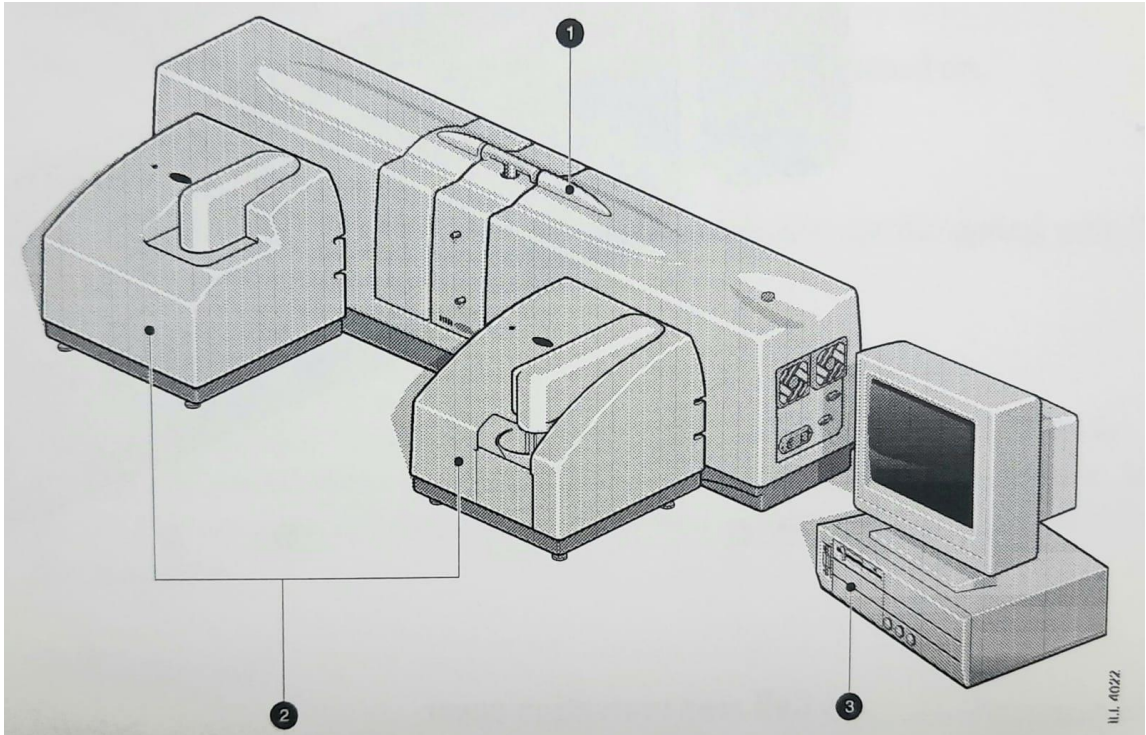


Figure 3.1: Malvern mastersizer MAZ2000S consisting of (1) Optical unit, (2) Sample dispersion accessory, and (3) computer system [image courtesy: Malvern instruments [97]]

3.3.3 Scanning electron microscopy (with EDS and EBSD)

Useful in both science and industry, a scanning electron microscope (SEM) allows for incredibly high magnification and resolution to examine the surface of objects. A focused electron beam is employed in SEMs instead of light, as in the optical microscope. Images with far better resolution are possible because electrons have wavelengths that are substantially shorter than visible light. SEMs produce their electron beam using an electron gun. After that, the beam is concentrated and directed over the sample surface. A small layer of conductive material, like carbon or gold, is frequently required to coat samples before they are placed in the SEM. In addition to enhancing image quality, this helps avoid charging effects. The surface of sample is scanned in a raster pattern by the electron beam. Different signals are produced when the beam interacts with the atoms on the surface. As

the electron beam interacts with the sample surface, several signals are gathered. The most prevalent signals are backscattered electrons, characteristic X-rays, and secondary electrons. The detectors in SEM subsequently pick up these signals and use them to produce an image of the surface. While backscattered electrons reveal information about the atomic structure and content of the material, secondary electrons offer precise information about the surface topography. SEMs may produce magnifications up to over 100,000x, which is a very large range. Scientists can view features in the micro- and nanoscale with the help of SEM images, which have a resolution of up to a few nanometers.

When analyzing the elemental composition of materials, energy dispersive X-ray spectroscopy, known as EDX or EDS, is often utilized along with scanning electron microscopes, or SEMs. Inner shell electrons in the atoms can be removed by the SEM electron beam when it interacts with the electrons in atoms on the surface of the sample. As a result, the electron shells develop "holes". In the process of filling these holes, electrons from the outer shell descend to lower energy levels, producing X-rays. In EDS, a detector located close to the sample gathers X-rays that the material emits. The detector is composed of semiconductor crystal, usually composed of silicon (lithium), which when exposed to X-rays produces electrical signals. As an electron moves from one energy level to another, each element releases characteristic X-rays at distinct energies. Since such energies are specific for every element, identification is possible. The EDS system measures and logs the energy of the X-rays that are detected. An energy spectrum is produced by processing the energy signals that the detector has detected. The intensity of X-rays observed at various energy levels is represented by this spectrum. A particular

element contained in the sample is represented by every peak in the spectrum. It is possible to ascertain the elemental composition of the specimen by examining the peaks in the spectrum and contrasting them with the known X-ray energies of various elements. Quantitative data regarding the proportional amount of each element is also provided by the peak intensities. Elemental maps of the surface of the sample may also be generated by EDS. By scanning the entire sample surface with the electron beam and gathering EDS data the distribution of various elements can be observed, providing spatial information about the composition of the sample [98,99].

In electron microscopy, the EBSD analysis is employed to examine the crystallographic characteristics of various materials. EBSD is a powerful technique for creating electron diffraction patterns of crystals, and material components. From the collected patterns, it is then possible to determine the chemistry of phases, the shape of the grains, and the crystallographic orientation, offering a comprehensive examination of the microstructure along with a strong correlation with the characteristics and performance of materials. In EBSD, a scanning electron microscope is utilized to direct a electron beam onto the sample surface. Electrons are dispersed in a variety of directions, including backscattering, when the electron beam interacts with the crystal structure of material. Because of interactions with the atomic lattice, electrons experience a change in momentum when they are backscattered. The crystallographic orientation of the specimen determines the direction and intensity of the backscattered electrons. A diffraction pattern is created when backscattered electrons are gathered by a detector above the sample. The material's crystallographic orientation at the site of interaction is revealed by this pattern. To ascertain

the material's crystallographic orientation, the diffraction pattern is examined. A theoretical pattern produced for various crystallographic orientations is compared to the experimental diffraction pattern in a procedure called indexing. The crystal lattice orientation is shown by the best match. EBSD may produce orientation maps that show the arrangement of crystallographic orientations within a material by moving the electron beam through the surface of sample and gathering EBSD data at each location. Information regarding crystallographic textures, grain boundaries, and other microstructural characteristics can be found on these maps. By examining the diffraction patterns acquired from various sample locations, EBSD can also be utilized for phase identification. It is possible to identify the existence of particular crystalline phases through contrasting such patterns with reference patterns for recognized phases. Individual grains inside a polycrystalline material can be characterized using EBSD. Analyzing grain shape, size, orientation, and distribution statistically can reveal information about the mechanical characteristics and performance of the material [99,100].

The scanning electron microscope used for this research is ThermoScientific™ Scios™ 2 Dualbeam™ (Thermo Scientific is the company, formerly known as FEI). It is equipped with an Oxford Ultim Max 170 EDS detector, and an Oxford Symmetry EBSD detector controller by the Aztec® software.

3.3.4 X-ray diffraction

X-ray diffraction (XRD) is a powerful analytical technique used to determine the atomic and molecular structure of crystalline materials. It relies on the principle of constructive interference of X-rays scattered by the atoms in a sample. When the X-rays strike the sample, they are scattered by the atoms' electron clouds. According to Bragg's law, this scattering will be constructive when the path difference between waves scattered from adjacent atomic planes is equal to an integer multiple of the X-ray wavelength.

$$n\lambda = 2d\sin\theta$$

The recorded intensities form a diffraction pattern, which consists of peaks corresponding to the constructive interference of X-rays scattered by different crystallographic planes in the sample. The positions and intensities of the diffraction peaks provide information about the crystal structure of the sample. By comparing the observed diffraction pattern with reference patterns from known crystal structures, the crystal structure of the sample can be determined. XRD typically uses a source of monochromatic X-rays, often generated by an X-ray tube. These X-rays have a well-defined wavelength, usually in the range of 0.5-2.5 angstroms [101].

The D8 X-ray diffractometer is the equipment used to perform the XRD work in this research.



Figure 3.2: A D8 X-ray diffractometer [image courtesy Bruker [102]]

3.4 Summary

The research methodology for the current research deals with design and synthesis of a variety of Ni(Zn)-alumina composite particles with different compositions and respective milling times. The Ni(Zn) alloy precursors are pre-milled for 2 hours to reduce them to micron size particles suitable for further milling to achieve the objective of synthesizing Ni(Zn)-alumina composite particles. The alloy particles and the subsequently synthesized composite particles specimens were subjected to material characterization, particle size distribution, and X-ray diffraction to investigate their microstructural properties in terms of its application for cold spray process.

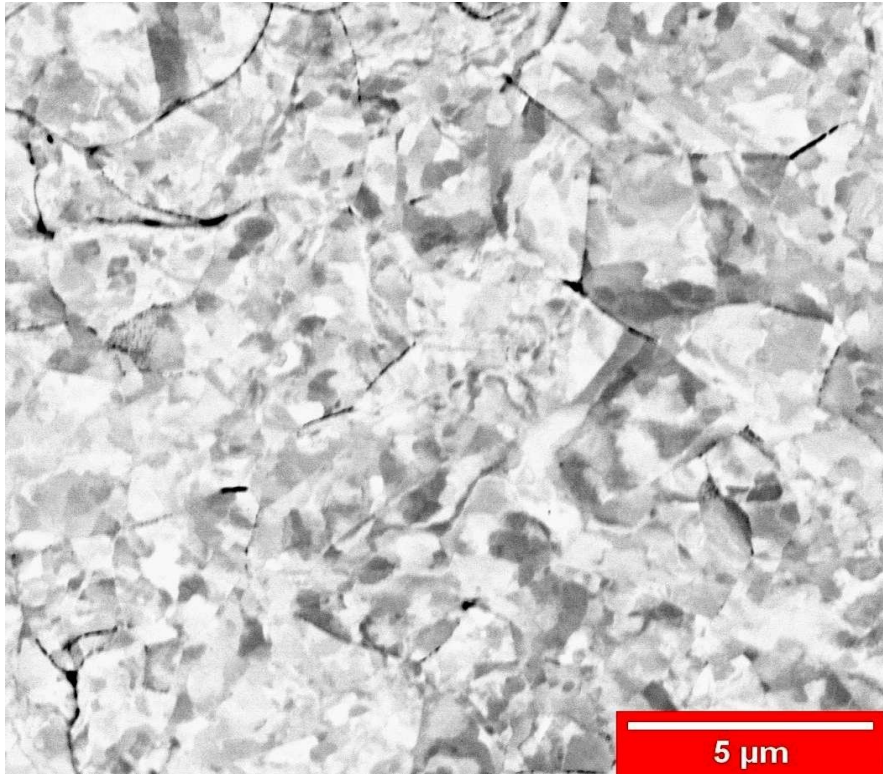
Chapter 4 Results and discussions

This chapter consists of the results and discussions pertaining to this research on the design, synthesis and microstructural characterization of Ni(Zn)-alumina composite particles. Firstly, the microstructural characterization of Ni(Zn) alloy precursors and the pre-milled Ni(Zn) particles are discussed, followed by the microstructural characterization of Ni(Zn)-alumina composite particles. The insightful results of microstructural characterization of Ni(Zn) alloy particles led to the planning, design and synthesis of Ni(Zn)-alumina composite particles with an aim to be utilized for CGDS process.

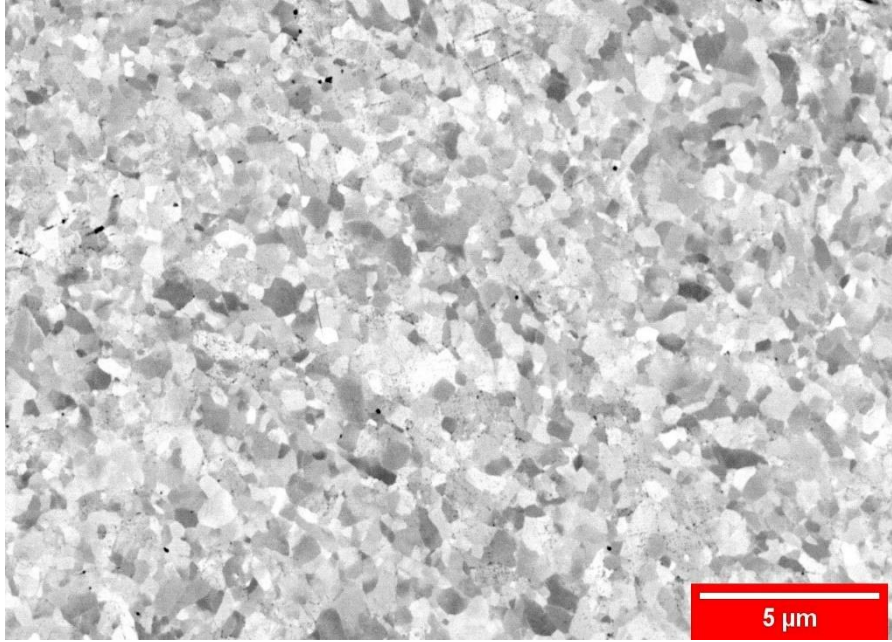
4.1 Microstructural characterization of as-received and pre-milled Ni(Zn) alloy precursors

The acquired Ni(Zn) alloy precursors used for the synthesis of Ni(Zn)- α -alumina composite particles can be seen in figure 4.1. Both the Ni(5wt.%Zn) and Ni(10wt.%Zn) alloys were etched for 30 seconds with aqua regia before observation under the SEM. The SEM images in backscatter mode of both Ni(Zn) alloys along with α -alumina grains demonstrate the presence of fine grains. The precursors that were acquired and milled by HE-MA method to create the composite particles are depicted in figure 4.1 The micrograph of the received α -Al₂O₃ particles and the back scattered SEM images of Ni(5wt.% Zn) and Ni(10wt.% Zn) etched with aqua regia for 30 s demonstrate the presence of tiny grains. In order to produce composite particles, both the Ni(Zn) alloy precursors were first pre-milled for 2 hours to produce a suitable alloy particle which can be used in the subsequent milling

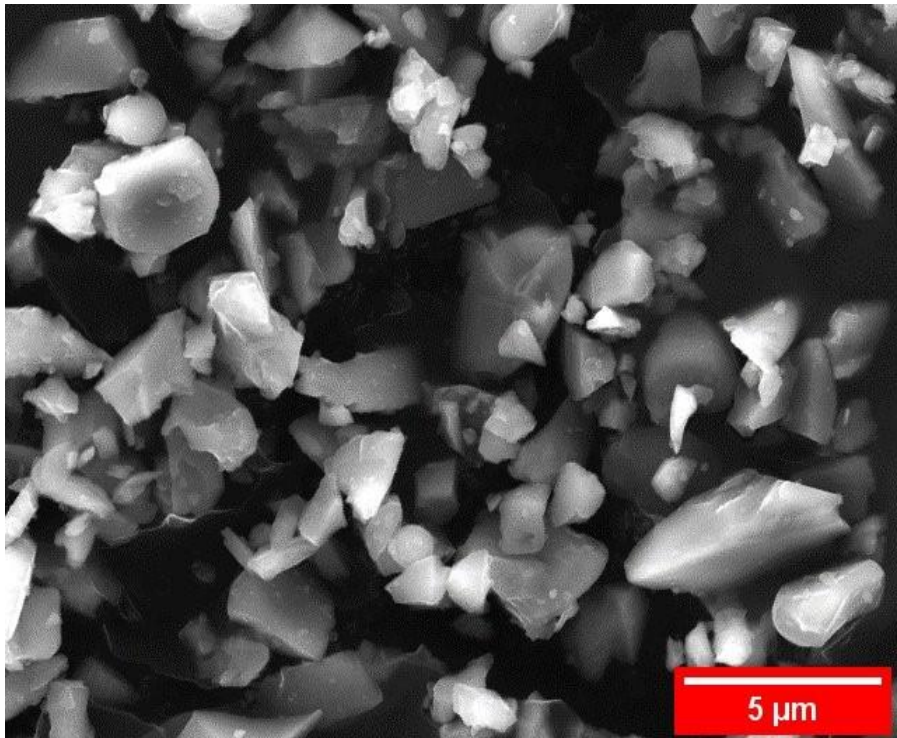
process. The objective was to enable the effective embedding of α -Al₂O₃ ceramic grains inside the Ni(Zn) alloy matrix.



(a)



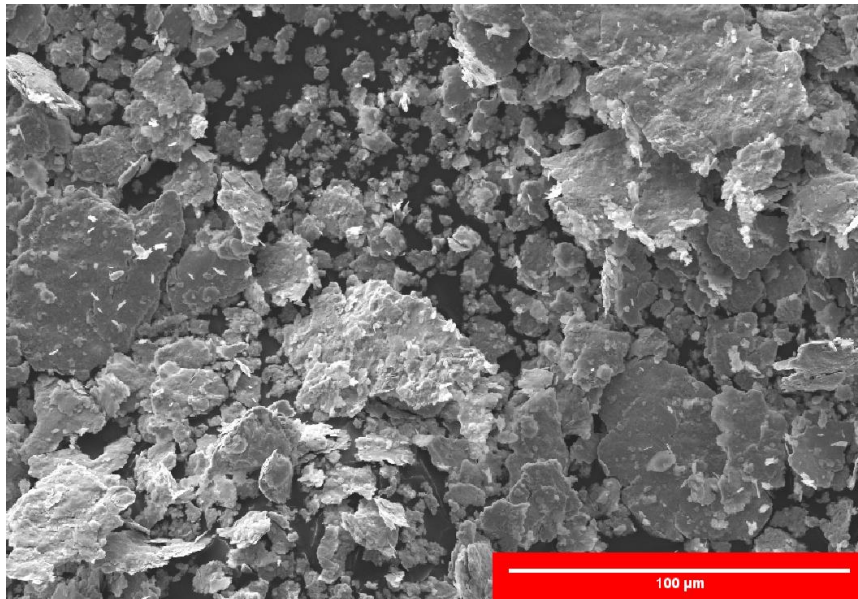
(b)



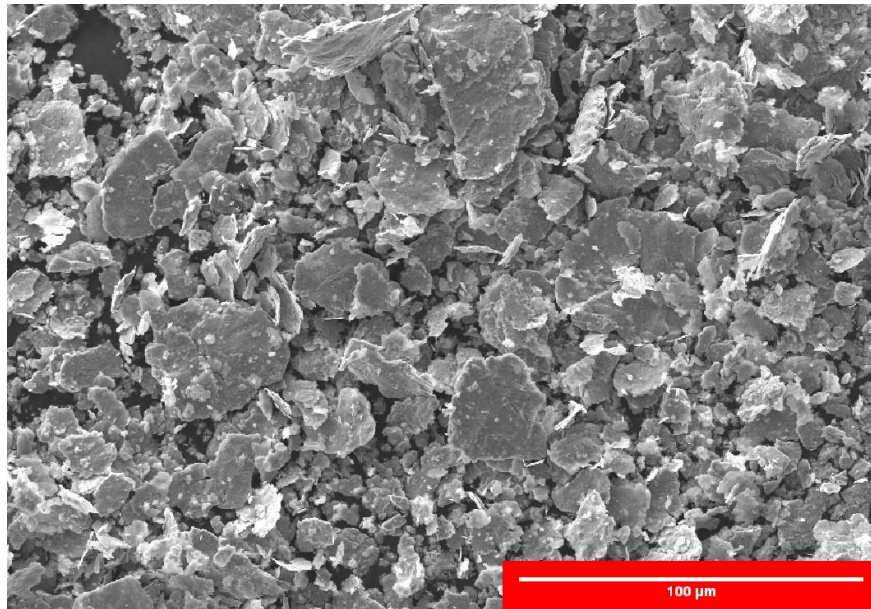
(c)

Figure 4.1: Scanning electron micrographs of alloy compositions (a) Ni (5wt.% Zn), (b) Ni (10wt.% Zn) along with (c) α -Al₂O₃ particles [103]

Further evidence that the Ni(Zn) alloy material was crushed and fractured simultaneously by the HEMA impact reducing them to micron sized particles. Particle flattening is evident as indicated by the flaky configuration seen in the SE micrograph of the pre-milled Ni(Zn) particle morphology in Figure 4.2. It is evident from the scale length in the SEM images for both Ni(5wt.% Zn) and Ni(10wt.% Zn) pre-milled for 2 hours, that the average size of Ni(5wt.%) particles is higher as compared to the Ni(10wt.% Zn) particles.



(a)



(b)

Figure 4.2: Particle morphology microstructure of both the (a) Ni(5wt.% Zn) and (b) Ni(10wt.% Zn) pre-milled for 2 hours.

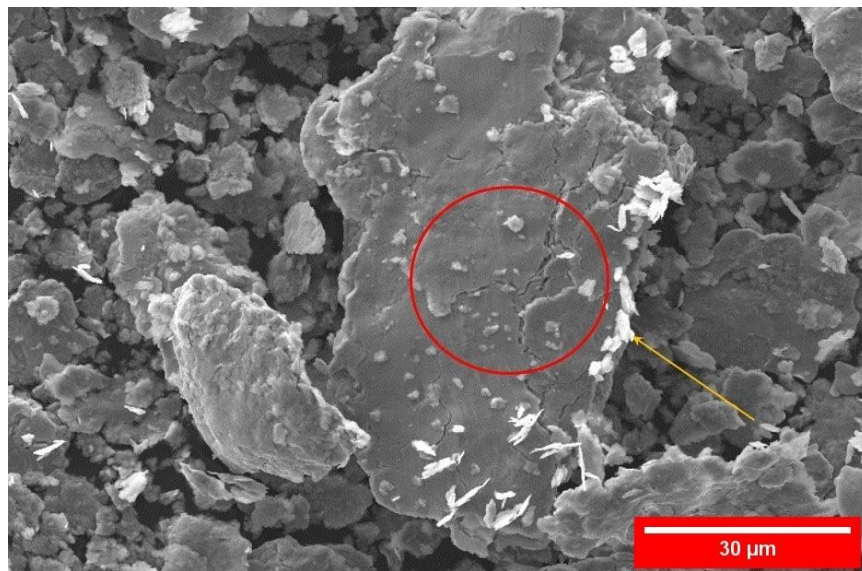
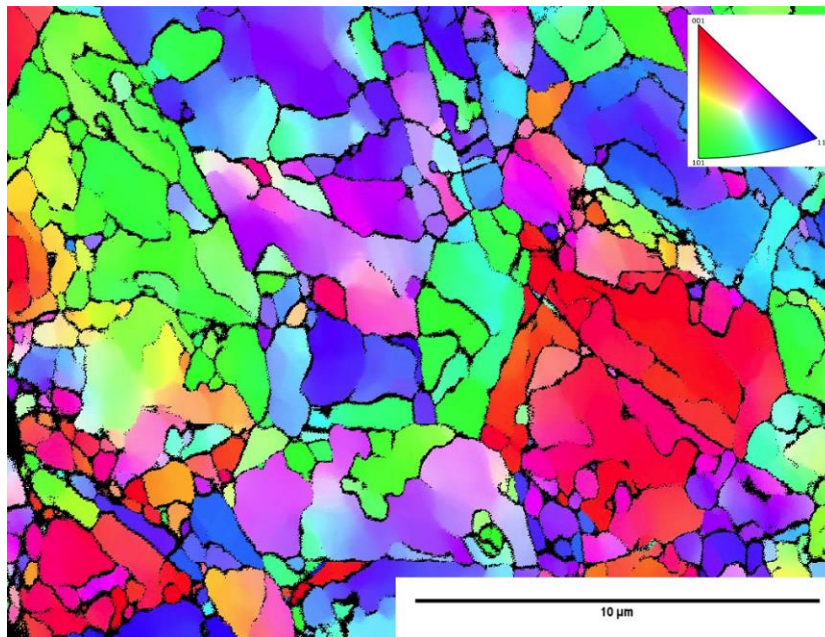


Figure 4.3: Scanning electron micrograph of Ni(5wt.%Zn) particles pre-milled for 2 hours [103].

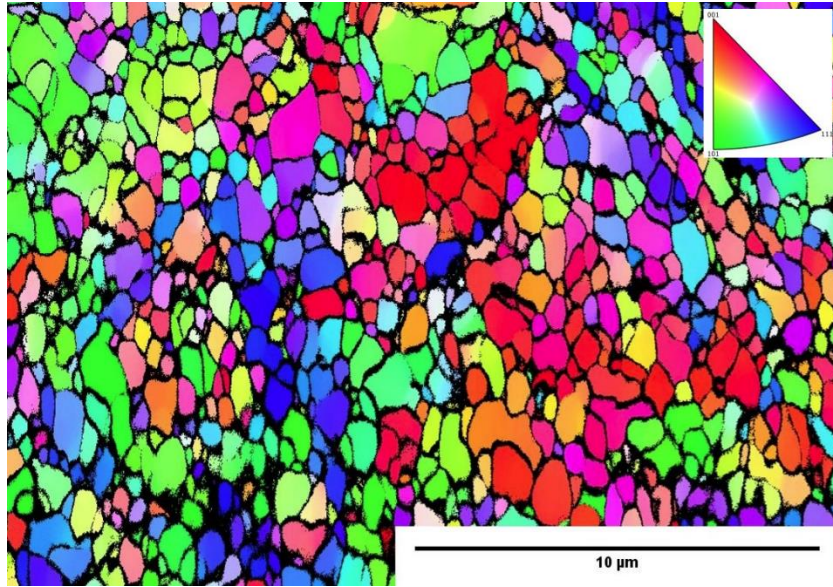
Figure 4.3 illustrates the several cracks across Ni(5wt.% Zn) pre-milled particle surface with a 'red' circular insert in it, which suggests that continuing fracture events are occurring throughout the pre-milling process. The scale in Figure 4.3 shows that the micron sized particles obtained after milling are suitable according to the size range of particles required for the CS deposition method [104].

4.2 EBSD characterization of Ni(Zn) alloy particles

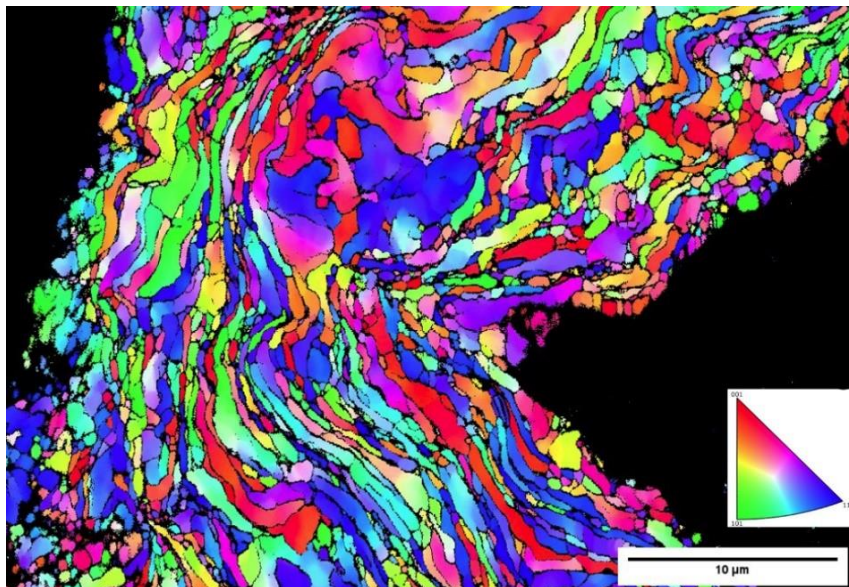
The EBSD inverse pole figures (IPF) maps showing the grain orientation pattern for as-received Ni(Zn) and pre-milled Ni(Zn) particles is shown in Figure 4.4. The scan results for both Ni(5wt.%Zn) and Ni(10wt%Zn) as received, vs. the pre-milled Ni(5wt.%Zn) and Ni(10wt.%Zn) are presented in Figures 4.4 (a), (c), and 16(b), (d), respectively.



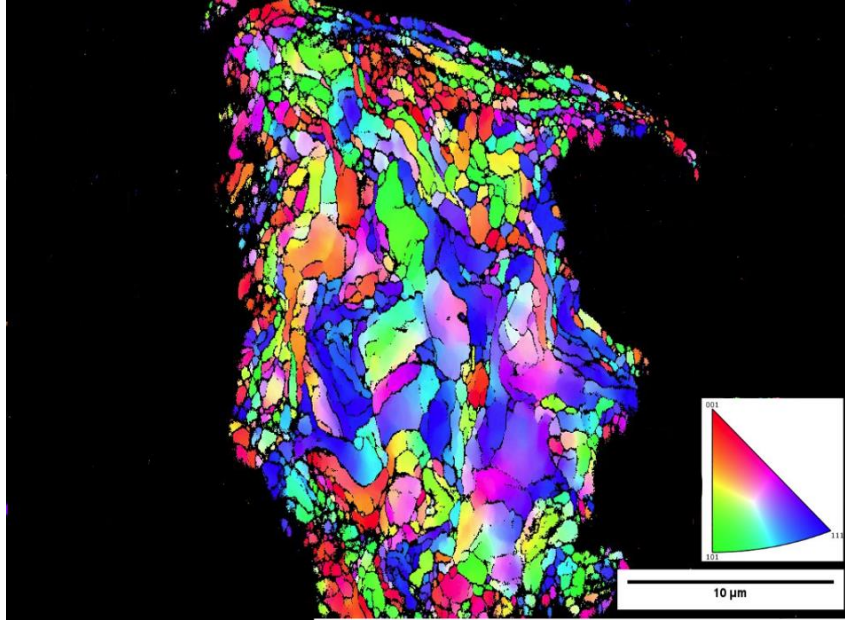
(a)



(b)



(c)



(d)

Figure 4.4: IPF maps for as-received alloy precursors (a) Ni(5wt% Zn), (b) Ni(10wt.% Zn) and pre-milled (c) Ni(5wt.% Zn), and (d) Ni(10wt.% Zn) particles for 2 hours [103].

Figures 4.4(a) and (b) make it clear that the as-received precursors of the Ni(5wt%Zn) and Ni(10wt.%Zn) alloys has stress free grains and less lattice defects. However, in Figure 4.4(c), the IPF map for Ni(5wt.%Zn) particles pre-milled for 2 hours shows significant deformation as predicted, as seen by the presence of elongated grains in the core and around the edges of the particle. Nevertheless, the presence of bigger grains at the center, which are less deformed than the ultrafine grains at the periphery, is evident in the IPF map of pre-milled Ni(10wt.%Zn) particles (Figure 4.4(d)). The decreased signal quality from the Ni(10wt.%Zn) particle boundary can be attributed to lattice defects that arise from deformation during the milling process for two hours. The IPF maps of the Ni(5wt.%Zn)

and Ni(10wt.%Zn) alloy particles unequivocally indicate that the former underwent successive deformations more uniformly than the latter. For as-received particles of Ni(5wt.% Zn) and Ni(10wt.% Zn) (Figures 4.5(a) and (b), respectively), and for pre-milled particles of Ni(5wt.% Zn) and Ni(10wt.% Zn) (Figures 4.5(c) and (d), respectively), the grain size distribution (GSD) in nanometers along with their respective normalized frequencies is shown in Figure 4.5. As indicated by Figure 4.5, the as-received particles have a smaller grain size distribution in the 100 and 1000 nm size range than the Ni(Zn) particles that were milled for two hours. Furthermore, pre-milled Ni(5wt.%Zn) alloy particles demonstrated a greater distribution of grain sizes between 100 and 1000 nm size range in comparison to Ni(10wt.% Zn) pre-milled powders. The former showed increased plastic deformation, followed by work hardening, and then eventual fracture of particles. This finding represents a significant turning point in the determination of further milling parameters for the synthesis of Ni(Zn)-alumina composite particles with varying compositions of ceramic in the composite and also the feedstock's cold spray-ability, which is made up of a substitutional alloy matrix under study [103].

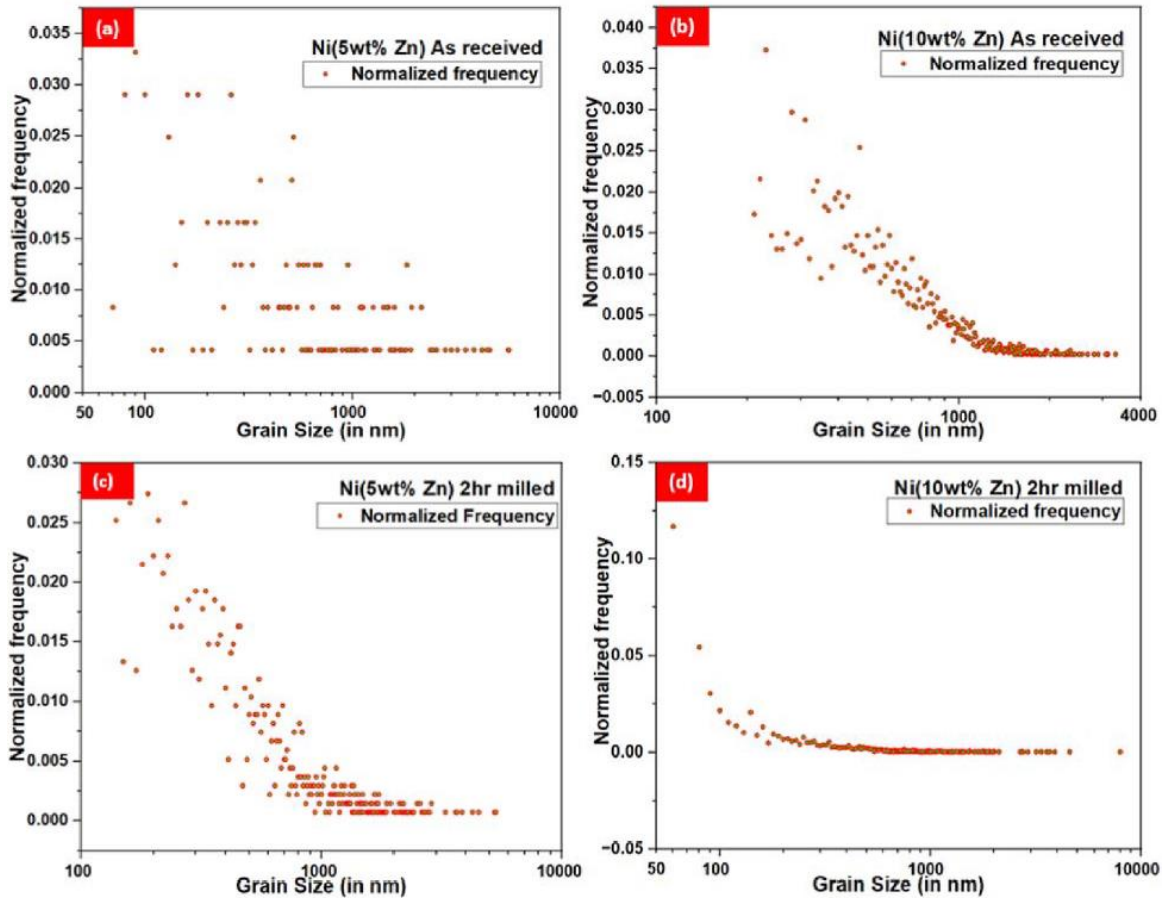
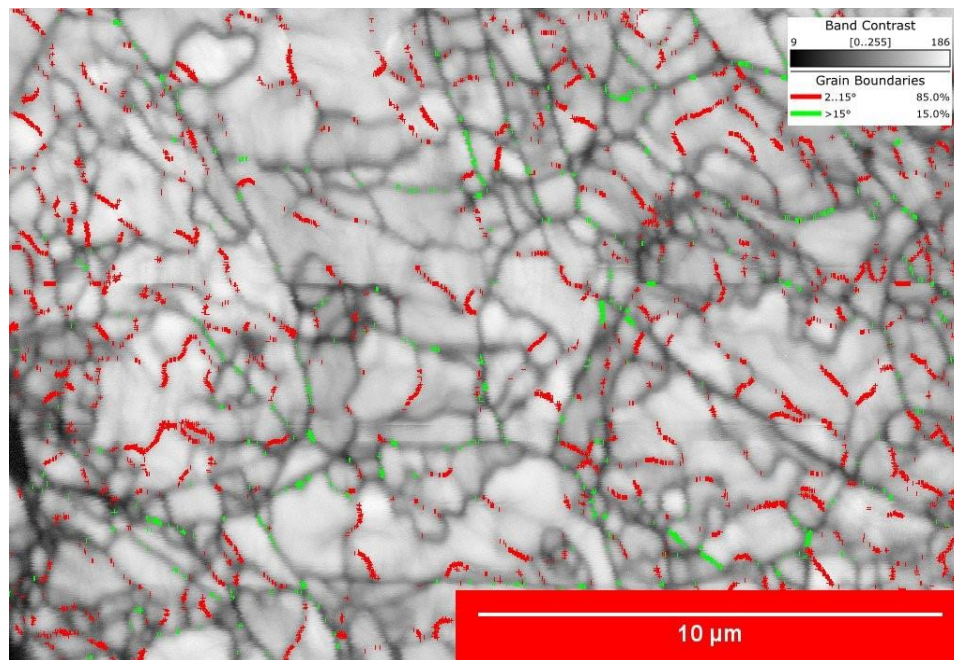


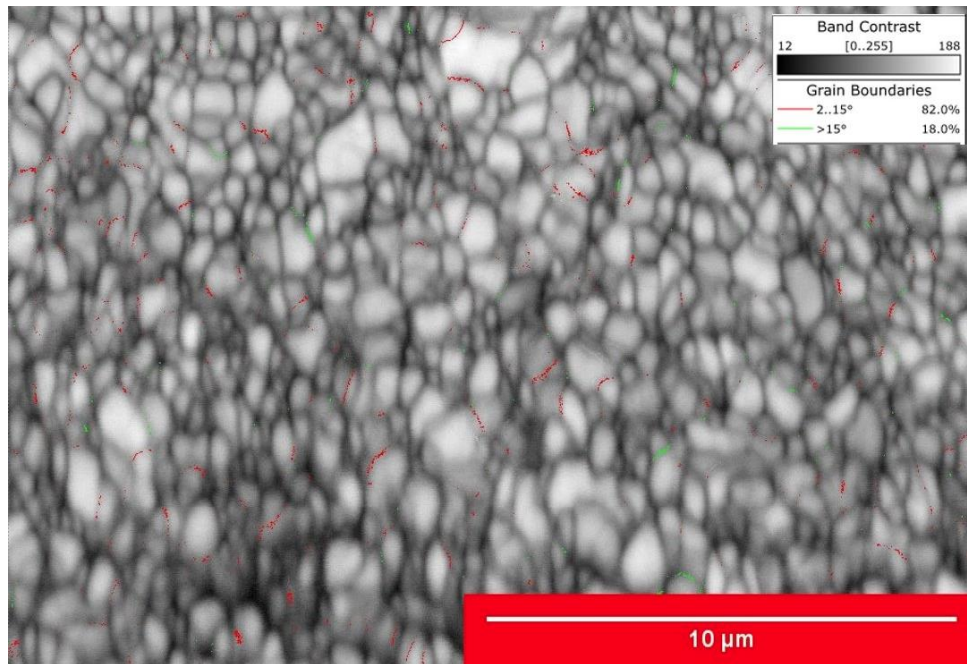
Figure 4.5 Grain size distribution for as-received alloy precursors (a) Ni(5wt.% Zn), (b) Ni(10 wt.% Zn) and pre-milled (c) Ni(5wt.% Zn), and (d) Ni(10 wt.% Zn) particles for 2 hours [103].

Figure 4.6 illustrates the band contrast image (BCI) consisting of the high-angle grain boundary (HAGB) and the low-angle grain boundary (LAGB) for the as received and pre-milled particles of both Ni(5wt.%Zn) and Ni(10wt.%Zn) alloy compositions. While HAGB is indicative of recently produced grain, LAGB can be described as an array of dislocations that shows lattice defects within the alloy material [105]. Figure 4.6 illustrates how pre-milling the Ni(5wt.%Zn) particles for two hours resulted in a decrease in the LAGB

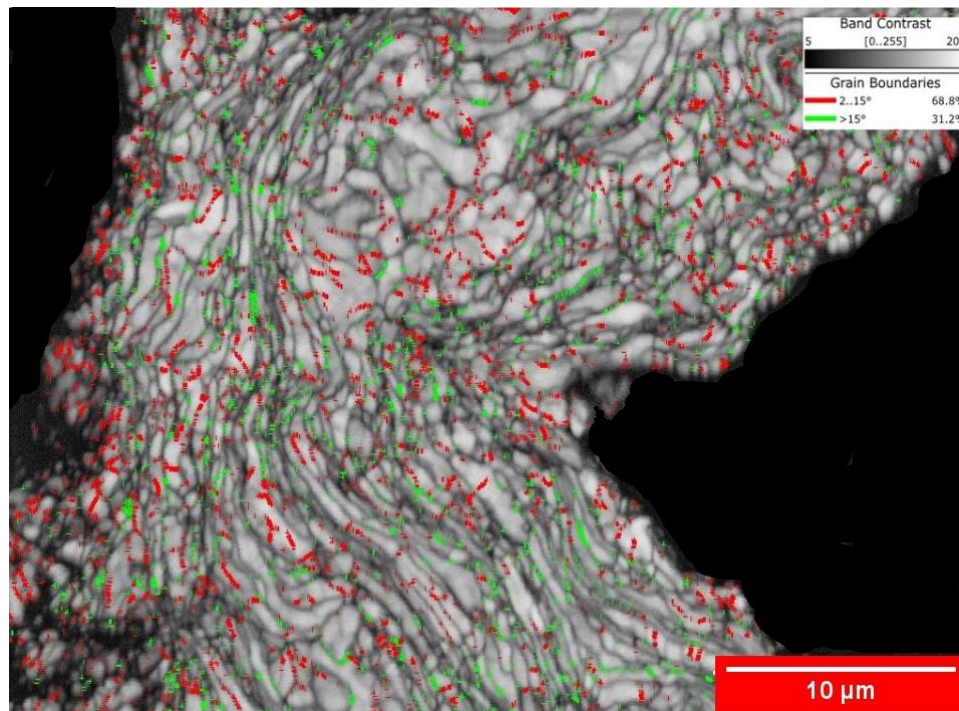
distribution from 85% to 68.8% and a surge in the HAGB distribution from 15% to 31.2%. Moreover, with Ni(10wt.% Zn), the HAGB distribution dropped from 18% to 14.7% while the LAGB distribution marginally rose from 82% to 85.3%. The pre-milled powders of Ni(5wt%Zn) alloy with higher HAGB levels demonstrated that these particles were more ductile and had experienced significant plastic deformation through the milling process. The boundaries may be called as LAGB once the dislocations are distinct and separate, however if the material is ductile and experiences intense, homogeneous deformation, the dislocation density keeps rising and ultimately results in overlapping of dislocation cores to form HAGB [103].



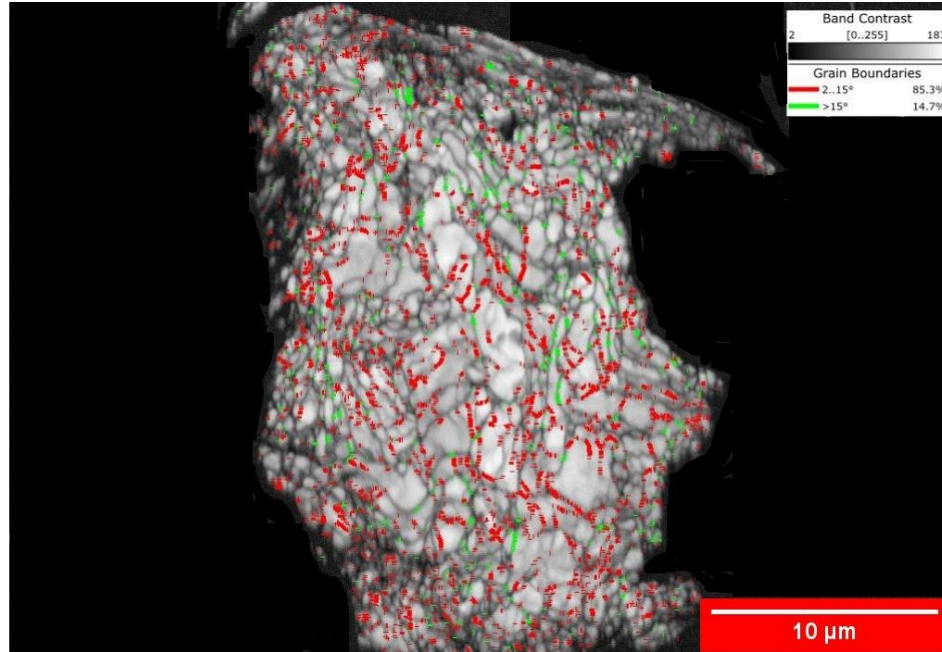
(a)



(b)



(c)



(d)

Figure 4.6: EBSD band contrast image for as-received alloy precursors (a) Ni(5wt.% Zn), (b) Ni(10wt.%Zn) and pre-milled (c) Ni(5wt.% Zn), and (d) Ni(10wt.% Zn) particles for 2 hours [103].

4.3 Particle size distribution analysis

The Ni(Zn) alloy precursors were pre-milled for 2 hours to obtain Ni(Zn) particles suitable for alumina ceramic embedment, to make Ni(Zn)-alumina composite particles with suitable micron size range for cold spray applications. Figure 4.7 illustrates the particle size distribution (PSD) and the cumulative volume fraction for both pre-milled Ni(5wt.%Zn) and Ni(10wt.%Zn) alloy compositions along with as-received α -Al₂O₃.

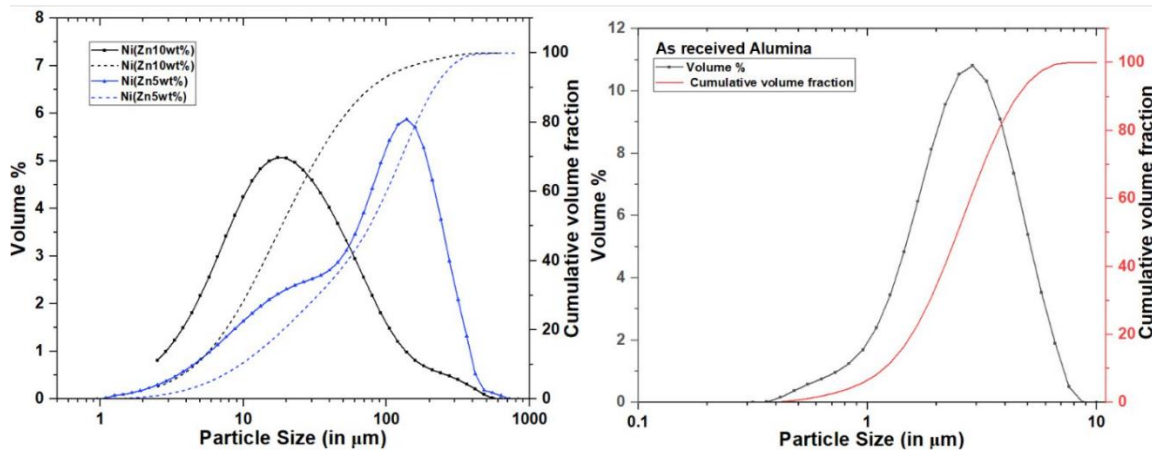


Figure 4.7: PSD in relation to cumulative volume fraction for (a) Ni(5wt.%Zn) and Ni(10wt.% Zn) alloy particles pre-milled for 2 hours, (b) as received $\alpha\text{-Al}_2\text{O}_3$ particles [103].

As seen from the PSD graph for both Ni(5wt.% Zn) and Ni(10wt.% Zn), it is evident that the PSD for Ni(5wt.% Zn) alloy particles is wider as compared to Ni(10wt.% Zn). Even after 2 hours of milling, the majority of particles of Ni(5wt.% Zn) alloy are bigger than 100 μm . This could be due to the higher ductility for Ni(5wt.% Zn) alloy as compared to Ni(10wt.% Zn). There is a delay in fracture of these particles. The PSD of Ni(Zn) alloy particles agrees with the SEM microstructures for pre-milled particles for both the alloys and the corresponding EBSD results obtained [103].

The PSD of the pre-milled Ni(Zn) alloy particles is significantly higher than that of the as-received $\alpha\text{-Al}_2\text{O}_3$ particles, by at least one order of magnitude. In comparison to the greater size of Ni(Zn) alloy particles pre-milled for two hours, the PSD of $\alpha\text{-Al}_2\text{O}_3$ is less than 10 μm . The incorporation of $\alpha\text{-Al}_2\text{O}_3$ grains within the Ni(Zn) alloy matrix is facilitated by the dissimilarity in particle sizes between the reinforcement and matrix [103].

Figure 4.8 illustrates the transformation of PSD in the milled specimens. Every specimen (S1–S12) had a Gaussian distribution, and Table 4.1 shows the associated mean and median values as well as a PSD analysis.

Table 4.1: The associated mean and median values as well as a PSD analysis for specimens (S1-S12) [103].

Specimen ID	Average particle Size D[4,3] (µm)	d_{0.1} (µm)	d_{0.5} (µm)	d_{0.9} (µm)	Span d _{0.9} –d _{0.1} d _{0.5} <i>d</i> _{0.9} – <i>d</i> _{0.1} <i>d</i> _{0.5}
S1	52.788	4.968	41.323	106.981	2.468674
S2	64.925	22.061	55.987	114.043	1.642917
S3	50.162	2.182	32.317	128.263	3.901383
S4	79.069	5.122	60.271	179.192	2.888122
S5	74.021	28.36	66.613	132.373	1.561452
S6	68.186	34.748	62.499	110.184	1.206995
S7	73.794	32.269	67.701	126.119	1.386
S8	76.098	27.555	68.582	137.342	1.601
S9	46.685	2.269	33.527	108.934	3.181
S10	82.148	33.813	75.187	142.765	1.449
S11	75.528	27.369	65.51	135.608	1.652
S12	79.684	7.911	72.364	157.707	2.07

The Ni(5wt.% Zn)–alumina composite particles of 70:30 proportion (S1, S2, S3), where sample S1 (milled for 1 hour) exhibit significant PSD, as shown by the PSD graph in Figure 4.8(a). This could be because of the beginning of particle flattening as well as cold welding. But in contrast to S2, the PSD is shorter than S1, which is explained by the concurrent cold welding that causes more plastic deformation and the beginning of particle fracture. The fracturing process brought on by extensive plastic deformation and the existence of ceramic grains eventually overruled the cold welding of powder particles in S3 (milled for 4 hours), resulting in a finer PSD and the creation of equiaxed particles. A high PSD range is seen in S4 (milled for 1 hour) in Figure 4.8(b), which corresponds to Ni(5wt.% Zn)–alumina with 50:50 ratio (S4, S5, S6). This is due to particle flattening and the beginning of cold welding, which renders the particles unsuitable for CS. On the other hand, in S5 (milled for 2 hours), the PSD reduces down along with reduction in particle size, probably as a result of the beginning of fracture. Also, the PSD reduced even more in S6 (milled for 4 hours) due to increased work hardening and a greater quantity of ceramic component present, which caused greater particle fracturing. The PSD of Ni(10wt.% Zn)–alumina composite particles in 70:30 proportion (S7, S8, S9) is represented in Figure 4.8(c). While specimen S8 (milled for two hours) displays a larger and wider PSD, specimen S7 (milled for one hour) displays a less wide PSD. As seen by the EBSD IPF map (see Figures 4.4(c) and (d)), this may be the outcome of less plastic deformation and comparatively faster fracture due to inferior ductility in the Ni(10wt.% Zn) alloy particles in comparison to that of the Ni(5wt.% Zn) alloy particles. Nevertheless, in S9 specimen (milled for 4 hours), reduced PSD was produced via fracturing of particles rather than cold welding. Ni(10wt.% Zn)–alumina composite particles with a 50:50 proportion are represented in Figure 4.8(d)

(S10, S11, S12). Compared to specimen S11 (milled for two hours), S10 specimen (milled for one hour) has a narrow PSD and span. Additionally, PSD of specimen S10 is higher than that of S11, which may be the result of both the increased ceramic content and the Ni(10wt.% Zn) alloy's reduced ductility. Specimen S12 witnesses a minor increase in particle size, which could be the result of rewelding and particle agglomeration, which could then lead the powder particles to fracture due to work hardening [103].

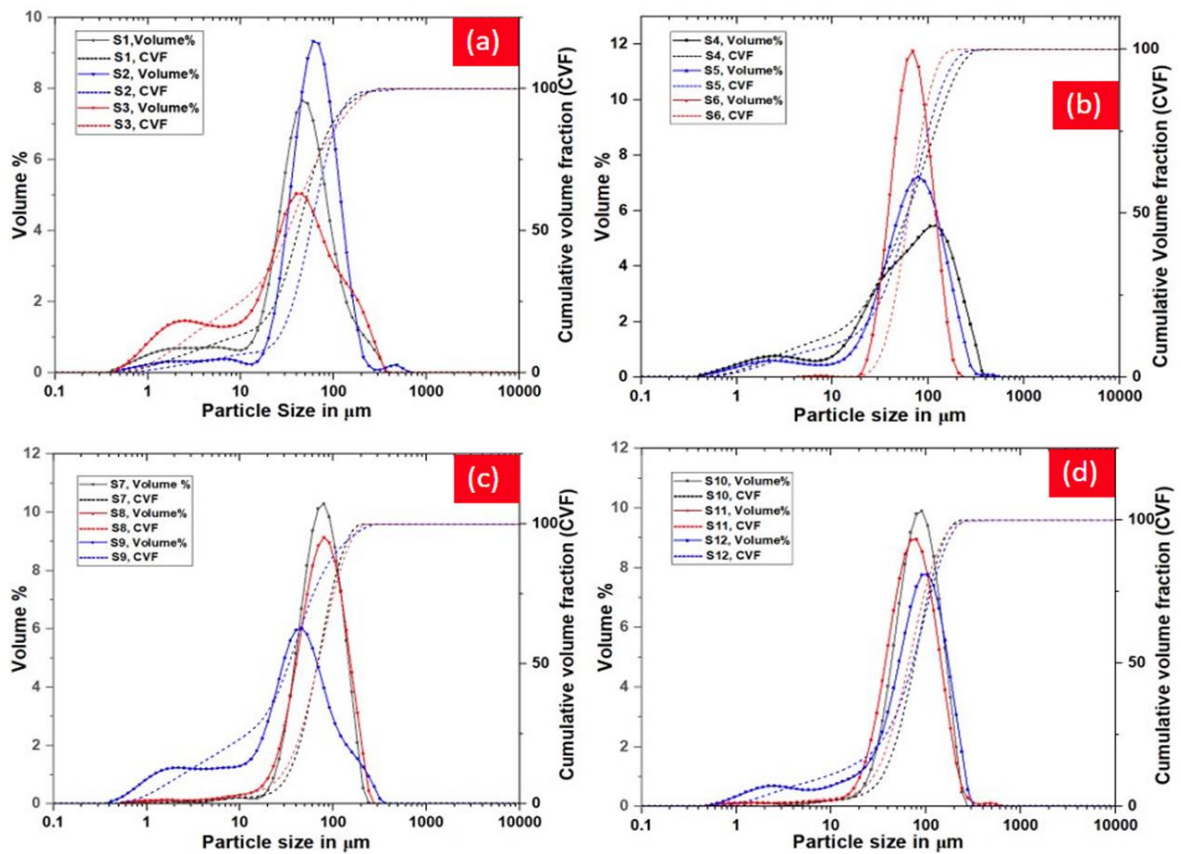


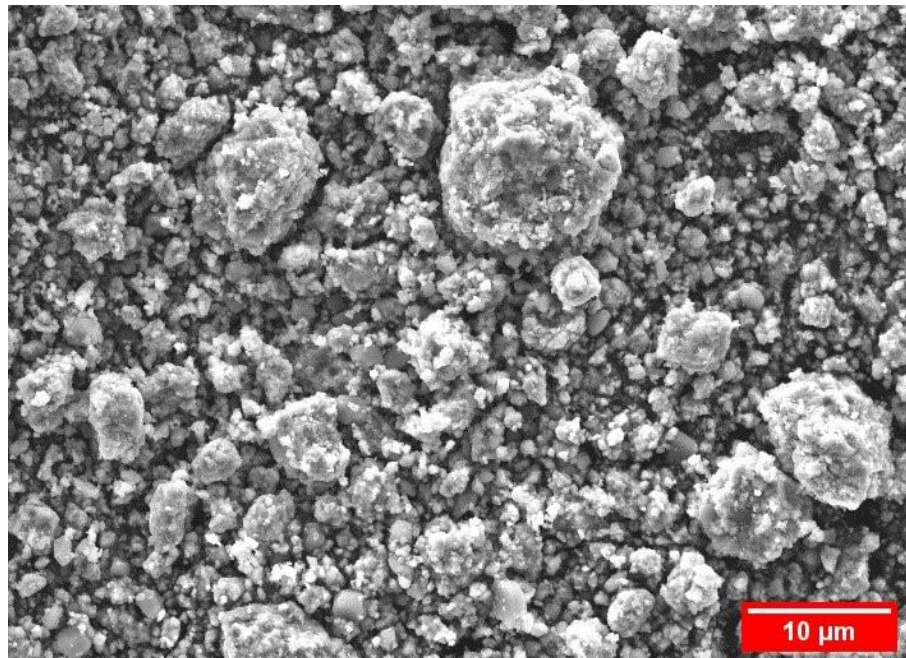
Figure 4.8: illustrates the transformation of PSD in the milled specimens (S1-S12) [103].

To get dense, non-porous CS deposits that have high interfacial and inter-particle cohesive strength, it is important to consider the average size of particles and PSD of the particle feedstock. In the case of metals, Matteazzi et al. [106] suggested a universal particle size in the range of 5–200 μm , whereas Assadi et al. [107] proposed an optimal size range between 5 and 105 μm . Marocco [108] et al. conducted combined experimental and numerical investigations and found that for Ti particles, porosity decreased with increase in particle size in the 28–47 μm range. According to recent research [109], larger particles in a PSD ranging from 10 to 50 μm bond more strongly than smaller ones because of their capacity to undergo considerably higher adiabatic heating upon collision. Nevertheless, Raelison et al. [92] noted that it is challenging to accelerate particles larger than 100 μm in the CS nozzle. This is caused by the restricted amount of time particles spend inside nozzle combined with the longer periods needed for thermal energy and momentum to be transferred from gas to particles of larger size. With this information in hand, the optimal powder particle size distribution was determined to be between 10 and 100 μm .

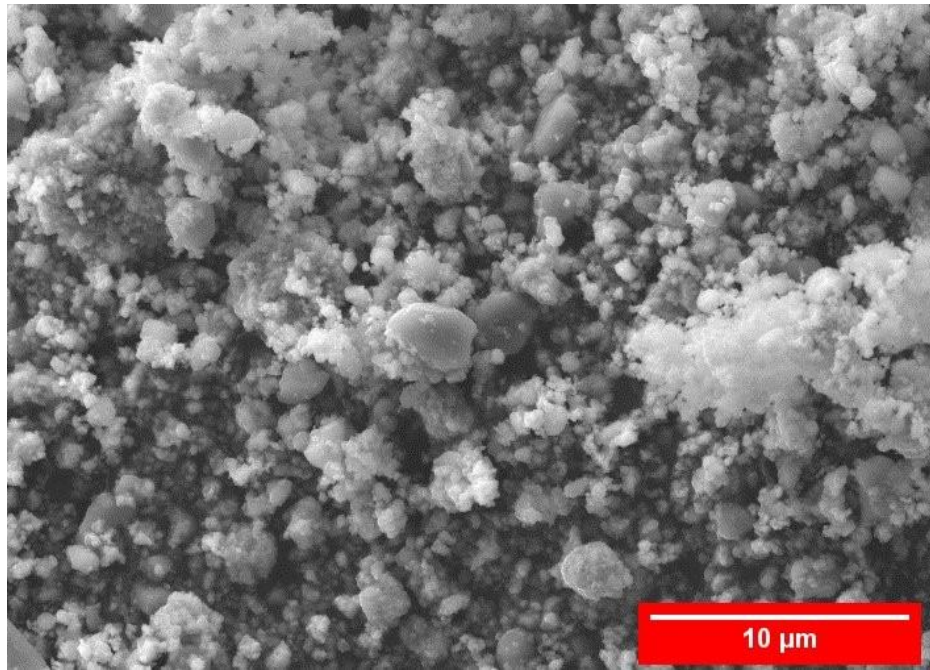
4.4 Microstructural characterization of Ni(Zn)-alumina composite particles

The Ni(Zn) alloy particles are initially turned flat by the impact of steel balls during HEMA process, which broadens the range of particle sizes [110]. As flattened particles are welded together to create big agglomerates, cold welding process of metal particles starts to occur [111]. Due to the greater number of potential sites for embedding ceramic grains into the metal matrix, the alumina ceramic reinforcement may be incorporated into the particles of the Ni(Zn) alloy [112]. These reinforcement grains function as a brittle phase during the milling process, facilitating the fracture of composite particles to produce an equiaxed

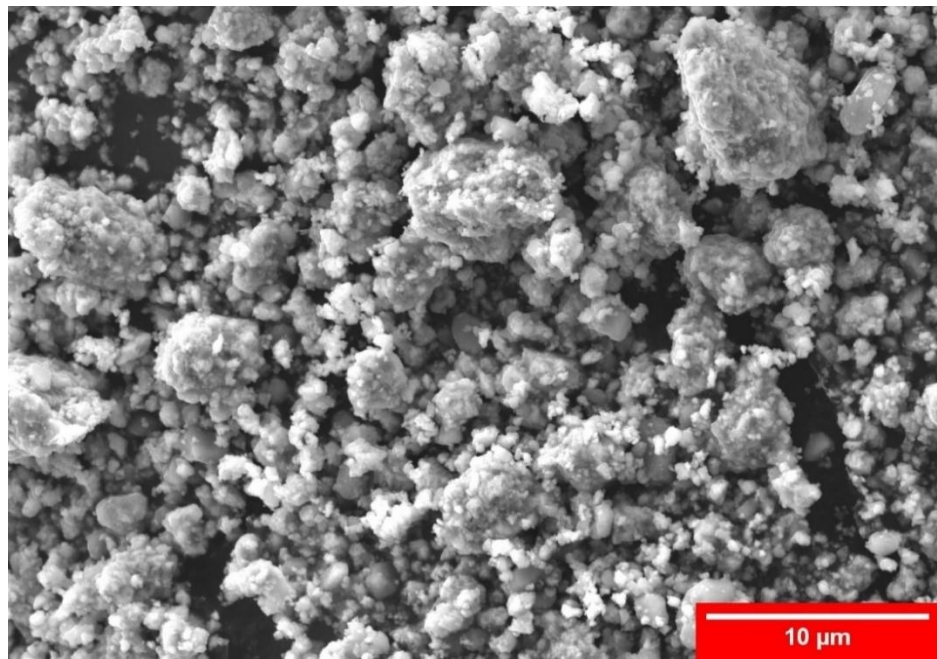
structure. Dislocations are created by the impact of the steel balls, which causes plastic deformation in the metallic matrix phase. This finally results in strain hardening as well as grain refining. Strain hardening and grain refinement occurs locally in Ni(Zn) particles as a result of reinforced ceramic grains that obstruct dislocations and increase dislocation density. Composite particles shatter more quickly and more readily to produce an equiaxed shape as a result of local work hardening of the particles, which also decreases the fracture toughness [111].



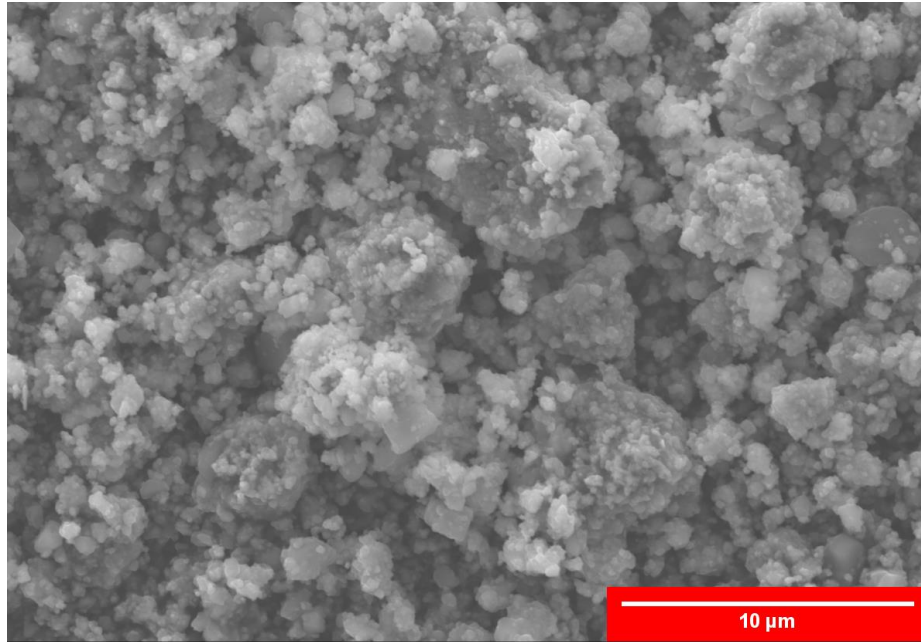
(a)



(b)



(c)



(d)

Figure 4.9: shows the SEM images of post-milled samples following a 4-hour milling period. Batches #1, #2, #3, and #4 are represented by Figures 4.9(a)- 4.9(d), respectively [103].

Figure 4.9 shows the SEM images of post-milled samples following a 4-hour milling period. Batches #1, #2, #3, and #4 are represented by Figures 4.9(a)–4.9(d), respectively. The Ni(Zn) region (atomic mass: 58.3(58.7)) can be seen as darker regions, while alumina (atomic mass: 102) is represented by the bright region. In contrast to Figures 4.9(a) and (c). Because there is a greater alumina content (50 wt.%) in S6 and S12, Figures 4.9(b) and (d) exhibit a more consistent particle size evolution and more agglomeration between the alumina grains and the alloy matrix. The alumina phase is trapped at the welded matrix joints and becomes embedded inside the alloy matrix as a result of repeated flattening,

cold-welding, and fracturing of particles under the impact [113]. Nevertheless, the alumina reinforcements start to agglomerate the alloy matrix when additional alumina grains become available. Figure 4.10 shows the matrix flattening, dispersion of reinforcement, along with agglomeration during milling process [114].

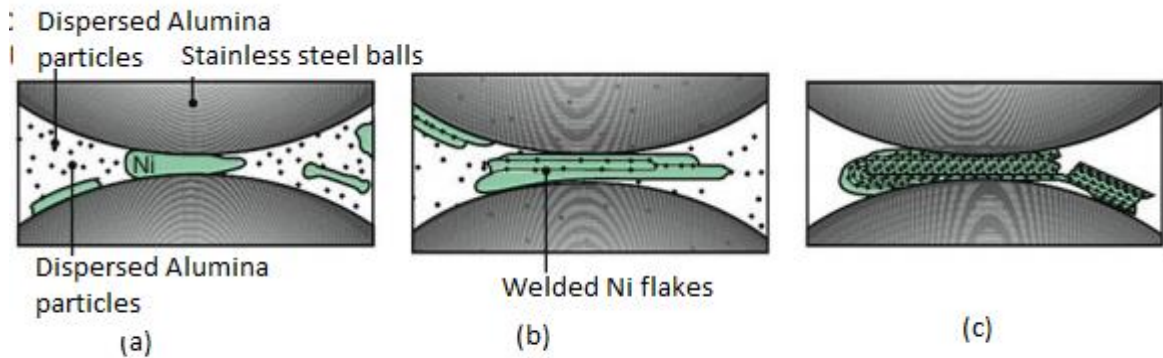
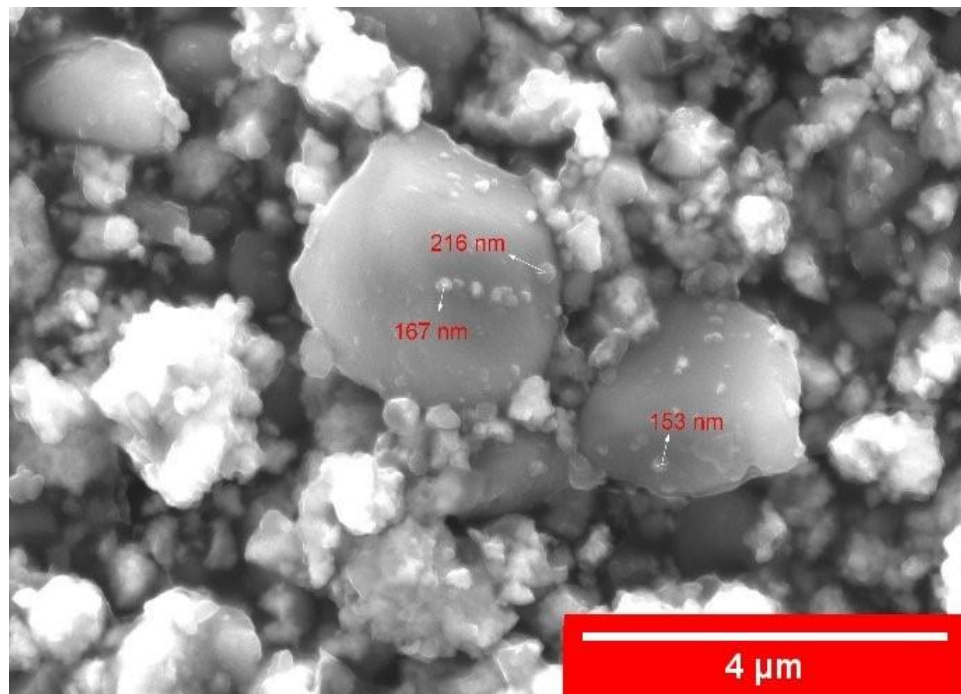


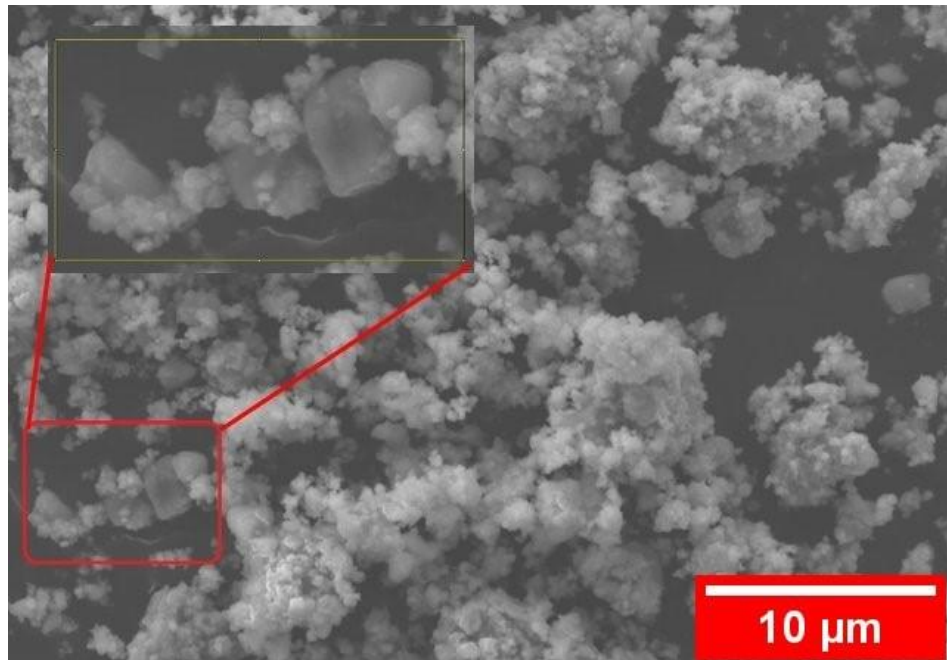
Figure 4.10: HE-MA mechanisms of Ni particles incorporating alumina reinforcements: (a) particle flattening, (b) alumina embedment, and (c) alumina agglomeration [114].

It is clear from above that the DoE that for both alloy compositions, high alumina content caused the matrix phase to agglomerate. However, it is still needed to prove that there is embedment of reinforcement in the alloy matrix. As a result, as seen in Figure 4.11, SEM examination was done first using non-agglomerated particles in specimen S3. It was determined that the alloy matrix in specimen S3 contained embedded quasi-circular alumina grains having diameters within the range of a few hundred nanometers. Furthermore, an interesting characteristic of smaller matrix particle fusion supported by reinforcement in specimen S6 from Figure 4.11 (the "red" insert). It is determined that the

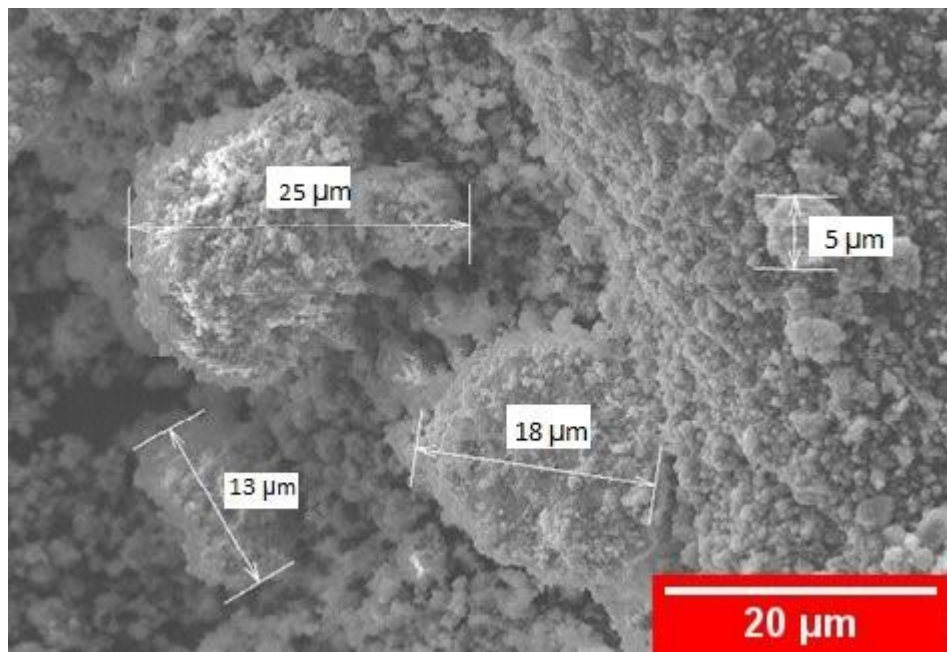
matrix fusion was the beginning of a layered structure construction involving alumina nanograins and Ni(Zn) particles, and eventually developing to a bi-layer composite made of Ni(Zn) and alumina. The determined particle size of S3 specimen within a range appropriate for cold spraying is also visible in Figure 4.11 [103].



(a)



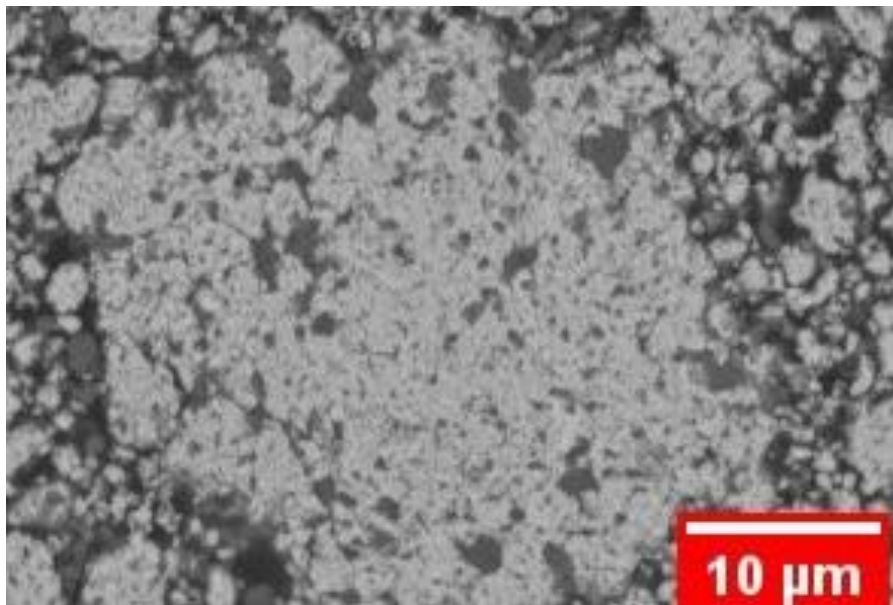
(b)



(c)

Figure 4.11: Characteristics seen in the SEM image include: a) embedding in S3, b) matrix fusion in S6 (with an insert depicting the enlarged view of fusion), and c) particle size assessment in S3 [103].

An EDS elemental profile study of S3 composite particle throughout its cross-section was performed to confirm the embedding of alumina grains inside Ni(Zn) alloy matrix. In Figure 4.12(a), the reference microstructure is presented. The EDS elemental distribution maps of each component element in the S3 specimen particle microstructure correspond to Figure 4.12(b). In comparison to other elements in the matrix, the Ni and Zn distribution is comparatively dense, as seen in Figure 4.12(b). Subfigure iv) in Figure 4.12(b) shows an overall distribution of nickel element in alloy matrix, while sub-figures ii) and iii) show a significant uniform dispersion of alumina reinforcement inside Ni(Zn) alloy matrix. Zinc is likewise shown equally dispersed in alloy matrix in sub-figure v) of Figure 4.12(b), as both alloy compositions utilized represent substitutional alloys [103].



(a)

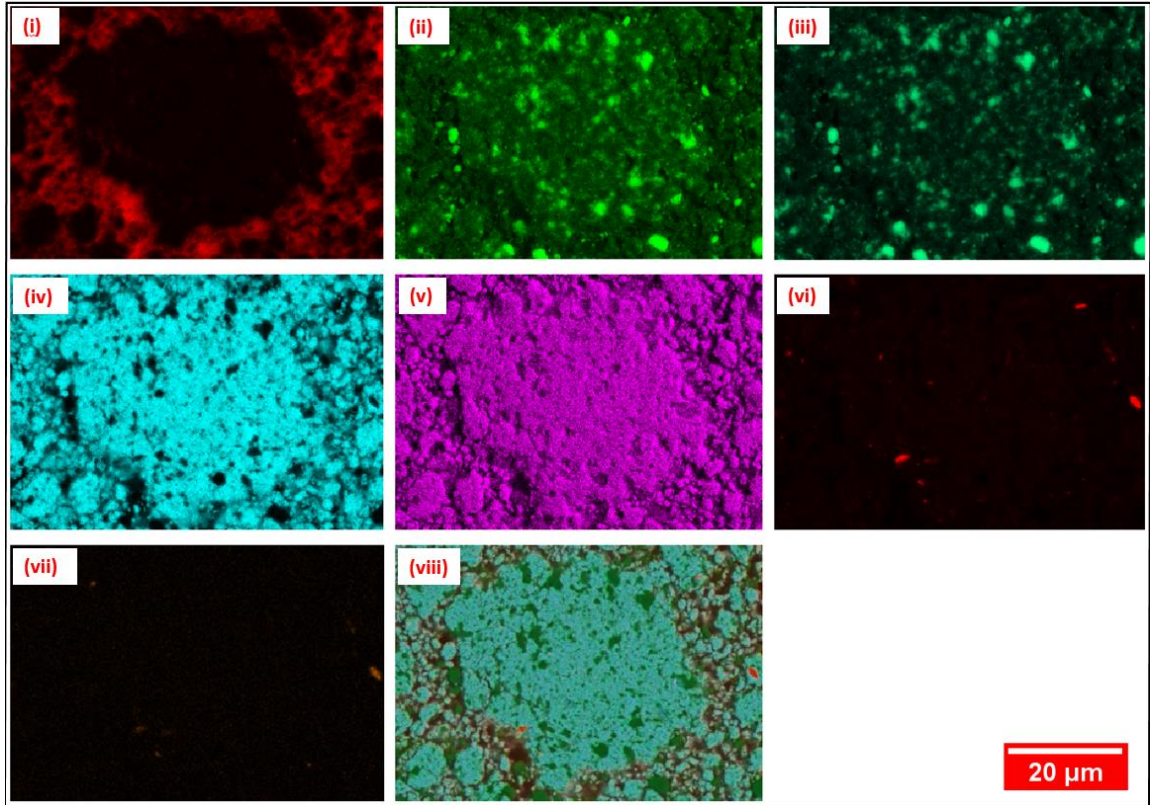


Figure 4.12: Specifications of the S3 composite specimen: (a) SE microstructure; (b) elemental distribution maps, arranged as follows: (i) mounting carbon, (ii) oxygen, (iii) aluminum; (iv) nickel, (v) zinc, (vi) iron; (vii) chromium, and (viii) phase-map [103].

Table 4.2 lists the elemental weight % determined by EDS elemental map analysis for the S3 specimen. Fe and Cr were detected, which suggested that the steel balls and milling vial used in the ball milling process may have contaminated the sample [103].

Table 4.2: List of elements shown in the EDS analysis of S3 specimen [103].

Elements	Ni	Zn	Al	O	Fe	Cr
Wt.%	67.3	4.0	14.4	12.2	1.9	0.2

4.5 X-ray diffraction analysis

The XRD patterns of the desirable particle specimens S3, S6, S9, and S12 are shown in Figure 4.13, based on the observations that were obtained in the previous subsections.

The prominence of the α -Al₂O₃ phase peaks can be attributed to the larger fraction of this ceramic phase present in S6 and S12. After the powder particles were milled for four hours, the peak broadening shows the gradual amorphization and plastic deformation of the particles. Grain refinement and strain hardening are produced during mechanical milling by plastic deformation. The material's ductility affects the formation of grain boundaries and dislocations. During mechanical milling, to attain a stable state between cold welding and particle fracture, a longer milling period is needed for more ductile materials. Brittle ceramic grains added to the ductile metal/alloy matrix accelerate the fracturing process by reducing fracture toughness. Considering both alloy compositions, Ni(5wt.% Zn) and Ni(10wt.% Zn), Table 4 illustrates the crystallite size for as-received pellets and crystallite size in alloy matrix in the composite particles for all specimen milled for 4 hours (S3,S6,S9 and, S12) as determined by the Williamson-Hall (W-H) method in OriginLab® software [103].

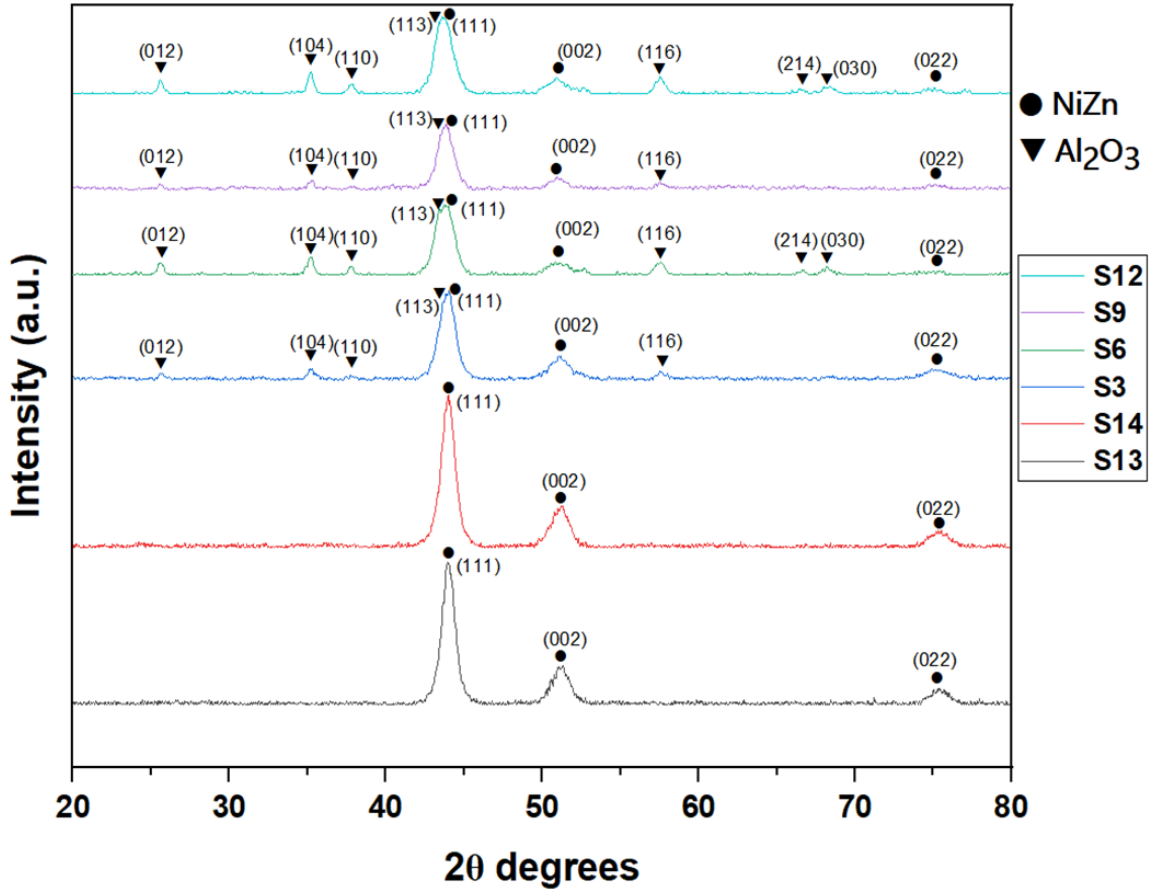


Figure 4.13: XRD pattern for particle specimens S3, S6, S9, S12, S13, and S14 [103].

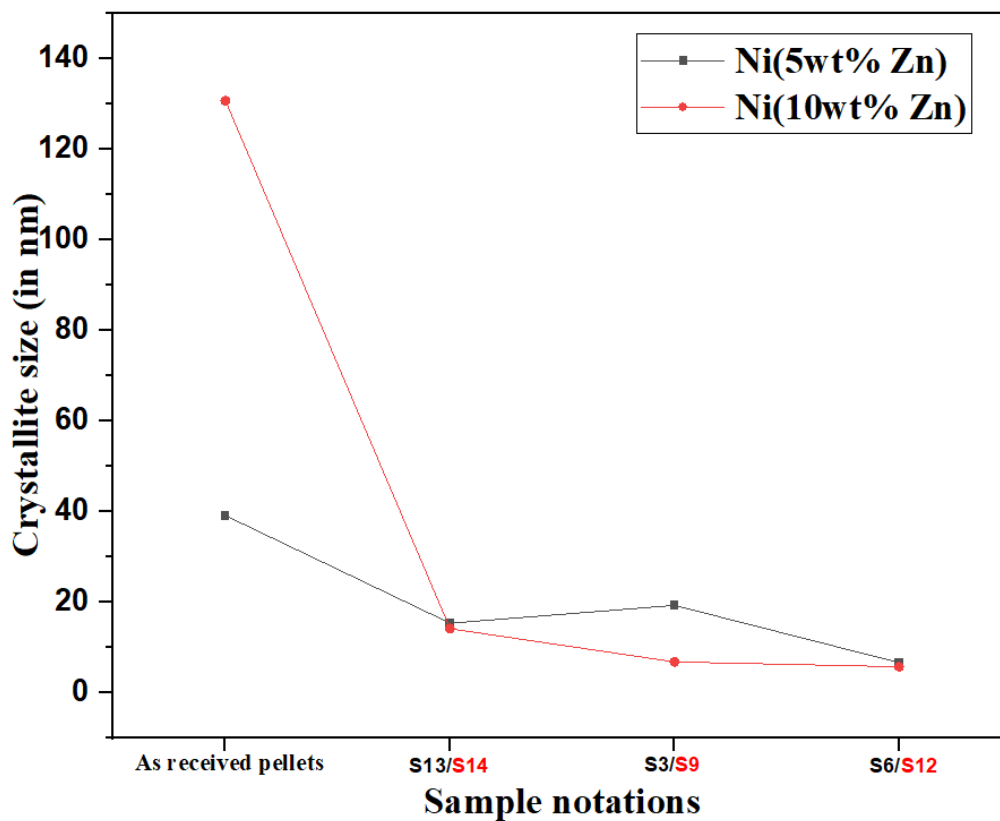
It is apparent that the crystallite size shrank after 4 hours of milling. More specifically, the crystallite size decreased even more as the ceramic concentration in the composite particles increased. This could be because the alumina grains blocked the dislocations, increasing the local work hardening and decreasing the fracture toughness. It is interesting to note that alumina grain crystalline sizes for S3 and S6 are smaller than in S9 and S12. This is explained by the fact that the ductility of the individual alloy matrix phases varied, with Ni(5wt.% Zn) having a greater amount of ductility than Ni(10wt.% Zn). Since the less-ductile Ni(10wt.% Zn) alloy phase fractured more quickly than Ni(5wt.% Zn), the energy consumption is mainly focused to fracture the Ni(10wt.% Zn) phase than the brittle alumina

particle grains. A harder alloy like Ni(Zn) could not be able to prevent the alumina particles from breaking, which reduced the crystallite size of the alumina ceramic grains during mechanical milling. On the other hand, it has been reported that the amorphization of graphene nanoplatelets (GNP) was delayed during ball milling by the ductile metal aluminum in the aluminum metal-matrix composites, protecting GNP as a reinforcement in the metal matrix [115]. The values in Table 4.3 are represented graphically in Figure 4.14.

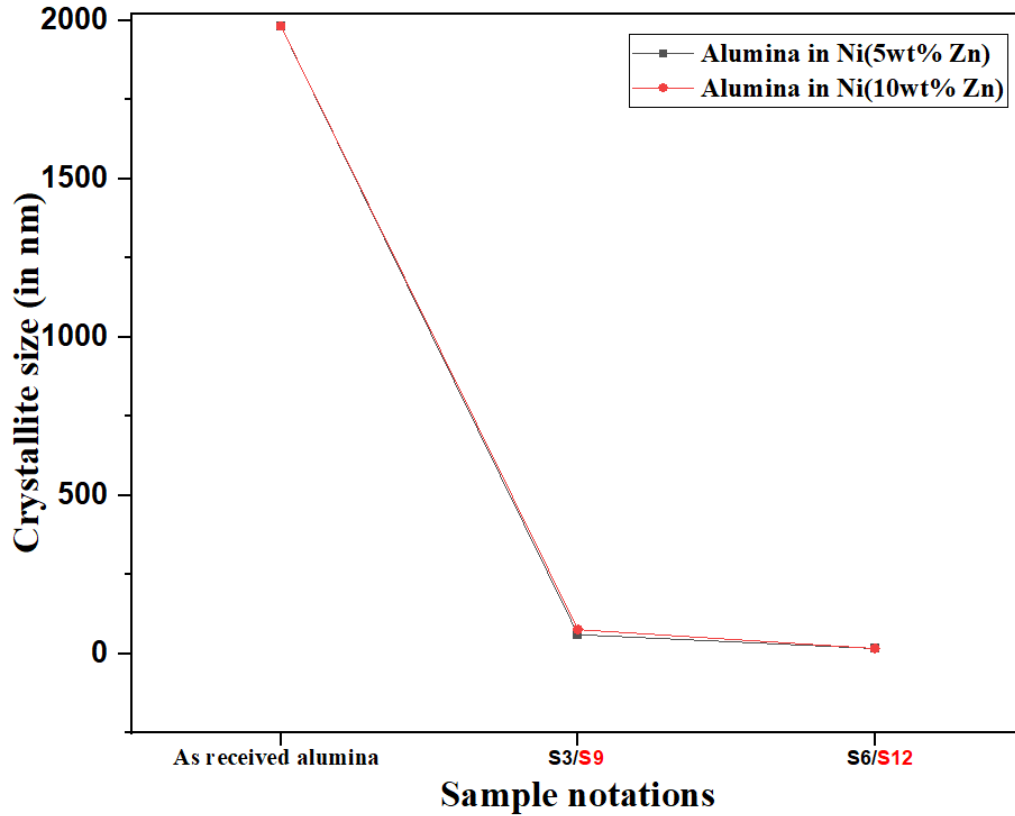
Table 4.3: Crystallite size was determined for (a) matrix and (b) ceramic reinforcement using the W-H method [103].

(a)	
Sample notation	Crystallite Size (nm)
Ni(5wt.% Zn)	
As-received	39.11797
S13	15.36088
S3	19.31325
S6	6.59505
Ni(10wt.% Zn)	
As-received	130.73747
S14	14.1482
S9	6.79989
S12	5.71313
(b)	

As-received Al ₂ O ₃	1983.45
Al ₂ O ₃ in S3	59.48178
Al ₂ O ₃ in S6	15.67602
Al ₂ O ₃ in S9	75.62642
Al ₂ O ₃ in S12	15.76267



(a)



(b)

Figure 4.14: The graph depicts crystallite size of the following samples: (a) Ni(Zn) as-received particles and S13, and S14 specimens; (b) as-received alumina and alumina reinforcement in S3, S6, S9, and S12 specimens [103].

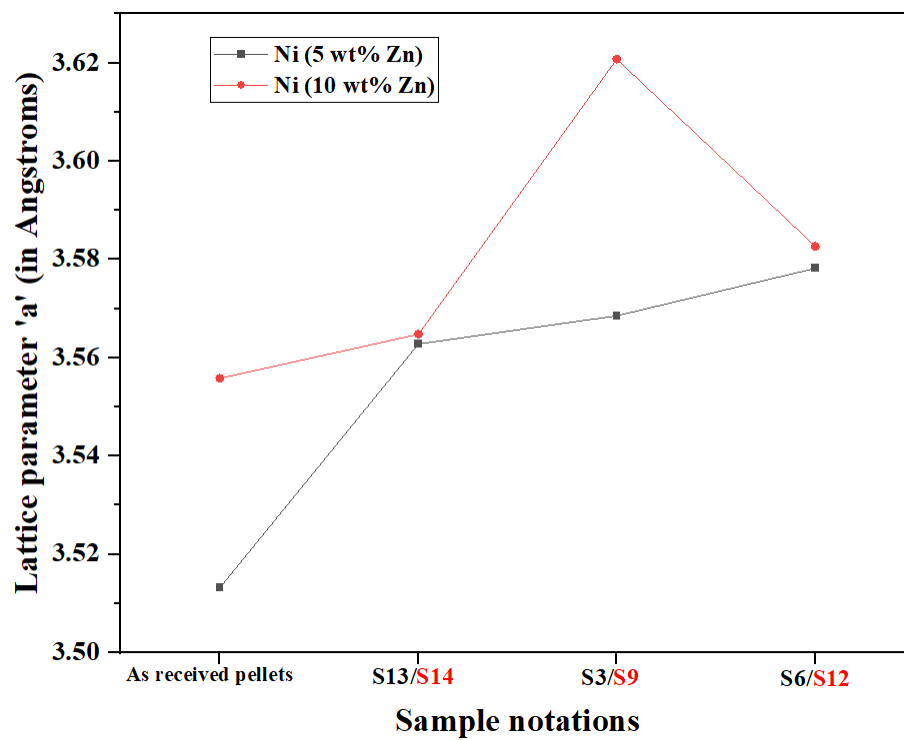
The influence of HE-MA upon the lattice parameters of Ni(Zn) composite particles is shown in Table 5. It is apparent that there is rise in distortion of Ni(Zn) lattice with an increase in alumina content. It is observed that the milled alloy particles as well as composite particles exhibit high Ni(Zn) lattice parameters. Nevertheless, the c/a ratio of the Al_2O_3 hexagonal lattice decreased as the milling time increased for alumina grains in the composite particles. It is interesting to note that the S3 and S6 specimens exhibit a greater drop in the c/a ratio than do the S9 and S12 specimens. This could be due to

variation in ductility of the composition of the Ni(Zn) alloys that were utilized. The data in Table 5 is presented graphically in Figure 4.15 [103].

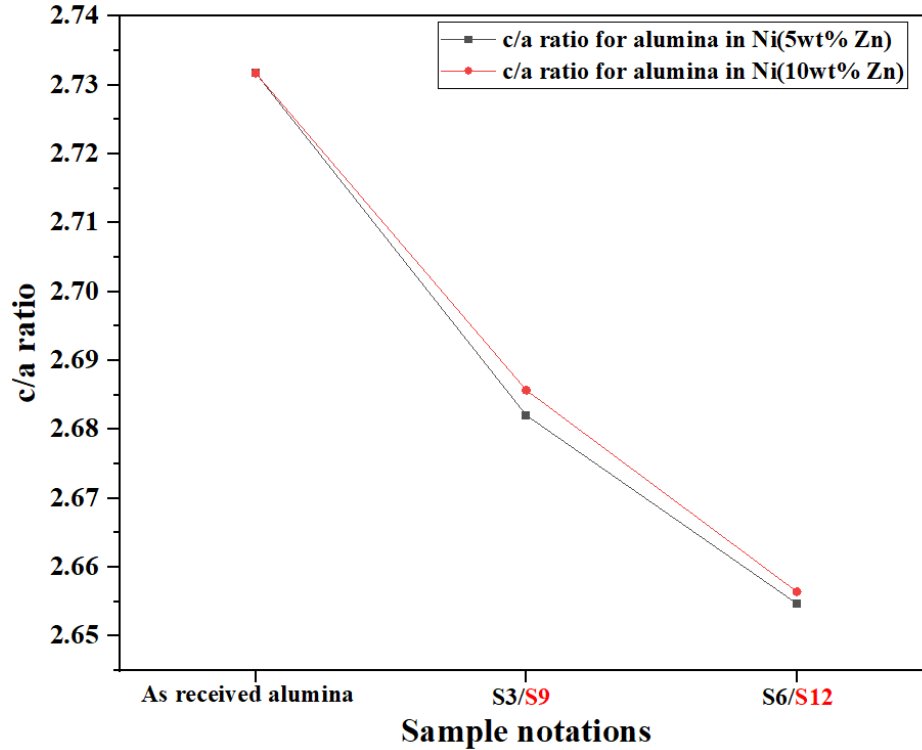
Table 4.4: Calculation of (a) lattice parameter; and (b) c/a ratio of various compositions [103].

(a)	
Sample notation	Lattice parameter 'a' (Å)
Ni(5wt.% Zn)	
As-received	3.51321
S13	3.56278
S3	3.56852
S6	3.57822
Ni(10wt.% Zn)	
As-received	3.5558
S14	3.56476
S9	3.62075
S12	3.58266
(b)	
Sample notation	c/a ratio for hexagonal crystal structure
As-received Al ₂ O ₃	2.73175
Al ₂ O ₃ in S3	2.68203

Al ₂ O ₃ in S6	2.65469
Al ₂ O ₃ in S9	2.68571
Al ₂ O ₃ in S12	2.65642



(a)



(b)

Figure 4.15: (a) lattice parameters of Ni(Zn) alloy particles specimens S13, S14 and the lattice parameters of Ni(Zn) alloy matrix in composite specimens S3, S6, S9, S12; and (b) c/a ratio of lattice parameters of as-received alumina as well as alumina reinforcement in composite specimens S3, S6, S9, S12 [103].

The capability to evenly distribute reinforcing agents throughout the metal matrix, preserve structural integrity, and provide an effective interface between matrix and reinforcement during composite fabrication and processing are the major factors influencing the performance of the MMCs. Conventional methods such as extrusion [8], plasma spray [116], rolling and pressing [117], and sintering and extrusion [118,119] may cause harm to nanostructures and generate secondary phases such as metal oxides and carbides, which could impact the intended commercial applications [5,120]. The HE-MA process used in the present research ensures the structural integrity and even distribution of alumina

ceramic grains in the Ni(Zn) alloy matrix while providing adequate control over the crystallite size, lattice parameters of constituents in the composite particles and composite particle morphology. The Ni(Zn)-alumina particles thus synthesized using HEMA process in this research may work for cold spray applications due to its particle size and irregular particle morphology. Research studies on the utilization of irregular shaped particle feedstock have shown effective DE. Unevenly shaped particles can achieve higher in-flight velocities during cold spraying that can reduce porosity and form dense coatings [92].

The Ni(Zn)-alumina particle composition has been meticulously devised by keeping in mind the effective deposition efficiency (DE) of the composite particles over the industrially relevant metallic substrates. Some of the research works on Ni based alloy composite coatings also suggest that these have a good cold spray ability. Ruben Fernandez et al. [121] fabricated CrC-NiCr cermet cold spray coating with amount of CrC ceramic content between 60% to 75% in the particle feedstock. Though the ceramic content was high yet they were successful in fabricating a cold sprayed coating. Another study on CrC-NiCr cold spray coatings suggested that the use of high ceramic content of 75% along with NiCr alloy as particle feedstock could create cold spray coating with required bond strength and tribological properties [122]. However, it is suggested to keep ceramic content in particle feedstock higher than 10% to ameliorate the required mechanical performance of the cold sprayed coatings [123]. Therefore, it would be safe to presume the applicability and cold spray ability of Ni(Zn)-alumina composite particles synthesized by HEMA process, to produce cold spray coatings which may have exceptional mechanical and tribological properties that can make it a commercial success.

4.6 Summary

The results for the particle characterization in this chapter reveal that the experimental design and milling process for the creation of Ni(Zn)-alumina composite having a homogeneous composition has been successfully executed. The Ni(Zn) alloy precursors were successfully pre milled and reduced to micron size particles suitable for further milling and synthesizing Ni(Zn)-alumina particles. The EBSD characterization of alloy particles reveal the ductility and extent of plastic deformation of Ni(Zn) alloy particles for both the alloy compositions employed in this research. Ni(5wt.% Zn) has higher ductility as compared to Ni(10wt.% Zn). And this result was also proved in the particle microstructures and powder size distribution analysis of alloy particles where Ni(5wt.% Zn) particles showed high higher particle size and delay in fracture process. Furthermore, the flaky shaped Ni(Zn) alloy particles offered enough sites for alumina embedment and thereby facilitating the formation of a homogeneous Ni(Zn)-alumina composite particle creation. The composite particle microstructural characterization depicts particle morphology and the uniform dispersion of alumina grains in the Ni(Zn) alloy matrix. The powder size distribution performed helped in the selection of appropriate particle size suitable for cold spray applications. Also, XRD analysis results show the phases, crystallite sizes, lattice parameters in the composite particles. At last, the design and properties of Ni(Zn)-alumina composite particles milled for four hours make it a suitable particle feedstock for CGDS process to create cold spray coatings with homogeneous composition which may have uniform mechanical, and tribological properties.

Chapter 5 Conclusion and Future Recommendations

In this research, HE-MA method was used to create Ni(Zn)-alumina composite particles. Two steps of milling were carried out: 1) pre-milling, for a duration of 2 hours to break down Ni(Zn) alloy precursor particles from millimeter-sized to micron-sized particles; and 2) milling, for a duration of 4 hours, for embedment of alumina in the Ni(Zn) alloy matrix and provide composite particle feedstock for cold spray process. This study led to the following conclusions:

1. The presence of alumina inside the Ni(Zn) alloy matrix was verified by SEM microstructures along with the EDS elemental analysis performed. In the milled specimens, agglomerates were seen, and their quantity rose as the percentage of alumina reinforcement in the composite particles increased.
2. Significant plastic deformation of the Ni(Zn) alloy particles caused by the HE-MA process was demonstrated by the EBSD characterization. The Ni(5wt% Zn) alloy particles exhibited greater ductility and consistent deformation in contrast to the Ni(10wt% Zn) alloy particles.
3. The milled particles had a PSD that follows Gaussian distribution. The process of cold welding and fracture of particles during milling were evident in the PSD of the particles milled for 1 hour, 2 hours, and 4 hours. The alumina concentration (wt.%) had an impact on the composite particle size distribution.
4. The volume fraction of particles within the targeted 10-100 μm range were measured by computing the cumulative volume fraction values. A particle size range between 10 and 100 μm was found to be present in most of the milled S3, S6,

S9, and S11 specimens. The embedded alumina was found to have grain sizes in the range of a few hundred nanometers.

5. Owing to the extreme plastic deformation and consequent cold working that the particles underwent during HE-MA, peak broadening was seen in the XRD patterns of the milled specimens. As the content of alumina in the composite increased, the α -Al₂O₃ peaks were more noticeable. A study was conducted on the crystallite size of the particle compositions, and the results showed that the alloy and composite powder crystallite sizes generally shrank as the milling time increased. Also, when the milling time increased, the lattice parameter corresponding to the Ni(Zn) matrix increased. As the milling duration increased, the lattice parameter c/a ratio of Al₂O₃ dropped.
6. The feasibility of composite feedstock synthesized by HEMA process for CS deposition was demonstrated by the quantitative and qualitative features of the feedstock as revealed by the results of this current research. Thus, the authors note that the findings presented in this work are important for further investigation and creation of nanostructured Ni(Zn)-Al₂O₃ coatings, which are sought after by several applications.

There is much potential for further research on Ni-based cold spray coatings. However, to fabricate the best quality coatings it is vital to understand the characteristics of particle feedstock employed for cold spray. Particle characterization becomes crucial when performing milling to design and synthesize alloy/composite particles to ensure uniform properties across the coatings fabricated over an industrially relevant metallic substrate.

There is enough research gap in terms of Particle EBSD characterization, particle nanoindentation characterization to explore the mechanical properties of the particles synthesized via HEMA. Single particle bonding characteristics is another interesting field for future research. Research needs to be done to determine the best sort and quantity of reinforcements to employ in order to provide Ni-based coatings with the desired properties. It will take more investigation to find out how well powder morphology and powder architecture and help these Ni-based coatings deposit. The higher the deposition efficiency, the less powder feedstock is wasted during the cold spraying process. The research study may also include two reinforcements that can enhance the metal matrix's mechanical, tribological, corrosion resistance characteristics. The tribological properties of Ni-based coatings in respect to the various reinforcements used require more investigation; these properties can be contrasted with those of other coating techniques including HVOF, CVD, sintering, and so on. Comparing several Ni-based cold-sprayed coatings with various reinforcing types is also feasible. A detailed investigation into preserving the grain sizes and original phases along with the material chemistry would be desirable. Research on the effects of bond strength on the tribological characteristics of Ni-based cold spray coatings can help produce valuable coatings with high commercial value.

Bibliography

1. Dhand, D., Grewal, J. S., & Kumar, P. (2021). Study and comparison of wear behavior of Ni-Al₂O₃ coatings deposited by hot and cold spray. *Surface Topography: Metrology and Properties*, 9(4), 045056. <https://doi.org/10.1088/2051-672X/ac4402>
2. Zhu, H., Niu, Y., Lin, C., Huang, L., Ji, H., & Zheng, X. (2013). Microstructures and tribological properties of vacuum plasma sprayed B₄C–Ni composite coatings. *Ceramics International*, 39(1), 101–110. <https://doi.org/10.1016/j.ceramint.2012.05.101>
3. Singh, A., Kumar, H., & Kumar, S. (2023). A Comparative Study of Erosion Wear Performance of Thermally Sprayed Ni-Based Composite Coatings. *Journal of Materials Engineering and Performance*. <https://doi.org/10.1007/s11665-023-08041-x>
4. Nath, L., & Saha, G. (2017). Synthesis and characterization of nanocrystalline Al₂O₃-Ni(Cr) particles using high-energy mechanical alloying process. *Surface and Coatings Technology*, 318. <https://doi.org/10.1016/j.surfcoat.2017.01.024>
5. Woo, D. J., Sneed, B., Peerally, F., Heer, F. C., Brewer, L. N., Hooper, J. P., & Osswald, S. (2013). Synthesis of nanodiamond-reinforced aluminum metal composite powders and coatings using high-energy ball milling and cold spray. *Carbon*, 63, 404–415. <https://doi.org/10.1016/j.carbon.2013.07.001>

6. Kuzumaki, T., Miyazawa, K., Ichinose, H., & Ito, K. (1998). Processing of Carbon Nanotube Reinforced Aluminum Composite. *Journal of Materials Research*, 13(9), 2445–2449. <https://doi.org/10.1557/JMR.1998.0340>
7. Esawi, A., & Morsi, K. (2007). Dispersion of carbon nanotubes (CNTs) in aluminum powder. *Composites Part A-Applied Science and Manufacturing - COMPOS PART A-APPL SCI MANUF*, 38, 646–650. <https://doi.org/10.1016/j.compositesa.2006.04.006>
8. Esawi, A. M. K., Morsi, K., Sayed, A., Gawad, A. A., & Borah, P. (2009). Fabrication and properties of dispersed carbon nanotube–aluminum composites. *Materials Science & Engineering A*, 1–2(508), 167–173. <https://doi.org/10.1016/j.msea.2009.01.002>
9. Wang, L., Choi, H., Myoung, J. M., & Lee, W. (2009). Mechanical alloying of multi-walled carbon nanotubes and aluminium powders for the preparation of carbon/metal composites. *Carbon*, 47(15), 3427–3433. <https://doi.org/10.1016/j.carbon.2009.08.007>
10. Sridhar, I., & Narayanan, K. (2009). Processing and characterization of MWCNT reinforced aluminum matrix composites. *Journal of Materials Science*, 44, 1750–1756. <https://doi.org/10.1007/s10853-009-3290-5>
11. Choi, H., Shin, J., Min, B., Park, J., & Bae, D. (2009). Reinforcing effects of carbon nanotubes in structural aluminum matrix nanocomposites. *Journal of Materials Research*, 24(8), 2610–2616. <https://doi.org/10.1557/jmr.2009.0318>

12. Myers M, Chawla K. Grain boundaries in plastic deformation (Grain-size strengthening). In: Mechanical behavior of materials. Cambridge UK: Cambridge Univ Press; 2009. p.345–8
13. Alidokht, S. A., & Chromik, R. R. (2021). Sliding wear behavior of cold-sprayed Ni-WC Composite coatings: Influence OF WC content. *Wear*, 477, 203792. <https://doi.org/10.1016/j.wear.2021.203792>
14. Kılıçay, K. (2020). Development of protective MMC coating on TZM alloy for high temperature oxidation resistance by LPCS. *Surface and Coatings Technology*, 393, 125777. <https://doi.org/10.1016/j.surfcoat.2020.125777>
15. Kumar, S. (2022). Influence of processing conditions on the mechanical, tribological and fatigue performance of cold spray coating: A review. *Surface Engineering*, 38(4), 324–365. <https://doi.org/10.1080/02670844.2022.2073424>
16. Sun, W., Chu, X., Lan, H., Huang, R., Huang, J., Xie, Y., Huang, J., & Huang, G. (2022). Current Implementation Status of Cold Spray Technology: A Short Review. *Journal of Thermal Spray Technology*, 31(4), 848–865. <https://doi.org/10.1007/s11666-022-01382-4>
17. Smid, I., Segall, A. E., Walia, P., Aggarwal, G., Eden, T. J., & Potter, J. K. (2012). Cold-Sprayed Ni-hBN Self-Lubricating Coatings. *Tribology Transactions*, 55(5), 599–605. <https://doi.org/10.1080/10402004.2012.686085>
18. Liu, Z., Lian, W., Liu, C., & Jie, X. (2023). Fabrication of In Situ rGO Reinforced Ni–Al Intermetallic Composite Coatings by Low Pressure Cold Spraying with Desired High Temperature Wear Characteristics. *Materials*, 16(9), Article 9. <https://doi.org/10.3390/ma16093537>

19. Georgiou, E. P., Dosta, S., Fernández, J., Matteazzi, P., Kowalski, K., Kusinski, J., Piticescu, R. R., & Celis, J.-P. (2016). Structural and Tribological Properties of Nanostructured Supersonic Cold Sprayed Ni-20 wt.% Sn Coatings. *Journal of Thermal Spray Technology*, 25(5), 1029–1039. <https://doi.org/10.1007/s11666-016-0418-4>
20. Sun, W., Tan, A. W.-Y., Bhowmik, A., Xue, F., Marinescu, I., & Liu, E. (2019). Evaluation of cold sprayed graphene nanoplates–Inconel 718 composite coatings. *Surface and Coatings Technology*, 378, 125065. <https://doi.org/10.1016/j.surfcoat.2019.125065>
21. Wu, K., Sun, W., Tan, A. W.-Y., Marinescu, I., Liu, E., & Zhou, W. (2021). An investigation into microstructure, tribological and mechanical properties of cold sprayed Inconel 625 coatings. *Surface and Coatings Technology*, 424, 127660. <https://doi.org/10.1016/j.surfcoat.2021.127660>
22. Torgerson, T. B., Harris, M. D., Alidokht, S. A., Scharf, T. W., Aouadi, S. M., Chromik, R. R., Zabinski, J. S., & Voevodin, A. A. (2018). Room and elevated temperature sliding wear behavior of cold sprayed Ni-WC composite coatings. *Surface and Coatings Technology*, 350, 136–145. <https://doi.org/10.1016/j.surfcoat.2018.05.090>
23. Alidokht, S. A., Manimunda, P., Vo, P., Yue, S., & Chromik, R. R. (2016). Cold spray deposition of a Ni-WC composite coating and its dry sliding wear behavior. *Surface and Coatings Technology*, 308, 424–434. <https://doi.org/10.1016/j.surfcoat.2016.09.089>

24. Alidokht, S. A., & Chromik, R. R. (2021). Sliding wear behavior of cold-sprayed Ni-WC composite coatings: Influence OF WC content. *Wear*, 477, 203792. <https://doi.org/10.1016/j.wear.2021.203792>
25. Chen, J., Song, H., Liu, G., Ma, B., An, Y., & Jia, L. (2020). Cold Spraying: A New Alternative Preparation Method for Nickel-Based High-Temperature Solid-Lubrication Coating. *Journal of Thermal Spray Technology*, 29(8), 1892–1901. <https://doi.org/10.1007/s11666-020-01088-5>
26. Dhand, D., Kumar, P., & Grewal, J. S. (2022). Wear behavior and microstructural characteristics of cold sprayed nickel-alumina coatings on boiler steel: Original scientific paper. *Journal of Electrochemical Science and Engineering*, 12(5), Article 5. <https://doi.org/10.5599/jese.1270>
27. Yang, Y., Kushima, A., Han, W., Xin, H., & Li, J. (2018). Liquid-Like, Self-Healing Aluminum Oxide during Deformation at Room Temperature. *Nano Letters*, 18(4), 2492–2497. <https://doi.org/10.1021/acs.nanolett.8b00068>
28. Ceschini, L., Morri, A., & Rotundo, F. (2014). Forming of Metal Matrix Composites. *Comprehensive Materials Processing*, 3, 159–186. <https://doi.org/10.1016/B978-0-08-096532-1.00311-3>
29. Miracle, D. B. (2005). Metal matrix composites – From science to technological significance. *Composites Science and Technology*, 65(15), 2526–2540. <https://doi.org/10.1016/j.compscitech.2005.05.027>
30. Evans, A., SanMarchi, C., & Mortensen, A. (2003). *Metal Matrix Composites in Industry: An Introduction and a Survey*. [https://doi.org/10.1007/978-1-4615-0405-](https://doi.org/10.1007/978-1-4615-0405-4)

31. Ibrahim, I. A., Mohamed, F. A., & Lavernia, E. J. (1991). Particulate reinforced metal matrix composites—A review. *Journal of Materials Science*, 26(5), 1137–1156. <https://doi.org/10.1007/BF00544448>
32. Surappa, M. K. (2003). Aluminium matrix composites: Challenges and opportunities. *Sadhana*, 28(1), 319–334. <https://doi.org/10.1007/BF02717141>
33. Stojanovic, B., & Ivanovic, L. (2015). Application of aluminium hybrid composites in automotive industry. *Tehnicki Vjesnik*, 22, 247–251. <https://doi.org/10.17559/TV-20130905094303>
34. Villafuerte, J. (2015). *Modern cold spray*. Ontario: Springer.
35. Lagutkin, S., Achelis, L., Sheikhaliev, S., Uhlenwinkel, V., & Srivastava, V. (2004). Atomization process for metal powder. *Materials Science and Engineering: A*, 383(1), 1–6. <https://doi.org/10.1016/j.msea.2004.02.059>
36. Unal, A. (1989). Liquid break-up in gas atomization of fine aluminum powders. *Metallurgical Transactions B*, 20, 61–69. <https://doi.org/10.1007/BF02670350>
37. Yule, A., & Dunkley, J. (1994). Atomization of Melts: For Powder Production and Spray Deposition. In *Oxford Series on Advanced Manufacturing (Book 11)*.
38. DATTA, B. K. (2011). *POWDER METALLURGY: AN ADVANCED TECHNIQUE OF PROCESSING ENGINEERING MATERIALS*. PHI Learning.
39. Menon V, Aranas Jr. C, Saha G, 2022, Cold spray additive manufacturing of copper-based materials: Review and future directions. *Mater Sci Add Manuf*. 1(2): 1-20. <https://doi.org/10.18063/msam.v1i2.12>

40. A. Nastic, D. MacDonald, and B. Jodoin, The Influence of Feedstock Powder, In: S. Pathak, and G.C. Saha (eds), *Cold Spray in the Realm of Additive Manufacturing*, Springer International Publishing, Cham, Switzerland, 2020, p 33-85
41. Fauchais, P., Montavon, G., & Bertrand, G. (2010). From Powders to Thermally Sprayed Coatings. *Journal of Thermal Spray Technology*, 19(1), 56–80. <https://doi.org/10.1007/s11666-009-9435-x>
42. Menon, V., Sripada, J. V. S. N., & Saha, G. C. (2023). Nanostructured Ni(Zn)–Al₂O₃ cermet particle synthesis in high-energy mechanical alloying method (CG-3:IL07). *Ceramics International*, 49(14, Part B), 24339–24350. <https://doi.org/10.1016/j.ceramint.2023.02.078>
43. Ghelichi, R., Bagherifard, S., Mac Donald, D., Brochu, M., Jahed, H., Jodoin, B., & Guagliano, M. (2014). Fatigue strength of Al alloy cold sprayed with nanocrystalline powders. *International Journal of Fatigue*, 65, 51–57. <https://doi.org/10.1016/j.ijfatigue.2013.09.001>
44. Ajdelsztajn, L., Zúñiga, A., Jodoin, B., & Lavernia, E. J. (2006). Cold-Spray processing of a nanocrystalline Al–Cu–Mg–Fe–Ni alloy with Sc. *Journal of Thermal Spray Technology*, 15(2), 184–190. <https://doi.org/10.1361/105996306X107995>
45. Neikov, O. D. (2019). Chapter 3—Mechanical Alloying. In O. D. Neikov, S. S. Naboychenko, & N. A. Yefimov (Eds.), *Handbook of Non-Ferrous Metal Powders (Second Edition)* (pp. 91–124). Elsevier. <https://doi.org/10.1016/B978-0-08-100543-9.00003-8>

46. Benjamin, J. S. (1970). Dispersion strengthened superalloys by mechanical alloying. *Metallurgical Transactions*, 1(10), 2943–2951. <https://doi.org/10.1007/BF03037835>
47. Davis, R. M., McDermott, B., & Koch, C. C. (1988). Mechanical alloying of brittle materials. *Metallurgical Transactions A*, 19, 2867–2874. <https://doi.org/10.1007/BF02647712>
48. Benjamin, J. S. (1990). Mechanical alloying—A perspective. *Metal Powder Report*, 45(2), 122–127. [https://doi.org/10.1016/S0026-0657\(10\)80124-9](https://doi.org/10.1016/S0026-0657(10)80124-9)
49. Benjamin, J. S., & Volin, T. E. (1974). The mechanism of mechanical alloying. *Metallurgical Transactions*, 5(8), 1929–1934. <https://doi.org/10.1007/BF02644161>
50. Mechanical alloying and milling C. Suryanarayana Department of Metallurgical and Materials Engineering, Colorado School of Mines, Golden, CO 80401-1887, USA, *Progress in Materials Science* 46 (2001) 1-184
51. Di, L. M., & Bakker, H. (1991). Phase transformation of the compound V₃Ga induced by mechanical grinding. *Journal of Physics: Condensed Matter*, 3(20), 3427. <https://doi.org/10.1088/0953-8984/3/20/004>
52. Kaloshkin, S. D., Tomilin, I. A., Andrianov, G. A., Baldokhin, U. V., & Shelekhov, E. V. (1997). Phase Transformations and Hyperfine Interactions in Mechanically Alloyed Fe-Cu Solid Solutions. *Materials Science Forum*, 235–238, 565–570. <https://doi.org/10.4028/www.scientific.net/MSF.235-238.565>

53. Kuhrt C, Schropf H, Schultz L, Arzt E. In: deBarbadillo JJ, et al., editors. Mechanical alloying for structural applications. Materials Park, OH: ASM International, 1993. p. 269-73
54. Suryanarayana, C. (1995). Does a disordered γ -TiAl phase exist in mechanically alloyed TiAl powders? *Intermetallics*, 3(2), 153–160. [https://doi.org/10.1016/0966-9795\(95\)92680-X](https://doi.org/10.1016/0966-9795(95)92680-X)
55. Lai MO, Lu L. Mechanical alloying. Boston, MA: Kluwer Academic Publishers, 1998.
56. Watanabe R, Hashimoto H, Park Y-H. In: Pease III LF, Sansoucy RJ, editors. Advances in powder metallurgy 1991, vol. 6. Princeton, NJ: Metal Powder Industries Federation, 1991. P.119±30.
57. Park, Y. H., Hashimoto, H., & Watanabe, R. (1992). Morphological Evolution and Amorphization of Ti/Cu and Ti/Al Powder Mixtures during Vibratory Ball Milling. *Materials Science Forum*, 88–90, 59–66. <https://doi.org/10.4028/www.scientific.net/MSF.88-90.59>
58. Suryanarayana, C., Chen, G.-H., & Froes, F. H. (Sam). (1992). Milling maps for phase identification during mechanical alloying. *Scripta Metallurgica et Materialia*, 26(11), 1727–1732. [https://doi.org/10.1016/0956-716X\(92\)90542-M](https://doi.org/10.1016/0956-716X(92)90542-M)
59. Miki, M., Yamasaki, T., & Ogino, Y. (1992). Preparation of Nanocrystalline NbN and (Nb, Al)N Powders by Mechanical Alloying under Nitrogen Atmosphere. *Materials Transactions, JIM*, 33(9), 839–844. <https://doi.org/10.2320/matertrans1989.33.839>

60. Calka, A., & Williams, J. S. (1992). Synthesis of Nitrides by Mechanical Alloying. *Materials Science Forum*, 88–90, 787–794.
<https://doi.org/10.4028/www.scientific.net/MSF.88-90.787>
61. Chen, Y., & Williams, J. R. (1996). Hydriding Reactions Induced by Ball Milling. *Materials Science Forum*, 225–227, 881–888.
<https://doi.org/10.4028/www.scientific.net/MSF.225-227.881>
62. Nouri, A., & Wen, C. (2013). *Surfactants in Mechanical Alloying/Milling: A Catch-22 Situation. Critical Reviews in Solid State and Materials Sciences*, 39(2), 81–108.
doi:10.1080/10408436.2013.808985
63. Nouri, A., Hodgson, P. D., & Wen, C. E. (2010). Effect of process control agent on the porous structure and mechanical properties of a biomedical Ti-Sn-Nb alloy produced by powder metallurgy. *Acta Biomaterialia*, 6(4), 1630–1639.
<https://doi.org/10.1016/j.actbio.2009.10.005>
64. Kubaski, E., Cintho, O., & Capocchi, J. (2011). Effect of milling variables on the synthesis of NiAl intermetallic compound by mechanical alloying. *Powder Technology - POWDER TECHNOLOGY*, 214, 77–82.
<https://doi.org/10.1016/j.powtec.2011.07.038>
65. Hiraga, H., Inoue, T., Kamado, S., Kojima, Y., Matsunawa, A., & Shimura, H. (2001). Fabrication of NiTi intermetallic compound coating made by laser plasma hybrid spraying of mechanically alloyed powders. *Surface and Coatings Technology*, 139, 93–100. [https://doi.org/10.1016/S0257-8972\(01\)00994-X](https://doi.org/10.1016/S0257-8972(01)00994-X)
66. Keskinen, J., Pogany, A., Rubin, J., & Ruuskanen, P. (1995). Carbide and hydride formation during mechanical alloying of titanium and aluminium with hexane.

Materials Science and Engineering: A, 196(1), 205–211.
[https://doi.org/10.1016/0921-5093\(94\)09701-1](https://doi.org/10.1016/0921-5093(94)09701-1)

67. Sheibani, S., Ataie, A., & Heshmati-Manesh, S. (2008). Role of process control agent on synthesis and consolidation behavior of nano-crystalline copper produced by mechano-chemical route. *Journal of Alloys and Compounds*, 465(1), 78–82.
<https://doi.org/10.1016/j.jallcom.2007.10.062>
68. Chen, C.-L., & Dong, Y.-M. (2011). Effect of mechanical alloying and consolidation process on microstructure and hardness of nanostructured Fe–Cr–Al ODS alloys. *Materials Science and Engineering: A*, 528(29–30), 8374–8380.
<https://doi.org/10.1016/j.msea.2011.08.041>
69. Byun, J.-S., Shim, J.-H., & Cho, Y. W. (2004). Influence of stearic acid on mechanochemical reaction between Ti and BN powders. *Journal of Alloys and Compounds*, 365(1), 149–156. [https://doi.org/10.1016/S0925-8388\(03\)00638-8](https://doi.org/10.1016/S0925-8388(03)00638-8)
70. O. D. Neikov, Mechanical crushing and grinding, in Handbook of Non-Ferrous Metal Powders, Neikov, O. D., Naboychenko, S. S., and Dowson, G., Eds., Elsevier, Oxford, UK, 47–62 (2009)
71. Hong, L. B., Bansal, C., & Fultz, B. (1994). Steady state grain size and thermal stability of nanophase Ni₃Fe and Fe₃X (X = Si, Zn, Sn) synthesized by ball milling at elevated temperatures. *Nanostructured Materials*, 4(8), 949–956.
[https://doi.org/10.1016/0965-9773\(94\)90101-5](https://doi.org/10.1016/0965-9773(94)90101-5)
72. Kimura H, Kimura M. In: Clauer AH, deBarbadillo JJ, editors. Solid state powder processing. Warrendale, PA: TMS, 1990. p. 365-77.

73. Lee, C. H., Mori, M., Fukunaga, T., & Mizutani, U. (1990). Effect of Ambient Temperature on the MA and MG Processes in Ni–Zr Alloy System. *Japanese Journal of Applied Physics*, 29(3R), 540. <https://doi.org/10.1143/JJAP.29.540>
74. Yamada, K., & Koch, C. C. (1993). The influence of mill energy and temperature on the structure of the TiNi intermetallic after mechanical attrition. *Journal of Materials Research*, 8(6), 1317–1326. <https://doi.org/10.1557/JMR.1993.1317>
75. Koch CC, Pathak D, Yamada K. In: deBarbadillo JJ, et al., editors. Mechanical alloying for structural applications. Materials Park, OH: ASM International, 1993. p. 205-12
76. Günther, R., Klassen, T., Dickau, B., Gärtner, F., Bartels, A., & Bormann, R. (2001). Advanced Alumina Composites Reinforced with Titanium-Based Alloys. *Journal of the American Ceramic Society*, 84, 1509–1513. <https://doi.org/10.1111/j.1151-2916.2001.tb00869.x>
77. Alonso, F., Fagoaga, I., & Oregui, P. (1991). Erosion protection of carbon—Epoxy composites by plasma-sprayed coatings. *Surface and Coatings Technology*, 49(1), 482–488. [https://doi.org/10.1016/0257-8972\(91\)90104-5](https://doi.org/10.1016/0257-8972(91)90104-5)
78. Kathirvel, P., Chandrasekaran, J., Manoharan, D., & Kumar, S. (2014). Preparation and characterization of alpha alumina nanoparticles by in-flight oxidation of flame synthesis. *Journal of Alloys and Compounds*, 590, 341–345. <https://doi.org/10.1016/j.jallcom.2013.12.105>
79. Kiliçay, K., & Dayi, S. C. (2021). Investigation on the Performance of Al7075 Alloy Surface Repaired by Cold Spray Coating Technology. In *Solid State*

Phenomena (Vol. 324, pp. 9–14). Trans Tech Publications, Ltd.
<https://doi.org/10.4028/www.scientific.net/ssp.324.9>

80. Kılıçay, K. (2020). Development of protective MMC coating on TZM alloy for high temperature oxidation resistance by LPCS. *Surface and Coatings Technology*, 393, 125777. <https://doi.org/10.1016/j.surfcoat.2020.125777>
81. Hofmockel M, Neubing H-C. ECKA Discup—new high performance PM-copper materials process, properties and applications. In: *Proceedings of PM 2004 world congress, Vienna*. Compiled by European powder metallurgy association, Bellstone Shrewsbury, UK, vol. 1; 2004. p. 231–6.
82. Llorca-Isern NC, Artieda-Guzma'n CN, Porrás-Mateu N, Roca A. Structural and magnetic properties of nanocrystalline Cu-Fe-Co-Al₂O₃ composite powders processed by mechanical alloying. In: *Proceedings of PM 2010 world congress, Florence*. Compiled by European powder metallurgy association, Bellstone Shrewsbury, UK, vol. 1; 2010. p. 159–66.
83. Anderson, K. R., Groza, J. R., Dreshfield, R. L., & Ellis, D. (1995). High-Performance dispersion-strengthened Cu-8 Cr-4 Nb alloy. *Metallurgical and Materials Transactions A*, 26(9), 2197–2206. <https://doi.org/10.1007/BF02671235>
84. Lo'pez M, Corredor D, Ramam K, Jimenez J, Ruano O. (2007). Performance of new dispersion-precipitation strengthened copper-ceramic materials made by mechanical alloying. *Phys Stat Sol*; 4(11):4248–53.
<https://doi.org/10.1002/pssc.200675940>.

85. Lo'pez M, Jimenez JA, Corredor D.(2007). Precipitation strengthened high strength-conductivity copper alloys containing ZrC ceramics. *Composites*; 38(Part A):272–9, <http://www.elsevier.com/locate/compositesa>
86. Alkhimov AP, Papyrin AN, Kosarev VF, et al., 1994, Gas dynamic spraying method for applying a coating (United States Patent No. US5302414A). Available from: <https://patents.google.com/patent/US5302414A/en> [Last accessed on 2022 May 31]
87. Tokarev AO, 1996, Structure of aluminum powder coatings prepared by cold gas dynamic spraying. *Metal Sci Heat Treat*, 38: 136–139. <https://doi.org/10.1007/BF01401446>
88. Kumar, S. (2022). Influence of processing conditions on the mechanical, tribological and fatigue performance of cold spray coating: A review. *Surface Engineering*, 38(4), 324–365. <https://doi.org/10.1080/02670844.2022.2073424>
89. Imbriglio, S. I., & Chromik, R. R. (2021). Factors Affecting Adhesion in Metal/Ceramic Interfaces Created by Cold Spray. *Journal of Thermal Spray Technology*, 30(7), 1703-1723. <https://doi.org/10.1007/s11666-021-01229-4>
90. Sripada J, Gallant M, Saha G, 2019, Study on the effect of milling parameters on HE-MA nanostructured Al-graphene cermet particles. *Proceedings of 1st Coatings and Interfaces Web Conference*, 2019, 6160. <https://doi.org/10.3390/ciwc2019-06160>
91. Pathak, S., Saha, G.C., Cold Spray in the Realm of Additive Manufacturing, *Materials Forming, Machining and Tribology*, <https://doi.org/10.1007/978-3-030-42756-6>

92. Raelison, R. N., Xie, Y., Sapanathan, T., Planche, M. P., Kromer, R., Costil, S., & Langlade, C. (2018). Cold gas dynamic spray technology: A comprehensive review of processing conditions for various technological developments till to date. *Additive Manufacturing*, 19, 134–159. <https://doi.org/10.1016/j.addma.2017.07.001>
93. Ning, X.-J., Jang, J.-H., & Kim, H.-J. (2007). The effects of powder properties on in-flight particle velocity and deposition process during low pressure cold spray process. *Applied Surface Science*, 253(18), 7449–7455. <https://doi.org/10.1016/j.apsusc.2007.03.031>
94. Wong, W., Vo, P., Irissou, E., Ryabinin, A. N., Legoux, J.-G., & Yue, S. (2013). Effect of Particle Morphology and Size Distribution on Cold-Sprayed Pure Titanium Coatings. *Journal of Thermal Spray Technology*, 22(7), 1140–1153. <https://doi.org/10.1007/s11666-013-9951-6>
95. Jodoin, B., Ajdelsztajn, L., Sansoucy, E., Zúñiga, A., Richer, P., & Lavernia, E. J. (2006). Effect of particle size, morphology, and hardness on cold gas dynamic sprayed aluminum alloy coatings. *Surface and Coatings Technology*, 201(6), 3422–3429. <https://doi.org/10.1016/j.surfcoat.2006.07.232>
96. Cinca, N., Rebled, J. M., Estradé, S., Peiró, F., Fernández, J., & Guilemany, J. M. (2013). Influence of the particle morphology on the Cold Gas Spray deposition behaviour of titanium on aluminum light alloys. *Journal of Alloys and Compounds*, 554, 89–96. <https://doi.org/10.1016/j.jallcom.2012.11.069>
97. Operations Guide, © Malvern Instruments Ltd. 1998, 1999

98. Yang Leng, Materials Characterization Introduction to Microscopic and Spectroscopic Methods, John Wiley & Sons (Asia) Pte Ltd.
99. David Brandon, Wayne D. Kaplan, Microstructural Characterization of Materials, John Wiley & Sons Ltd.
100. Stojakovic, D. (2012). Electron backscatter diffraction in materials characterization. *Processing and Application of Ceramics*, 6. <https://doi.org/10.2298/PAC1201001S>
101. B.D. Cullity, Elements of Xray diffraction, Second edition, Addison-Wesley publishing company
102. <https://www.bruker.com/en/products-and-solutions/diffractometers-and-x-ray-microscopes/x-ray-diffractometers/d8-advance-family/d8-advance.html> [referred on 23rd May, 2024]
103. Vineeth Menon, Jagannadh V.S.N. Sripada, Gobinda C. Saha (2023), Nanostructured Ni (Zn)-Al₂O₃ cermet particle synthesis in high-energy mechanical alloying Method. <http://doi.org/10.1016/j.ceramint.2023.02.078>
104. A. Colella, P. Matteazzi, (2016) Powder production techniques for high-pressure cold spray, in: C.M. Kay, J. Karthikeyan (Eds.), High Pressure Cold Spray: Principles and Applications, vol. 46, ASM International, pp. 173–182.
105. A. Sabard, T. Hussain, (2018) Bonding mechanisms in cold spray deposition of gas atomised and solution heat-treated Al 6061 powder by EBSD (arXiv:1811.08694), ArXiv . <https://doi.org/10.48550/arXiv.1811.08694>.

106. P. Matteazzi, G. Le Ca'ër, A. Mocellin, (1997) Synthesis of nanostructured materials by mechanical alloying, *Ceram. Int.* [https://doi.org/10.1016/0272-8842\(95\)00138-7](https://doi.org/10.1016/0272-8842(95)00138-7)
107. H. Assadi, T. Schmidt, H. Richter, J.O. Kliemann, K. Binder, F. Gartner, T. Klassen, H. Kreye, (2011) On parameter selection in cold spraying, *J. Therm. Spray Technol.* <https://doi.org/10.1007/s11666-011-9662-9>.
108. T. Marrocco, D.G. McCartney, P.H. Shipway, A.J. Sturgeon, (2006) Production of titanium deposits by cold-gas dynamic spray: Numerical modeling and experimental characterization, *J. Therm. Spray Technol.* <https://doi.org/10.1361/105996306X108219>
109. I. Dowding, M. Hassani, Y. Sun, D. Veysset, K.A. Nelson, C.A. Schuh, (2020) Particle size effects in metallic microparticle impact-bonding, *Acta Mater.* <https://doi.org/10.1016/j.actamat.2020.04.044>
110. N. Eigen, T. Klassen, E. Aust, R. Bormann, F. Gartner, (2003) Production of nanocrystalline cermet thermal spray powders for wear resistant coatings by high-energy milling, *Mater. Sci. Eng., A* , [https://doi.org/10.1016/S0921-5093\(03\)00110-2](https://doi.org/10.1016/S0921-5093(03)00110-2)
111. Z.R. Hesabi, A. Simchi, S.M.S. Reihani, (2006) Structural evolution during mechanical milling of nanometric and micrometric Al₂O₃ reinforced Al matrix composites, *Mater. Sci. Eng., A* , <https://doi.org/10.1016/j.msea.2006.04.116>.
112. J.V.S.N. Sripada, M.F. Gallant, G.C. Saha (2019), Study the effect of milling parameters on HE-MA nanostructured Al-graphene cermet particles, in: 1st

Coatings Interfaces Web Conf, CIWC, pp. 1–14,
<https://doi.org/10.3390/ciwc2019-06160>.

113. C. Suryanarayana (2019), Mechanical Alloying: A Novel Technique to Synthesize Advanced Materials, Research, <https://doi.org/10.34133/2019/4219812>.
114. S. Kalpakjian, S.R. Schmidt, K.S.V. Sekar, 2014 Manufacturing Engineering and Technology, SI units, seventh ed.
115. Pérez-Bustamante, R., Bolaños-Morales, D., Bonilla-Martínez, J., Estrada-Guel, I., & Martínez-Sánchez, R. (2014). Microstructural and hardness behavior of graphene-nanoplatelets/aluminum composites synthesized by mechanical alloying. *J. Alloys Comp.* (2014). <https://doi.org/10.1016/j.jallcom.2014.01.225>
116. Laha, T., Chen, Y., Lahiri, D., & Agarwal, A. (2009). Tensile properties of carbon nanotube reinforced aluminum nanocomposite fabricated by plasma spray forming. *Composites Part A: Applied Science and Manufacturing*, 40(5), 589–594. <https://doi.org/10.1016/j.compositesa.2009.02.007>
117. Esawi, A. M. K., & El Borady, M. A. (2008). Carbon nanotube-reinforced aluminium strips. *Composites Science and Technology*, 68(2), 486–492. <https://doi.org/10.1016/j.compscitech.2007.06.030>
118. Benjamin JS, editor. New materials by mechanical alloying techniques. Oberursel, Germany: DGM Informationgesellschaft; 1989.
119. Kwon, H., Estili, M., Takagi, K., Miyazaki, T., & Kawasaki, A. (2009). Combination of hot extrusion and spark plasma sintering for producing carbon nanotube reinforced aluminum matrix composites. *Carbon*, 47(3), 570–577. <https://doi.org/10.1016/j.carbon.2008.10.041>

120. _Woo, D. J., Heer, F. C., Brewer, L. N., Hooper, J. P., & Osswald, S. (2015). Synthesis of nanodiamond-reinforced aluminum metal matrix composites using cold-spray deposition. *Carbon*, 86, 15–25. <https://doi.org/10.1016/j.carbon.2015.01.010>
121. _Fernandez, R., & Jodoin, B. (2017). Effect of Particle Morphology on Cold Spray Deposition of Chromium Carbide-Nickel Chromium Cermet Powders. *Journal of Thermal Spray Technology*, 26(6), 1356–1380. <https://doi.org/10.1007/s11666-017-0580-3>
122. _Wolfe, D. E., Eden, T. J., Potter, J. K., & Jaroh, A. P. (2006). Investigation and characterization of Cr₃C₂-based wear-resistant coatings applied by the cold spray process. *Journal of Thermal Spray Technology*, 15(3), 400–412. <https://doi.org/10.1361/105996306X124400>
123. _Aussavy, D., Costil, S., El Kedim, O., Montavon, G., & Bonnot, A.-F. (2014). Metal Matrix Composite Coatings Manufactured by Thermal Spraying: Influence of the Powder Preparation on the Coating Properties. *Journal of Thermal Spray Technology*, 23(1), 190–196. <https://doi.org/10.1007/s11666-013-9999-3>

Appendix A: Material data sheets



Certificate of Analysis
ALUMINUM OXIDE POWDER
AL-600

1.1 General

SOLD TO	PURCHASE ORDER #	SHIP DATE	DOCUMENT NUMBER
UNIVERSITY OF NEW BRUNSWICK	PO249386	27 JUNE 2016	1605104
CATALOG NUMBER	LOT NUMBER	QUANTITY	CAS NUMBER
AL-600	1501525	11 LBS	1344-28-1

2.1 Chemical Analysis (in percentage (%) unless other wise stated)

Al	O
>53.10	>46.89

3.1 Screen Analysis (percent passing) / Other

Size
Sub-Micron

4.1 Notes

5.1 Statement

The above analysis is carried out as part of our internal quality control testing and is based upon our analysis methods.

We do not assume any warranty, liability, or risk based on such findings. Our quality is warranted within the scope of our general sales conditions.

Please refer to MSDS for material handling instructions.

Very Truly Yours,

M. Gerald, QA

24 Industrial Ave, Upper Saddle River, NJ 07458
On the web at: www.micronmetals.com

Tel: 201.828.9400 Fax: 201.828.9414
Email: info@micronmetals.com

Product Data Sheet

Zn-90% Ni-10%

Product Code: ZN-NI-01-P.10NI

Formula: Zn-Ni
CAS No.: N/A
EC No.: N/A
MDL: N/A

Chemical Identifiers

Linear Formula	Zn-Ni
MDL Number	N/A
EC No.	N/A
Pubchem CID	14877100
IUPAC Name	nickel; zinc
SMILES	[Ni].[Zn]
InChI Identifier	InChI=1S/Ni.Zn
InChI Key	QELJHCBNBNGDEXLD-UHFFFAOYSA-N

Total Metal Impurities: Variable or N/A

Packaging Specifications

Typical bulk packaging includes palletized plastic 5 gallon/25 kg. pails, fiber and steel drums to 1 ton super sacks in full container (FCL) or truck load (T/L) quantities. Research and sample quantities and hygroscopic, oxidizing or other air sensitive materials may be packaged under argon or vacuum. Shipping documentation includes a Certificate of Analysis and Safety Data Sheet (SDS). Solutions are packaged in polypropylene, plastic or glass jars up to palletized 440 gallon liquid totes, and 36,000 lb. tanker trucks.

Documentation
A Certificate of Analysis and Materials Safety Data Sheet (SDS) in accordance with EN 10204 are supplied with every shipment. AMERICAN ELEMENTS 10884 WEYBURN AVE. LOS ANGELES, CALIFORNIA 90024 TEL. 310-208-0551 FAX 310-208-0351 customerservice@americanelements.com

Curriculum Vitae

Candidate's full name: Vineeth Menon

Universities attended:

- National Institute of Technology, Raipur, India. B.Tech. Metallurgical Engineering, 2011–2015
- Indian Institute of Technology, Kharagpur, India. M.Tech. Metallurgical & Materials Engineering, 2016-2018

Publications:

- Menon V, Aranas Jr. C, Saha G, 2022, Cold spray additive manufacturing of copper-based materials: Review and future directions. *Mater Sci Add Manuf.* 1(2): 1-20. <https://doi.org/10.18063/msam.v1i2.12>
- Vineeth Menon, Jagannadh V.S.N. Sripada, Gobinda C. Saha (2023), Nanostructured Ni (Zn)-Al₂O₃ cermet particle synthesis in high-energy mechanical alloying Method. <http://doi.org/10.1016/j.ceramint.2023.02.078>